Dissertation
submitted to the
Combined Faculties of the Natural Sciences and Mathematics
of the Ruperto-Carola-University of Heidelberg, Germany
for the degree of
Doctor of Natural Sciences

Put forward by
Holger Eric Jörg
born in: Schwetzingen, Germany
Oral examination: 21$^{th}$ December 2016

# Compton Polarimetry of 6 - 35 keV X-rays: Influence of Breit Interaction on the Linear Polarisation of *KLL* Dielectronic Recombination Transitions in Highly Charged Ions

Referees: Priv.-Doz. Dr. José R. Crespo López-Urrutia
Prof. Dr. Selim Jochim

**Abstract**

The polarisation of X-rays emitted during $K$ shell dielectronic recombination (DR) into highly charged ions was studied using electron beam ion traps. In the first experiment, the degree of linear polarisation of X-rays due to $K$ shell DR transitions of highly charged krypton ions was measured with a newly developed Compton polarimeter based on SiPIN diodes. Such polarisation measurements allow a study of the population mechanism of magnetic sublevels in collisions between electrons and ions. In a second experiment, the influence of Breit interaction between electrons on the polarisation of X-rays emitted during $K$ shell DR into highly charged xenon ions was studied. Here, polarisation measurements provide an access to the finer details of the electron-electron interaction in electron-ion collisions.

Furthermore, a second Compton polarimeter based on silicon drift detectors has been developed for polarisation measurements at synchrotrons. It has been developed for X-ray polarimetry with a high energy resolution for energies between 6 keV and 35 keV. It was tested in the course of polarisation measurements at an electron beam ion trap and at a synchrotron radiation source.

**Zusammenfassung**

Die Polarisation von Röntgenquanten, die in dielektronischer Rekombination (DR) in die K-Schale hochgeladener Ionen erzeugt werden, wurde mithilfe von Elektronenstrahl-Ionenfallen untersucht. In einem ersten Experiment wurde der Grad der linearen Polarisation von Röntgenquanten, welche in K-Schalen DR Übergängen in hochgeladenen Kryptonionen emittiert werden, mit einem neu entwickelten Compton-Polarimeter, welches auf SiPIN Dioden basiert, gemessen. Solche Polarisationsmessungen erlauben eine Untersuchung von Bevölkerungsmechanismen von magnetischen Unterschalen in Kollisionen zwischen Elektronen und Ionen. In einem zweiten Experiment wurde der Einfluss untersucht, den die Breit-Wechselwirkung zwischen Elektronen auf die Polarisation von Röntgenquanten hat, die in K-Schalen DR Übergängen in hochgeladenen Xenonionen emittiert werden. Hier erlauben Polarisationsmessungen einen Einblick in die feinen Details der Elektron-Elektron Wechselwirkung in Kollisionen zwischen Elektronen und Ionen.

Des Weiteren wurde ein zweites Compton-Polarimeter entwickelt, welches auf Silizium-Drift-Detektoren basiert, für Polarisationsmessungen an Synchrotronen. Es wurde für Polarisationsmessungen im Röntgenbereich mit hoher Energieauflösung für Energien im Bereich von 6 keV bis 35 keV entwickelt. Es wurde bei Polarisationsmessungen an einer Elektronenstrahl-Ionenfalle und einer Synchrotronstrahlenquelle getestet.

# Contents

# 1 Introduction

Studying collisional processes in laboratory plasmas of stored highly charged ions (HCI) is a tool to probe our understanding of relativistic particle dynamics under the presence of strong nuclear electromagnetic fields [1]. The dominant radiative processes in collisions between electrons and ions in plasmas, which are radiation excited by electron impact, synchrotron radiation and bremsstrahlung, and electron recombination, exhibit distinct polarisation traits. Analysing the polarisation features of the emitted radiation yields the magnetic sublevel population of excited ionic states, called alignment, which in strong electromagnetic fields shows influences of higher-order multipole transitions [2] [3] and relativistic effects [4] [5]. Furthermore QED contributions are predicted [6] [7].

Nearly ninety years ago in 1927, J. R. Oppenheimer described the polarisation of radiation following electron impact [8]. An atom is excited by electron impact to certain Zeeman components of a higher level. By calculating the probabilities of radiative transitions to the Zeeman components of a lower level, the polarisation of the emitted radiation can be obtained. If the emitted radiation is observed perpendicular to the electron propagation direction, its degree of linear polarisation is defined as $P = (I_{\parallel} - I_{\perp})/(I_{\parallel} + I_{\perp})$ with the intensity of radiation with the electric field vector parallel, $I_{\parallel}$, and perpendicular, $I_{\perp}$, to the electron direction. This theory has then been complemented during the following years to include e.g. effects due to nuclear spin [9]. Early polarisation measurements conducted by A. Ellett et al. in 1926 [10], which showed a polarisation of 30% of the mercury λ2537 line, could then be explained on the basis of alignment production following directional electron impact excitation. In the following decades studies of the polarisation of radiation following electron impact excitation came to include effects due to near threshold excitations [11], as well as experimental [12] and theoretical [13] studies of impact radiation in the X-ray regime.

Studies of the polarisation features of non-resonant electron recombination, i.e. radiative electron capture or radiative recombination, up to the highest charge states of the heaviest ions have been performed theoretically [14, 15, 16] as well as experimentally [5] during the last two decades. Here, for strong electromagnetic fields of HCIs, the influence of higher-order multipole transitions becomes pronounced, as e.g. in the polarisation of the Ly-$\alpha_1$ transition following radiative electron capture into the ionic $L$ shell for $U^{92+}$ [17]. Such polarisation measurements enable studies of the influence E1-M2 mixing has on the alignment of the $2p_{3/2}$ state, see figure 1. For heavy, few electron ions, the electric dipole approximation fails to describe the

alignment of the excited ionic states [18]; multipole-mixing effects may even dominate, as it is the case for the angular distribution of radiative deexcitation lines in resonant electron capture into excited electronic states [19].

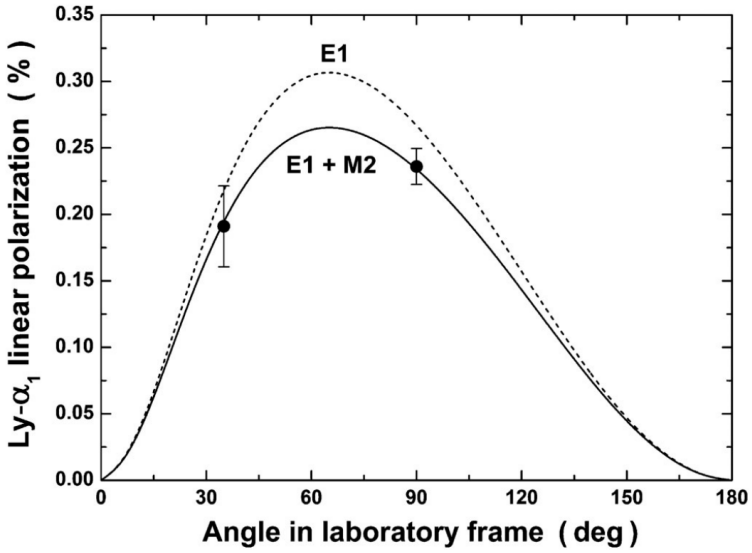


Figure 1: Linear polarisation of the Ly-$\alpha_1$ transition following radiative electron capture. The measured degree of linear polarisation is compared with theory calculations in the electric dipole approximation (E1), dotted line, and also taking E1-M2 mixing into account, solid line. Taken from [17].

Alignment is also studied in resonant electron recombination, e.g. in resonant transfer and excitation (RTE) in collisions between light atoms and HCIs. Here, a loosely bound electron is transferred from the atom to the ion with a simultaneous excitation of an ionic electron. The decay radiation from this excited intermediate state has an anisotropic angular distribution if the intermediate state is aligned [20]. By measuring the angular differential cross section of radiation emitted in RTE in collisions between $U^{91+}$ and hydrogen atoms, relativistic effects in the electron-electron interaction have been shown to influence the alignment of the intermediate state [21] [22]. Studies of the polarisation of the radiation emitted in RTE have up to now not been performed.

A similar resonant electron recombination process to RTE is dielectronic recombination (DR), where, in the first step, an unbound electron is resonantly captured by an ion under simultaneous excitation of a bound electron. An autoionising doubly-excited state is formed. In the second step, this intermediate state decays radiatively [23]. If the recombining electrons have a directionality, the formed intermediate state is aligned and the corresponding DR lines are polarised. DR is a prominent process in collisions of electrons with HCIs. With the electron energy

tuned into a DR resonance, DR even dominates the recombination rate over the non-resonant electron recombination [24]. Theoretical studies about the polarisation of radiation emitted in DR have been started twenty years ago [25] [26], and are still being continued [7]. Up to now, experimental studies on the polarisation of radiation emitted in DR have been sparse. Theoretical research on the polarisation of DR radiation also includes relativistic effects [27]. On the experimental side, Shlyptseva and co-workers [25] [28] have measured polarisation features of dielectronic recombination lines excited by an electron beam in $K$ shell X-ray spectra of highly charged iron ions using a polarisation sensitive Bragg crystal spectrometer. Here only features indicating polarised radiation could be measured and no degree of linear polarisation could be derived. The analysis of polarisation dependent spectra from Bragg polarimeters suffers from a need to account for the crystal reflectivity and its polarisation sensitivity. These inherent difficulties make such polarisation measurements difficult to perform

In diagnostics of hot plasmas, information about the directionality of the plasma electrons can be deduced from measurements of linear polarisation of DR X-ray lines [29] [26]. A high anisotropy in the velocity distribution of the recombining plasma electrons results in a high degree of linear polarisation of DR lines. Anisotropy in the directionality of the plasma electrons also results in an anisotropic X-ray emission, which affects the intensity measurement of DR lines [27, 19, 30]. This, in turn, affects plasma temperature diagnostics, which are performed with DR X-ray lines. For solar flares, for example, the intensity ratio of a DR line $I_s$ to its corresponding principal excitation line in He-like systems $I_w$, due to the direct excitation, $1s2p\,^1P_1^0 \longrightarrow 1s^2\,^1S_0$, has been used as a measure of the plasma electron temperature $T_e$ [31]:

$$\frac{I_s}{I_w} = \frac{\alpha_s}{q_w}\,; \quad \alpha_s = f(T_e) S_{RC}(s) \tag{1}$$

with the recombination rate $\alpha_s(T_e)$ through the DR line, and the rate coefficient $q_w$. The recombination rate through the DR resonance depends on the plasma electron temperature through a temperature dependent term $f(T_e)$ as well as on the resonance recombination strength $S_{RC}$. For the dielectronic capture, the plasma electron energy has to fulfil the resonance condition for a particular ionic excitation level, while for the corresponding principal line, the electron energy just has to be high enough for the threshold of excitation of the core transition. Thus, the ratio $I_s/I_w$ is sensitive to the plasma electron energy distribution and is therefore sensitive to the plasma temperature.

The interest in the polarisation of DR X-rays also arises from the point of view of understanding the basic electron-electron interaction in the extreme regime of strong Coulomb fields of HCIs. DR is the strongest resonant process in electron-ion collisions, and it is as such governed by the electron-electron interaction [24]. The latter is of fundamental importance for atomic and molecular physics as it defines the level structure as well as the dynamics of collision processes. In the non-relativistic limit, the interaction between electrons is given by the Coulomb interaction. In the strong fields of heavy HCI, the Breit interaction modifies their interaction potential. The (generalised) Breit interaction (BI) encompasses the lowest-order QED effects in electron-electron interactions; it includes the retardation in the exchange of a single virtual photon between the electrons as well as magnetic effects [32]. BI is often viewed as a correction to the Coulomb interaction since it causes only small shifts in the energy levels in atoms and ions. BI becomes pronounced for collisional processes involving deep inner-shell electrons in heavy ions, as e.g. in the $1s$ electron impact ionisation cross section for H-like uranium, which it enhances by about 50% [33]. In collisions between electrons and HCIs, BI has a strong influence on the DR resonance strength for heavy HCI [32] [34]. In Li-like system, for example, the BI contribution increases with the atomic number Z, see figure 2.

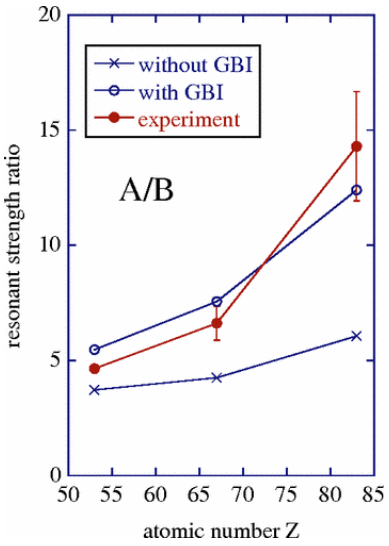


Figure 2: Resonance strength ratios between two DR resonances into Li-like iodine (Z=53), holmium (Z=67) and bismuth (Z=83) ions. Resonance B, with the intermediate state $[1s2s2p_{1/2}^2]_1$, is not influenced by BI, while resonance A, with the intermediate state $[1s2s^22p_{1/2}]_1$, shows a strong influence. Taken from [32].

One of the strongest effects of Breit interaction on the electron-electron interaction in collisions between electrons and ions was predicted by S. Fritzsche et al. to be on the linear polarisation of DR X-rays [6]. For the specific DR resonance of initially Li-like ions, called $Li_1$, populating the intermediate state $[1s2s^2 2p_{1/2}]_1$, the influence of BI interaction was predicted to reverse the polarisation direction of electric-dipole radiation emitted in the radiative decay, see figure 3. Here, BI increasingly dominates the Coulomb repulsion in the interaction between the free and the bound electron of ions with higher atomic numbers $Z$. Thus, measuring the polarisation of DR X-rays is one of the most sensitive probes of the electron-electron interaction in the presence of strong Coulomb fields of heavy nuclei.

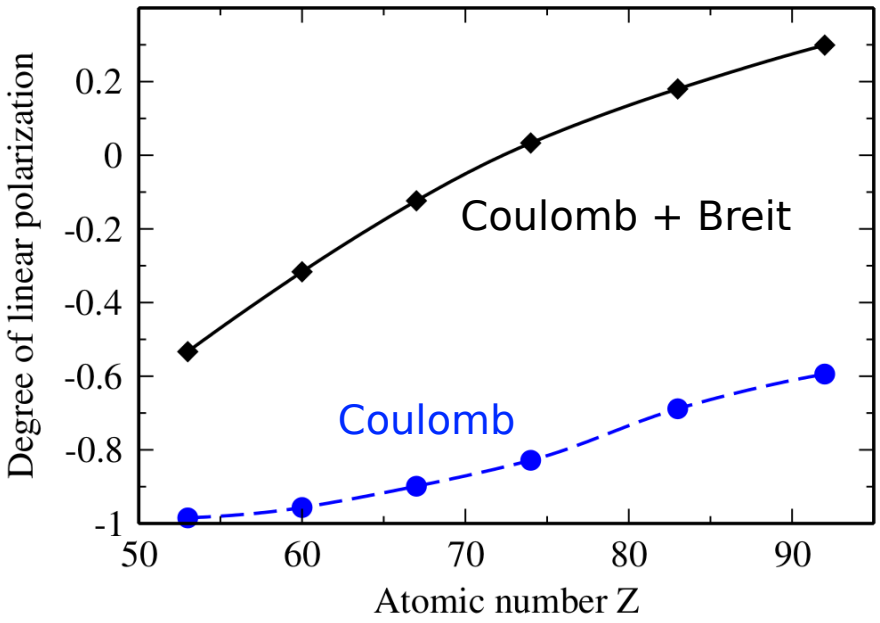


Figure 3: Theoretical calculations of the degree of linear polarisation of the DR X-ray emission for the decay from the intermediate state $[1s2s^2 2p_{1/2}]_1$, observed at an angle perpendicular to the recombining electron propagation direction. Taken from [6]

In 2014, Z. Hu et al. [35] measured the atomic number dependence of the magnetic sublevel population in the autoionising state formed in the $Li_1$ DR resonance, combining X-ray and DR resonance strength measurements. Their measurements were performed at the Electron Beam Ion Trap (EBIT) in Tokyo, a device capable of producing and trapping HCIs. The DR resonance strengths were obtained by measuring the ion abundance in the trap. This introduces uncertainties due to ion escape from the trap and multiple charge exchange in collisions between the HCIs and the residual gas in the trap. Their measurements demonstrate the influence

BI has on the alignment of the intermediate state for heavier ionic systems, albeit with substantial relative uncertainties, see figure 4. Including relativistic effects like BI leads to a higher population of magnetic sublevels whose population is strongly suppressed in the non-relativistic level, i.e. sublevels with the magnetic quantum number $m_d = 0$.

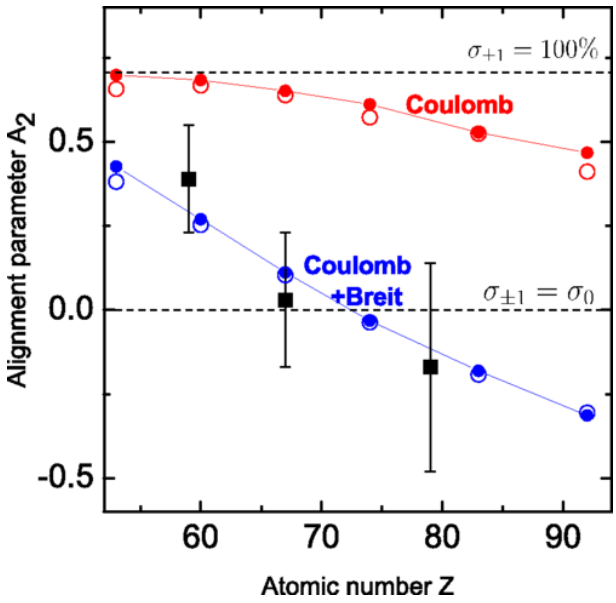


Figure 4: Alignment parameter $\mathcal{A}_2$ for the intermediate state $[1s2s^2 2p_{1/2}]_1$ in DR of Li-like Pr, Ho and Au. The experimental results are shown by black squares. Theoretical values are plotted as red and blue dots. Solid circles refer to calculations with the flexible atomic code [36], while open circles refer to calculations with the RATIP code [37]. Taken from [35]

This thesis work describes a more direct approach to study the influence of BI on the alignment of the intermediate state in the $Li_1$ DR resonance. A dedicated semiconductor based Compton polarimeter was employed to measure the polarisation of DR X-ray lines of two ion species, krypton ($Z = 36$) and xenon ($Z = 54$). With these measurements, the influence BI has on the polarisation of the X-ray radiation of the $Li_1$ resonance was clearly resolved. This more direct access to the alignment of the intermediate state formed in the $Li_1$ resonance, in comparison to the experiment performed by Hu et al., yields lower uncertainties in studying the influence BI has on the electron-electron interaction.

Two Compton polarimeters for the X-ray energy region of 6 - 35 keV, where most of the transitions in mid-$Z$ HCIs are, are presented in this thesis. The first prototype, which is based on silicon PIN (SiPIN) diodes, was specially designed for alignment studies at EBITs. With its detector chips operating at room temperature, it has an energy resolution of 3.5 keV at 13 keV. This was sufficient to measure the

polarisation of X-ray DR lines of mid-$Z$ HCIs. For the next generation the goal was a higher energy resolution, which was achieved by implementing Peltier cooled silicon drift detector (SDD) chips. This new generation has an energy resolution of 600 eV at 13 keV. It is designed for experiments at synchrotron radiation sources. Here, single transitions of HCIs can be studied by resonant single-photon excitation, which provides a much cleaner environment for polarisation measurements. Test measurements with the new polarimeter generation at the Petra III synchrotron radiation source in Hamburg are presented in this thesis, see chapter 6.3.

The polarimeters use the polarisation dependent Compton angular scattering distribution to measure the degree of linear polarisation of X-rays in the energy region of 6 - 35 keV. X-ray polarisation measurements on HCIs in this energy region have been difficult to conduct for a number of reasons. For ions much heavier than iron, $K$ shell X-rays are out of the useful range of Bragg crystal polarimeters [25]. For Compton polarimetry, the low energy threshold has been at 60 keV for most of the 20th century. For X-rays with energies below this threshold, the efficiency of Compton scattering becomes small. Germanium-based polarimeters have been used for X-ray energies above 60 keV up to the MeV range [5] [38] [39]. They have been used, for example, to measure the degree of linear polarisation of radiative electron capture into the $K$ shell of bare uranium ions with an X-ray energy at 250 keV [5].

The development of polarimeters for the low energy region of hard X-rays is not only relevant for fundamental atomic physics research but also for studies of astrophysical plasmas. Here X-ray and gamma ray polarimetry is used to pinpoint the source of radiation from astrophysical plasmas like pulsars [40] and black holes [41]. The degree and angle of radiation from such sources also yields information about the emission mechanisms of their radiation, the geometry and orientation of the source. So far X-ray and gamma ray polarimetry has only been performed for the Crab, a pulsar with its associated nebula. For the X-ray region, at 2.6 keV and 5.2 keV, the degree of linear polarisation is 19.2% and 19.5% with an angle of 156.4° and 152.6°[42], see figure 5. For the gamma range for 100 keV to 1 MeV, it is (46±10)% with an angle of (123±11)° [40]. The measured degrees of polarisation confirm the X-ray emission mechanism as synchrotron radiation. The high degree of polarisation of the gamma rays indicates that they originate from a site close to the neutron star because such high degrees of polarisation need a highly structured magnetic field. The angle of polarisation of the X-ray emission, on the other hand, suggests a different production site.

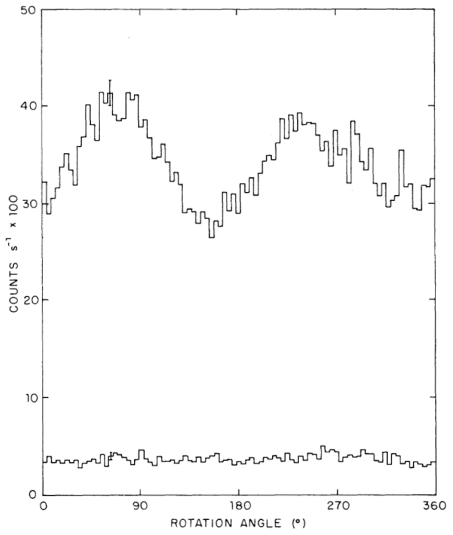


Figure 5: Modulation curves obtained at 2.6 keV during (upper curve) observations of the Crab nebula and during (lower curve) observations of the instrumental background. Taken from [42]

Moreover, the laboratory polarisation measurement techniques and data are useful for the future X-ray satellite missions where X-ray polarimetry is the goal, as e.g. XIPE (*X-ray Imaging Polarimetry Explorer*) [43], with its goal to study anisotropies in astrophysical plasmas like active galactic nuclei, or the observatory *ASTROSAT* [44], which is planned to house a Compton polarimeter for polarimetry measurements on cosmic X-ray sources in the energy regime form 100 keV to 250 keV.

As mentioned in the preceding paragraphs, in this thesis work, X-ray polarisation measurements have been performed to study the influence Breit interaction has on the electron-electron interaction in collisions between electrons and ions. For further research at synchrotron radiation sources, a new generation of Compton polarimeters has been developed and tested at two X-ray radiation sources. Such polarisation studies are necessary for diagnostics of astrophysical and laboratory plasmas.

## 1.1 Organisation of the Thesis

This thesis is organised as follows:

- Chapter 2 introduces the theoretical background of the Dirac theory and Breit interaction which is used to describe the electron-electron interaction. The two main electron-ion recombination processes relevant for this thesis, dielectronic and radiative recombination, are discussed. The density matrix formalism is introduced which describes the population of magnetic sublevels in DR and it is used to derive the polarisation of DR lines. Furthermore the interaction processes of photons with matter relevant for the experimental setups is discussed.

- Chapter 3 deals with the experimental setups for the alignment measurements consisting of EBITs, which produce and trap HCIs. Furthermore a Compton polarimeter based on silicon PIN diodes is presented.

- Chapter 4 describes an experiment on the linear polarisation of DR into highly charged krypton ions, in which the magnetic sublevel population of the intermediate state was studied.

- Chapter 5 depicts an experiment on the influence Breit interaction has on the polarisation of a specific DR resonance in highly charged xenon ions, labelled $\mathrm{Li}_1$, with the intermediate state $[1s2s^2 2p_{1/2}]_1$. Here Breit interaction leads to a significant change in the population of magnetic sublevels and hence the polarisation of this line.

- Chapter 6 describes a newly developed generation of Compton polarimeters based on SDD chips, which offer an improved energy resolution. Results of the first polarisation measurements with this new detector generation performed at an EBIT are discussed. The characterisation of the new polarimeter was done at the synchrotron radiation source, Petra III, in Hamburg.

- Chapter 7 concludes this thesis and offers an outlook on how this work can be applied in further research.

# 2 Theoretical Description

## 2.1 Dirac Theory and Breit Interaction

Breit interaction is the name given to the combined magnetic and relativistic contributions to the electron-electron interaction. To motivate and derive the Breit interaction operator, the Schrödinger equation and the Hamilton operator are introduced, which offer a non-relativistic description of the dynamics of quantum mechanical states. It is used to derive energy levels of bound states of one-electron ions. The Dirac equation, the central relativistic quantum mechanic equation of motion, is also solved for bound states of one-electron ions. For systems with more than one electron interactions between electrons have to be taken into account. Starting from the Lagrangian of an electron moving in the electromagnetic field of another electron, retarded potentials in Lorenz gauge are introduced to derive the classical Breit operator, which is used throughout this thesis to account for magnetic and retardation effects in the electron-electron interaction. For more detailed information about the Schrödinger equation, Dirac theory and energy levels of bound states of one electron ions, references [45], [46], [47] and [48] can be consulted. The following chapters are based on these textbooks.

### 2.1.1 Schrödinger Equation

The Schrödinger equation is the central non-relativistic equation of motion in quantum mechanics. It describes the dynamics of quantum mechanical states, their temporal evolution. It cannot be derived from first principles; it can only be justified using the correspondence principle [45]. The Hamilton operator $\mathcal{H}$ determines the dynamics of the system and possible energy eigenvalues $E$.

$$\mathcal{H}_{(\vec{x},t)} \left|\psi_{(\vec{x},t)}\right\rangle = E \left|\psi_{(\vec{x},t)}\right\rangle = i\hbar \frac{\partial}{\partial t} \left|\psi_{(\vec{x},t)}\right\rangle \tag{2}$$

The wave function $\psi_{(\vec{x},t)}$ describes the quantum state of the system. It contains all information about the system. All possible wave functions form an abstract vector space, the Hilbert space. $|\psi_{(\vec{x},t)}\rangle$ is the state vector which represents a particular state of the system at a given time $t$. The Hamilton operator can also be "derived" from the correspondence principle.

$$\mathcal{H}_{(\vec{x},t)} = E_{kin} + E_{pot} = -\frac{\hbar}{2m}\Delta + V_{(\vec{x},t)} \tag{3}$$

$m$ is the mass of the system, $\Delta$ the Laplacian and $V_{(\vec{x},t)}$ the potential.

The Schrödinger equation can be analytically solved for bound states of one-electron ions [46]. The Coulomb potential, $V_C = -\frac{Ze}{r}$, with Z as nuclear charge number and $r = |\vec{x}|$, describes the interaction between electron and nucleus. This two-particle problem can be equivalently described as a single particle with mass $\mu = \frac{m_e M_k}{m_e + M_k}$ moving in the potential $V = -\frac{Ze^2}{r}$. In spherical coordinates, $\vec{x} \longmapsto (r, \theta, \phi)$, the isotropy of the potential enables us to separate the Schrödinger equation and thus the wave function in a radial and angular part: $\psi_{(r,\theta,\phi)} = R_{(r)}\Omega_{(\theta,\phi)}$. The equation for the radial part

$$[-\frac{\hbar^2}{2\mu}\frac{d^2}{dr^2} - \frac{\hbar^2}{r}\frac{d}{dr} + \frac{\hbar^2 l(l+1)}{2\mu r^2} - V_r]R_{n,l(r)} = E_{n,l}R_{n,l(r)} \tag{4}$$

with n as principal quantum number and l as angular momentum quantum number yields the energy eigenvalues and radial wave functions

$$E_{n,l} = E_n = -\frac{1}{2}\mu c^2 \frac{(\alpha Z)^2}{n^2} \;\; ; \quad R_{n,l(r)} = e^{-r/na_0} r^l L_{n,l} \tag{5}$$

with the associated Laguerre polynomials $L_{n,l}$. The angular part of the Schrödinger equation is solved by the spherical harmonics $\mathcal{Y}_{l,m(\theta,\phi)}$, with the magnetic quantum number $m$. The quantum numbers $l$ and $m$, with $l < n$ and $m = -l, .., l$, define the angular momentum $L = \hbar\sqrt{l(l+1)}$ and its projection on the quantisation axis, here the z-direction, $L_z = m\hbar$. The states with different $m$ for given $n, l$ are called magnetic sublevels. In this non-relativistic treatment the energy of the eigenstates depends only on the principal quantum number $n$. Experimental results show a finer level structure which can be explained in a relativistic treatment of one-electron ions.

### 2.1.2 Dirac Equation

The Dirac equation is the central relativistic equation of motion in quantum mechanics, describing spin-1/2 particles. The Schrödinger equation, with its linear derivation with respect to the time coordinate and its second derivation with respect to the position coordinate, violates the symmetry requirements of special relativity [47]. The Dirac equation is linear in its spatial coordinates, which satisfies relativistic covariance [48]

$$\mathcal{H}_{D(\vec{x},t)} \left|\psi_{(\vec{x},t)}\right\rangle = (c\hat{\vec{\alpha}}\vec{p} + \hat{\beta}m_0c^2) \left|\psi_{(\vec{x},t)}\right\rangle = E \left|\psi_{(\vec{x},t)}\right\rangle = i\hbar\frac{\partial}{\partial t} \left|\psi_{(\vec{x},t)}\right\rangle \tag{6}$$

with

$$\hat{\alpha_i} = \begin{pmatrix} 0 & \sigma_i \\ \sigma_i & 0 \end{pmatrix} \quad ; \quad \sigma_1 = \begin{pmatrix} 0 & 1 \\ 1 & 0 \end{pmatrix}, \sigma_2 = \begin{pmatrix} 0 & -i \\ i & 0 \end{pmatrix}, \sigma_3 = \begin{pmatrix} 1 & 0 \\ 0 & -1 \end{pmatrix} \tag{7}$$

$$\hat{\beta} = \begin{pmatrix} 1 & 0 & 0 & 0 \\ 0 & 1 & 0 & 0 \\ 0 & 0 & 1 & 0 \\ 0 & 0 & 0 & -1 \end{pmatrix} \tag{8}$$

The $\sigma_i$ are the Pauli matrices. The Dirac equation is an equation of motion for 4-component spinors:

$$\psi_{(\vec{x},t)} = \begin{pmatrix} \psi_A \\ \psi_B \end{pmatrix} \quad \text{with} \quad \psi_A = \begin{pmatrix} \psi_{1(\vec{x},t)} \\ \psi_{2(\vec{x},t)} \end{pmatrix} \quad \text{and} \quad \psi_B = \begin{pmatrix} \psi_{3(\vec{x},t)} \\ \psi_{4(\vec{x},t)} \end{pmatrix} \tag{9}$$

The upper components $\psi_A$ are interpreted as the spin states for regular particles, while the lower components $\psi_B$ are interpreted as the spin states for their antiparticles.

The Dirac equation can also be analytically solved for bound states of one-electron ions [47] if we assume that the nucleus rests in space and the much lighter electron is moving in its potential. The Dirac equation for this system consists of two coupled differential equations, one for the upper and another for the lower components.

$$\vec{\sigma}\vec{p}\psi_B = \frac{1}{c}(E - V_{\vec{x}} - m_0c^2)\psi_A \; ; \quad \vec{\sigma}\vec{p}\psi_A = \frac{1}{c}(E - V_{\vec{x}} + m_0c^2)\psi_B \tag{10}$$

These equations are again solved using a separation ansatz

$$\psi_{A\ jlm\ (r,\theta,\phi)} = ig_{(r)}\mathcal{Y}_{jlm\ (r,\theta,\phi)} \; ; \quad \psi_{B\ jlm\ (r,\theta,\phi)} = -f_{(r)}\mathcal{Y}_{jlm\ (r,\theta,\phi)} \tag{11}$$

where $j$ is the total angular momentum quantum number with $\vec{j} = \vec{l} + \vec{s}$. Here $\vec{s}$ is the spin of the particle, with its quantum number $s$, defining its length $S = \hbar\sqrt{s(s+1)}$ and its projection on the quantisation axis $s_z = m_s\hbar$ with $m_s = -s, ..., s$. In this case the particle is an electron, a spin-1/2 particle, which means that $s = 1/2$. The total angular momentum has the length $J = \hbar\sqrt{j(j+1)}$ with $|l - s| < j < |l + s|$. For the radial equation, this yields ordinary coupled differential equations for $g_{(r)}$ and $f_{(r)}$.

$$-(E + m_0c^2 - V)f + \hbar c(\frac{dg}{dr} + \frac{\kappa + 1}{r}g) = 0 \tag{12}$$

$$(E - m_0c^2 - V)g + \hbar c(\frac{df}{dr} + \frac{1 - \kappa}{r}f) = 0 \tag{13}$$

with the Dirac quantum number

$$\kappa = \mp(j + 1) \begin{cases} -l - 1 & \text{for } \; j = l + 1/2 \\ l & \text{for } \; j = l - 1/2 \end{cases} \tag{14}$$

Solving the radial equations yields the energy eigenvalues

$$E_{n,j} = m_0c^2\sqrt{1 + \frac{(Z\alpha)^2}{(n - \delta_j)^2}} \quad \text{with} \quad \delta_j = j + \frac{1}{2} - \sqrt{(j + \frac{1}{2})^2 - (Z\alpha)^2} \tag{15}$$

In the relativistic Dirac theory, the energy eigenvalues of the system electron-ion depend on the principal quantum number $n$ and the total angular momentum quantum number $j$. This is in line with experimental observations. To highlight the connection with the non-relativistic theory, we expand equation (15) in powers of $(Z\alpha)^2$.

$$E_{n,j} = m_0c^2[1 - \frac{(Z\alpha)^2}{2n^2} - \frac{(Z\alpha)^4}{2n^3}(\frac{1}{j + 1/2} - \frac{3}{4n}) + ...] \tag{16}$$

The zero order term $(Z\alpha)^0$ represents the rest energy of the electron, the first order term term represents the energy eigenvalues of the non-relativistic theory, and the second order term encompasses the relativistic corrections, which are also called fine-structure corrections.

Further corrections are necessary to account for effects measured at higher precision. Taking the spin of the nucleus into account leads to the so called hyperfine corrections. Furthermore there are discrepancies between Dirac theory and experimental observations which can only be explained in the framework of quantum electrodynamics. The most prominent one are the corrections deriving from the interactions of the electron with its own radiation field, the self-energy of the electron.

### 2.1.3 Breit Interaction

For systems with more than one electron, the interaction between electrons has to be taken into account. In addition to the Coulomb potential in the electromagnetic

interaction of two or more massive spin-1/2 particles, Breit interaction accounts for retardation and magnetic interactions between two electrons. Retardation effects become strong for electrons in heavy ions, as their velocity scales with the atomic number of the ion. Breit interaction is often interpreted as a correction to the Coulomb potential. In the years 1929-32, Gregory Breit published a series of papers [49] [50] [51] deriving this correction term for the Dirac Hamiltonian. To derive these corrections, we look at the Lagrangian of an electron moving in an electromagnetic field caused by another moving electron with the potential $(\phi, \vec{A})$, see figure 6.

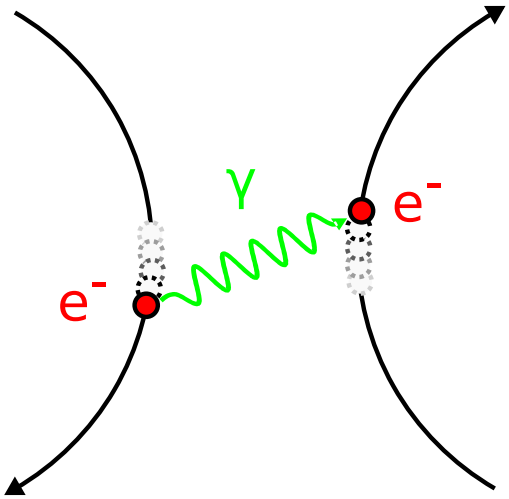


Figure 6: Illustration of retardation effects in the interaction between two electrons. An electron moves in the electromagnetic field caused by another electron moving at relativistic energies.

$$\mathcal{L}_1 = \mathcal{L}_{1(\vec{x_1},\vec{v_1})} = -\gamma mc^2 - e\phi + \frac{e}{c}\vec{A}\vec{v_1} \tag{17}$$

with the retarded potentials in Lorenz gauge

$$\phi_{\vec{x},t} = \int \frac{1}{R}[\rho_{(\vec{r}',t')}]_{ret} d^3r' \;\; ; \quad \vec{A}_{\vec{r},t} = \int \frac{1}{cR}[\vec{j}_{(\vec{r}',t)}]_{ret} d^3r' \tag{18}$$

$$\text{with} \quad \vec{R} = \vec{x}_1 - \vec{x}_2 \quad \text{and} \quad [...]_{ret} = [...]_{t'=t-R/c} = \sum_{n=0}^{\infty} \frac{(-1)^n}{n!}(\frac{R}{c})^n \partial_t [...] \tag{19}$$

We expand the Lagrangian around $t$ in powers of $R/c$, cut off the Taylor expansion after the second term and do the following gauge transformation

$$\phi' = \phi - \frac{1}{c}\partial_t f \;\; ; \quad \vec{A}' = \vec{A} + \vec{\nabla} \quad \text{with} \quad f := \frac{e}{2c}\partial_t R \tag{20}$$

which yields the 2nd order Darwin Lagrangian, also known as classical Breit interaction.

$$\mathcal{L}^{(2)}_{1,2} = \frac{e^2}{c^2 R}\vec{v_1}\vec{v_2} - \frac{e^2}{2c^2 R}\vec{v_1}\vec{v_2} + \frac{e^2}{2c^2 R^3}(\vec{v_1}\vec{R})(\vec{v_2}\vec{R}) \tag{21}$$

The first term is the magnetostatic current-current interaction and the second and third term together are the retarded electric interaction or scalar interaction. With the replacement $\vec{v} = \frac{i}{\hbar}[\vec{x}, \mathcal{H}_D] = c\vec{\alpha}$, we arrive at the classical Breit interaction Hamiltonian

$$\mathcal{H}_B = \frac{\vec{\alpha_1}\vec{\alpha_2}}{2\vec{R}} + \frac{(\vec{\alpha_1}\vec{R})(\vec{\alpha_2}\vec{R})}{2\vec{R}^3} \tag{22}$$

In the framework of quantum electrodynamics, a more precise theory of Breit interaction, the generalised Breit interaction [52], can be derived. Considering the first-order Feynman diagram of electron-electron interaction, the exchange of a virtual photon, the potential for Breit interaction is found to be

$$V_B = \sum_{i<j}(-(\vec{\alpha_i}\vec{\alpha_j})\frac{exp(i\omega R_{ij})}{R_{ij}} + (\vec{\alpha_i}\vec{\nabla}_i)(\vec{\alpha_j}\vec{\nabla}_j)\frac{exp(i\omega R_{ij}) - 1}{\omega^2 R_{ij}}) \tag{23}$$

with $\omega$ as the frequency of the exchanged photon and $R_{ij} = |\vec{x_i} - \vec{x_j}|$. The classically derived Breit interaction operator is the limit of the generalised Breit interaction operator as $\omega \longrightarrow 0$ [53]. Only for high-Z ions, for which $\omega$ increases, it becomes necessary to use the generalised Breit interaction operator.

Breit interaction becomes more pronounced at relativistic energies. For highly charged ions, this means the effect of Breit interaction can be observed for high-Z systems with relativistic electrons. Still its effect on binding energies [54] is relatively small. Its effect on dynamic processes with more than one electron involved, e.g. dielectronic recombination, is predicted to be substantial [6].

## 2.2 Interaction of Photons with Matter

The following chapter discusses the major processes of interactions between photons and matter, which are relevant for the detectors and experimental setups used in this thesis. For the photon energies in our experiments, the relevant processes are the photoelectric effect, Compton and Rayleigh Scattering. The X-ray energies relevant for this thesis work, 6 keV to 35 keV, are too small for pair production. The relevant materials are silicon, beryllium and boron carbide ($B_4C$). In the Compton polarimeters used in this thesis work, the detector chips are made of silicon, whereas the scattering materials are made of either beryllium or boron carbide. Silicon has a high photoelectric absorption cross section in the relevant energy range, which makes it suitable as a material for detector chips, see figure 7. Beryllium and boron carbide have a high Compton scattering cross section for X-ray energies between 6 keV and 35 keV, which are of similar strength as their photoabsorption cross sections, see figures 8 and 9. They are used as scattering material.

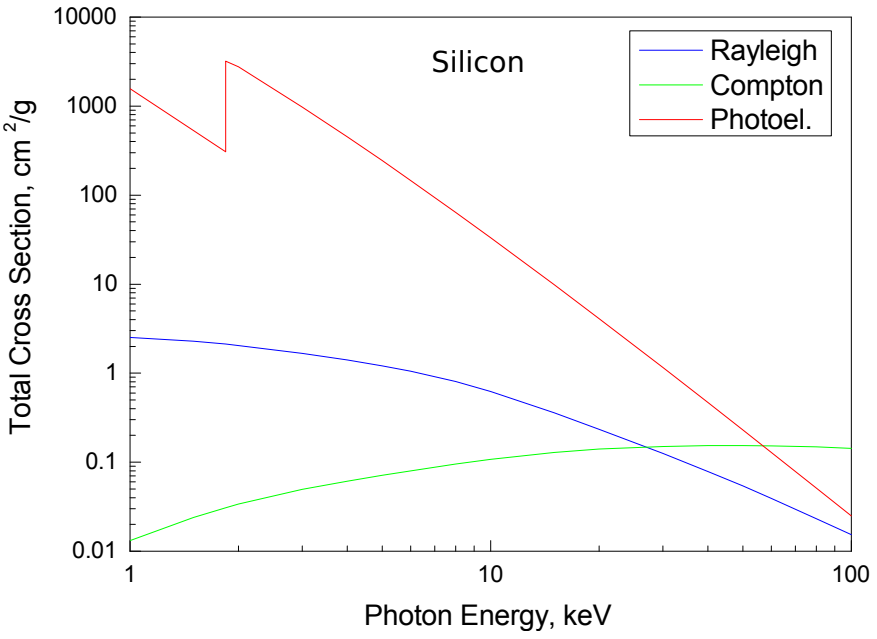


Figure 7: Photon cross sections for photoelectric absorption and scattering in silicon in the energy range between 1 and 100 keV. Data obtained from NIST photon cross sections database [55].

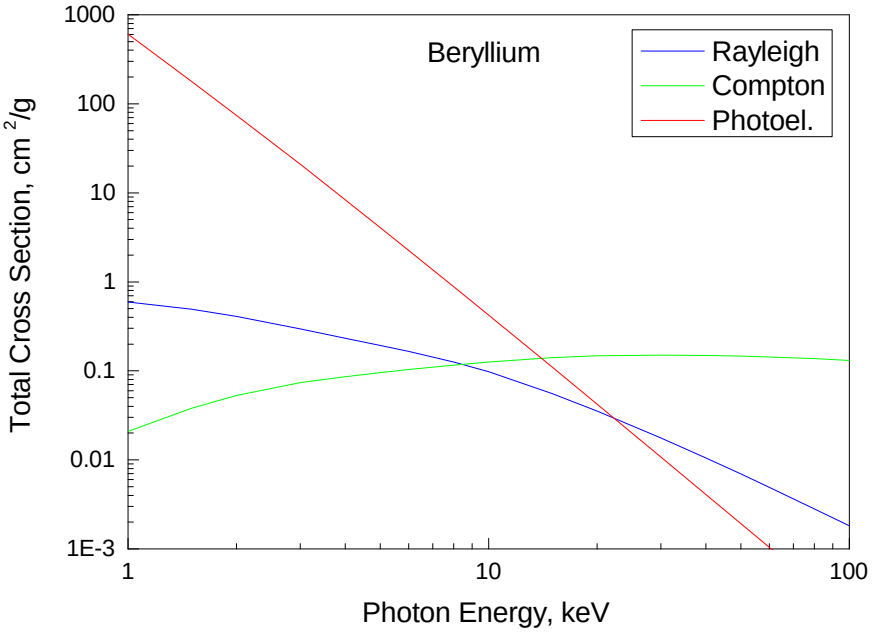


Figure 8: Same as figure 7, except for beryllium.

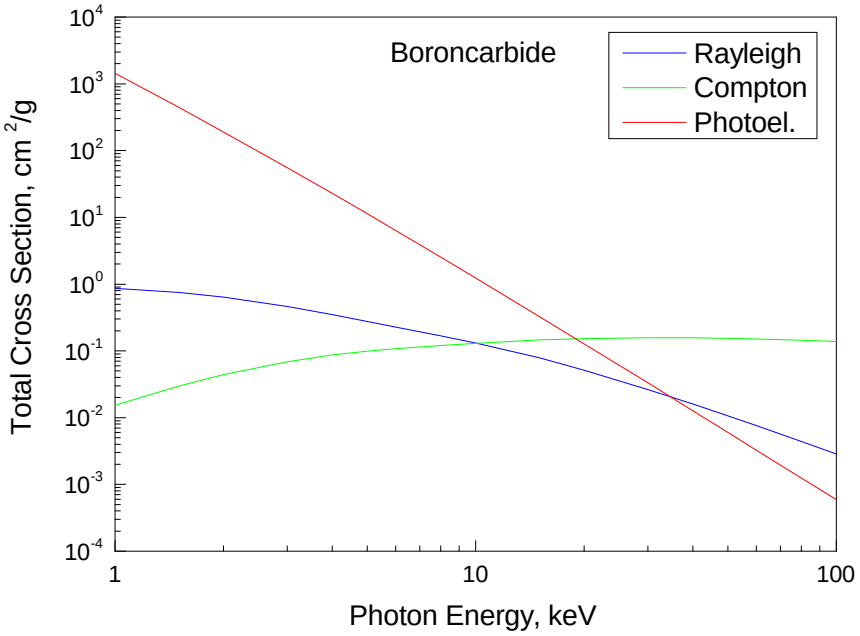


Figure 9: Same as figure 7, except for boroncarbide.

### 2.2.1 Photoelectric Effect

The photoelectric effect describes the total absorption of a photon with energy $E_\gamma = \hbar\omega$, with $\omega$ as the frequency of the photon, and the subsequent emission of an electron, see figure 10. The energy of the emitted electron is:

$$E = E_\gamma - E_{\text{bind}} \tag{24}$$

with the binding energy of the electron $E_{\text{bind}}$. The total cross section of the photoelectric effect is [56]:

$$\sigma_{\text{photo}} \propto \frac{Z^n}{(\hbar\omega)^{7/2}} \tag{25}$$

which is the probability of photoelectric absorption per interaction between a photon and an atom. The parameter n, with 4<n<5, depends on the photon energy. $Z$ represents the atomic number of the atom of the bound electron.

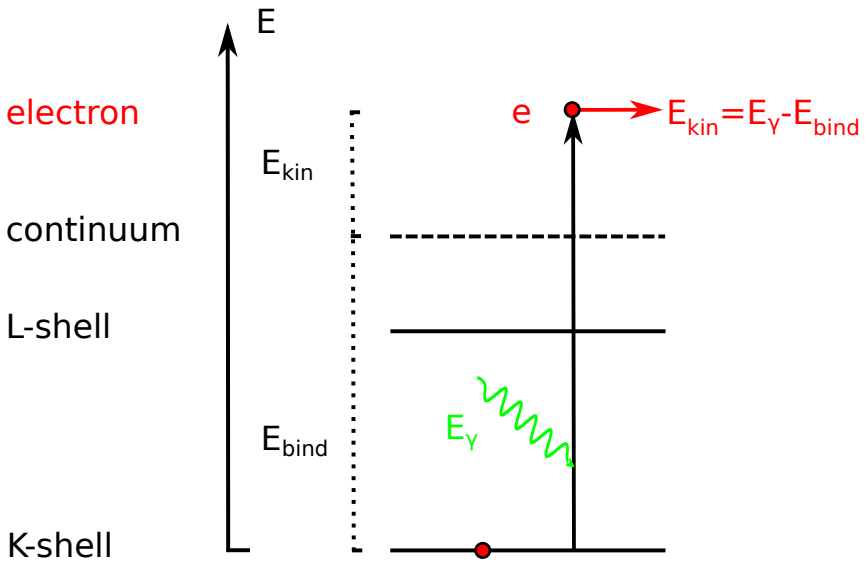


Figure 10: Illustration of the photoelectric effect. A photon with energy $E_\gamma$ is absorbed by an atom and simultaneously an electron with energy $E_{kin}=E_\gamma-E_{bind}$ is emitted.

For the materials used in the polarimeter setups, the photoelectric effect predominates the interaction between X-rays and the polarimeter materials for X-ray energies below 10 keV and is still a strong process for energies up to 20 keV. Equation (25) is not valid for photon energies close to the electron binding energies.

These electron binding energies can be seen in the cross section graph as "absorption edges", e.g. for the $K$ shell of silicon at an energy of 1.84 keV, see figure 7.

### 2.2.2 Compton Scattering

In Compton scattering, a photon with energy $\hbar\omega$ scatters inelastically off a free or weakly bound electron, see figure 12. Energy and momentum conservation yield the energy of the scattered photon and the electron [57].

$$E_{\text{photon}} = \frac{\hbar\omega}{1 + \frac{\hbar\omega}{m_e c^2}(1 - cos\theta)} \;\; ; \quad E_{\text{electron}} = \hbar\omega \frac{\frac{\hbar\omega}{m_e c^2}(1 - cos\theta)}{1 + \frac{\hbar\omega}{m_e c^2}(1 - cos\theta)} \tag{26}$$

where $\theta$ is the polar scattering angle. The kinematics of Compton scattering are shown in figure 11 for three energies of the incoming photon, 13 keV, 31 keV and 100 keV. The energy transfer from the incoming photon to the electron becomes bigger with larger photon energies and bigger scattering angles $\theta$. For the energy range of interest for us, from 6 keV to 35 keV, the energy of the recoil electron is very small, below 3 keV. At even smaller photon energies, the energy transfer to the electron becomes negligible. This low energy limit of Compton scattering is known as the Thomson limit. It is the classical limit where no energy is transferred to the electron. The photon scatters elastically off the electron in a process called Thomson scattering. The classical Thomson cross section is $\sigma_{\text{Thomson}} = \frac{8\pi}{3} r_e^2 = 6.65 \cdot 10^{-25} \text{cm}^2$ [57]. The differential cross section of Thomson scattering is [57]

$$\frac{d\sigma}{d\omega} = r_e^2 (\vec{\epsilon} \cdot \vec{\epsilon}\,')^2 \tag{27}$$

with the incident and scattered radiation electric polarisation vectors $\vec{\epsilon}$ and $\vec{\epsilon}\,'$.

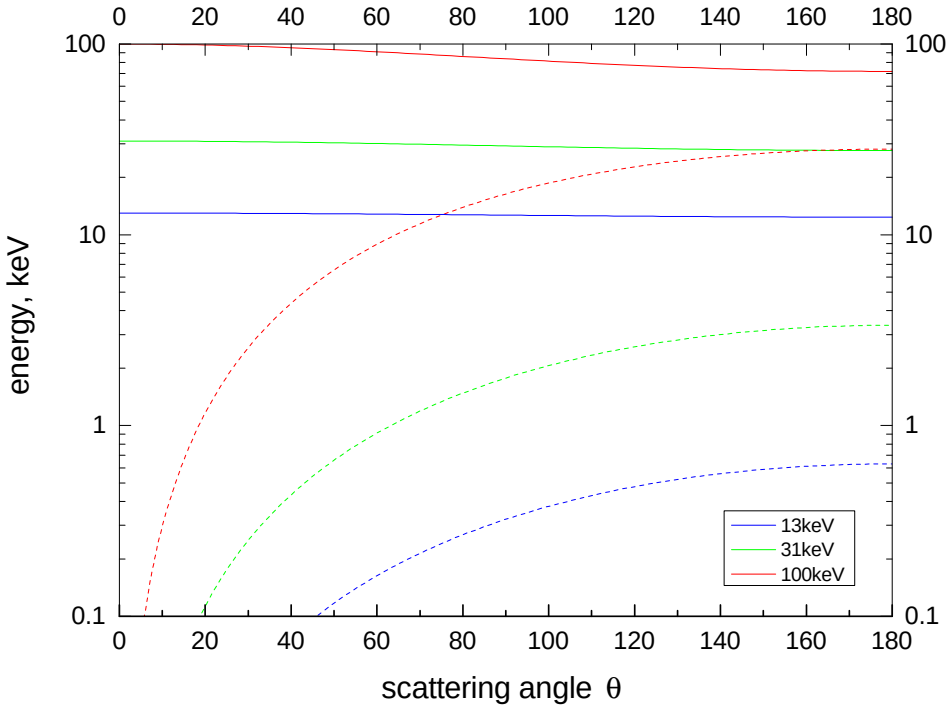


Figure 11: Kinematical relationships in Compton scattering. Energy of the scattered photon - solid line - and scattered electron - dashed line - for different energies of the incoming photon: 13 keV - blue, 31 keV - green and 100 keV - red. The data is derived from equation (26).

The Klein-Nishina formula describes the angular scattering distribution of photons scattered off a single free electron into the solid angle element $d\Omega$ in the lowest order of quantum electrodynamics [5]

$$\frac{d\sigma}{d\Omega} \propto \frac{\hbar\omega'}{\hbar\omega} + \frac{\hbar\omega}{\hbar\omega'} - sin^2\theta - Psin^2\theta\, cos(2(\varphi - \varphi_0)) \tag{28}$$

with the polar scattering angle $\theta$, the azimuthal scattering angle $\varphi$, the degree of linear polarisation P and the angle of linear polarisation $\varphi_0$ of the photon. This sensitivity of the angular azimuthal scattering distribution on the degree and angle of linear polarisation of the photon is exploited in Compton polarimetry.

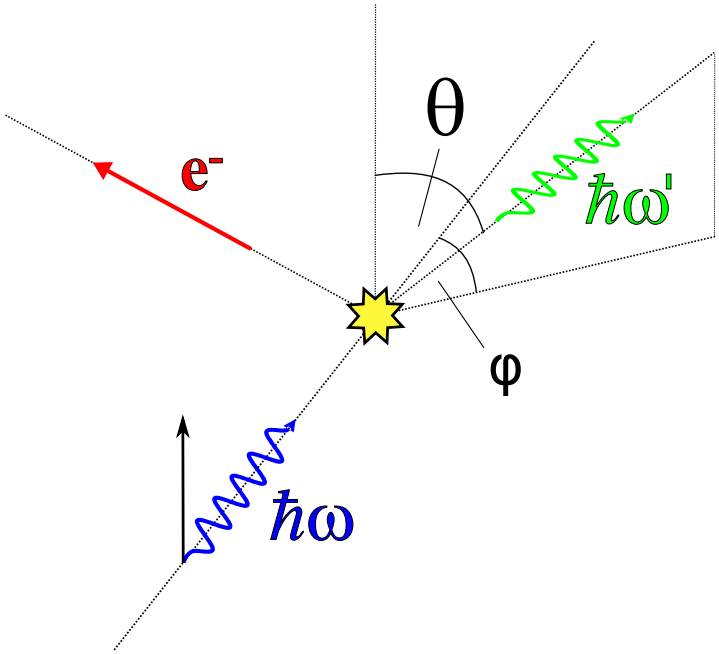


Figure 12: Illustration of Compton scattering. A photon (blue) is scattered off an electron (red). The angular differential scattering distribution of scattered photon (green) is given by the Klein-Nishina formula

### 2.2.3 Rayleigh Scattering

In Rayleigh scattering, photons scatter coherently off bound electrons in atoms. No electrons are emitted. The nucleus absorbs the full recoil momentum. More than one electron can participate, including effects of resonances and phase coherences between multiple electrons. For photon energies much higher than $E_{bind}$ and smaller than 2 keV, the differential cross section for Rayleigh scattering is:

$$\frac{d\sigma}{d\omega} = Z^2 r_e^2 (\vec{\epsilon} \cdot \vec{\epsilon}')^2 \tag{29}$$

which is the Thomson scattering cross section, see equation (27), multiplied by the number of electrons $Z$ in the atom. For higher energies, the cross section becomes [58]:

$$\sigma_{Rayleigh} = \pi r_e^2 \int_{-1}^{1} (1 + cos^2\theta) f^2(\theta) d(cos\theta) \tag{30}$$

with the form factor $f(\theta)$, which goes to 0 for non-zero angles and photon energies higher than 5 keV. Photons scattered in Rayleigh scattering deposit little energy

to the recoil atom. Energy and momentum conservation yield the following energy of the scattered photon.

$$\hbar\omega' = \frac{\hbar\omega}{1 + \frac{\hbar\omega}{M_{Atom}c^2}} \tag{31}$$

## 2.3 Electron-Ion Recombination

Electron-ion recombination encompasses fundamental atomic processes which control the state of matter in plasmas as well as atomic level populations. Relevant processes for this thesis work are dielectronic recombination (DR) and radiative recombination (RR); another process is bremsstrahlung, the recombination of an electron into a continuum state of an atom or ion. Both DR and RR start and end with the same atomic configuration, see figure 13. RR is a one-step non-resonant recombination of a free electron with an ion under the emission of a photon. DR is a two-step resonant recombination. It reaches the same final state for the recombined ion through an intermediate state. The first step is a resonant electron capture leading to a doubly-excited intermediate ionic state. The second step leads to the emission of a photon with nearly the same energy as in the RR process.

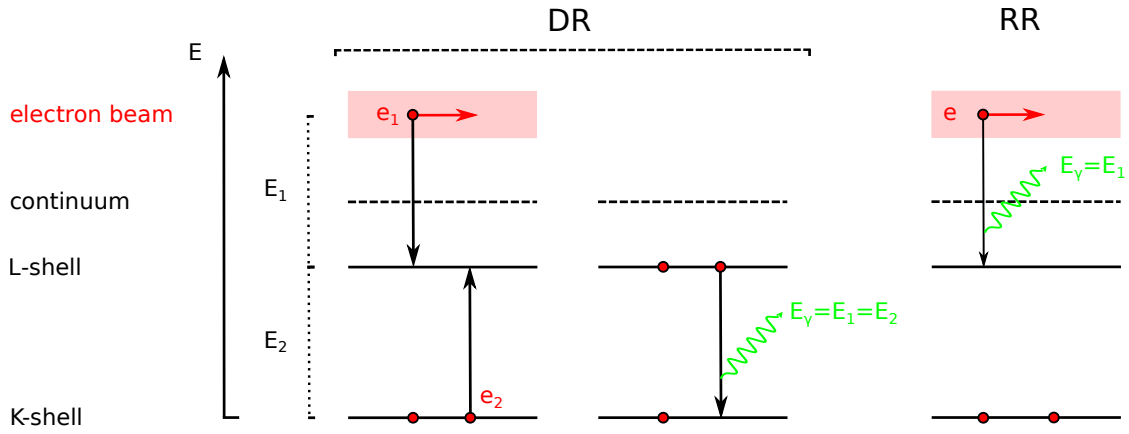


Figure 13: Comparison between DR and RR. Both processes start and end with the same atomic configuration. Photons produced by these two processes have nearly the same energy for a given energy of the recombining electron.

The polarisation of RR has been thoroughly examined for a wide spectral range, including the X-ray regime [59]. The polarisation of DR lacks thorough experimental observations. To quantify polarisation, the Stokes parameters are introduced, which allow a definition of the degree of linear polarisation of photons and their angle of polarisation. For a theoretical description of the polarisation of X-rays produced in atomic collisions, the density matrix formalism and so-called alignment parameters are used, which allow a quantification of the magnetic sublevel population of excited atomic states and the polarisation of their decay products. This leads to a discussion about the influence Breit interaction has on the alignment of the resonantly excited states in the DR process and thus on the polarisation of DR photons.

### 2.3.1 Radiative Recombination

Radiative recombination (RR) is the radiative capture of a free electron by an ion, see figure 14 . An electron from the continuum is captured into a bound state of an ion, emitting a photon with an energy equal to the initial kinetic energy of the electron $E_{kin}$ plus the binding energy of the state into which it is captured $E_{bind}$. RR can be viewed as the time-reverse of photoionisation, where an atom or ion is ionised by a photon, see figure 14.

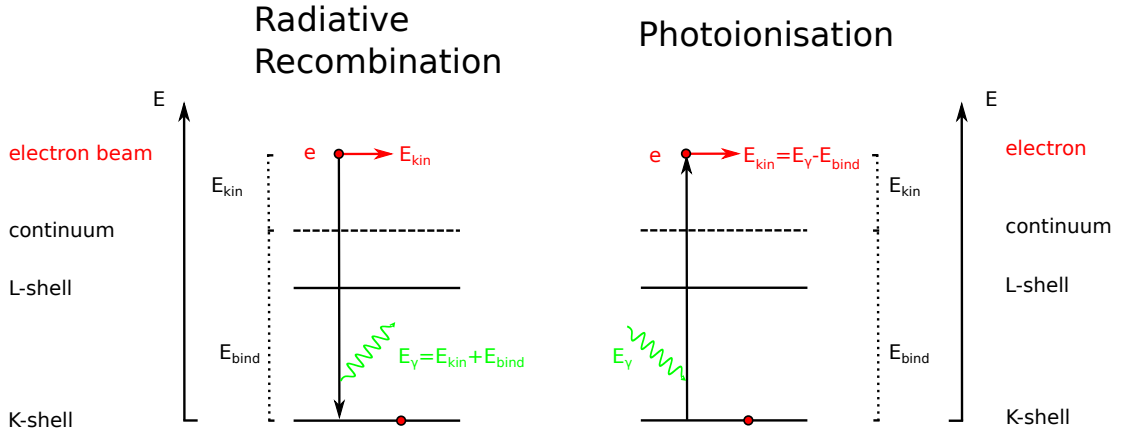


Figure 14: Comparison between radiative recombination and its time-reverse, photoionisation. In RR an electron is captured from the continum by an ion, under the emission of a photon.

The RR cross section $\sigma_{RR}$ is related to the photoionisation cross section $\sigma_{PI}$ by the principle of detailed balance assuming complete thermal equilibrium, i.e. through the Milne relation.

$$\sigma_{RR}(E_{kin})\, g_{q+1} = \sigma_{PI}(\omega) \frac{(\hbar\omega)^2}{2m_e c^2 E_{kin}}\, g_q \tag{32}$$

where, from the perspective of RR, $g_{q+1}$ and $g_q$ are the statistical weights of the recombined and the initial state and $\hbar\omega$ is the energy of the RR photon. For the recombination of an electron into level n of an ion with residual charge z, the RR cross section is estimated using the semiclassical Kramers equation, which is derived from the Bethe-Salpeter formula [36] [60]:

$$\sigma_{RR}(E_{kin}) = 2.10 \cdot 10^{-22} cm^2 \, \frac{G_n z^4 E_H^2}{n E_{kin}(z^2 E_H + n^2 E_{kin})} \tag{33}$$

with the Rydberg energy $E_H$. $G_n$ is the so called Gaunt factor which is introduced to account for deviations from the semiclassical result for the low-n states (n<10), e.g. $G_2 = 0.8762$ for the $L$ shell.

In collisions between electrons and ions, photons produced through RR and DR have nearly the same energy for a given electron energy, see figure 13. The energy difference is in the order of 10 eV - 100 eV, which is beyond the resolution of the detectors used in this thesis.

### 2.3.2 Dielectronic Recombination

Dielectronic recombination (DR) is a two-step resonant process involving two electrons and an ion. In the first step of this process, the dielectronic capture (DC), an electron is captured by an ion under simultaneous excitation of a bound electron. In the second step, the radiative stabilisation (RS), the intermediate excited state decays radiatively [23]. DR is a resonant process; the energy of the first electron $E_1$ has to match the energy required to excite the second electron $E_2$.

$$e^- + A^{q+} \xrightarrow{DC} A^{(q-1)+**} \xrightarrow{RS} A^{(q-1)+} + \hbar\omega \tag{34}$$

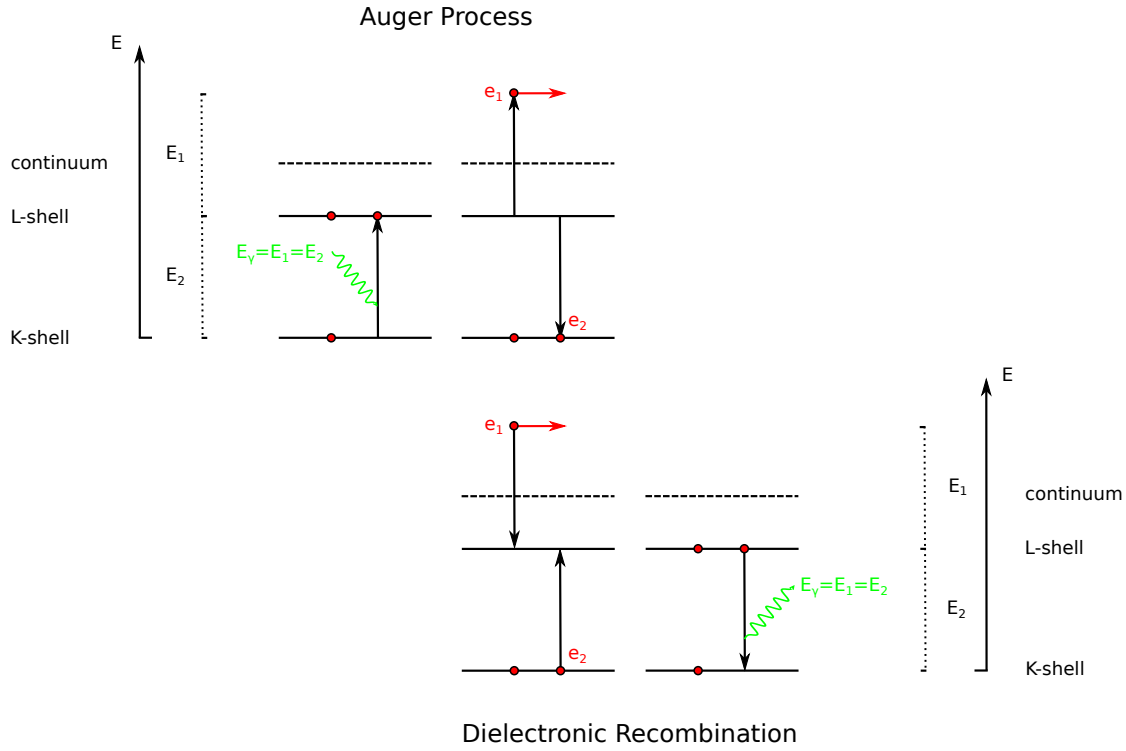


Figure 15: Comparison of the *KLL* Auger process (upper figure) to its time-reverse, *KLL* dielectronic recombination (lower figure).

DR can be seen as the time-reverse of the Auger process, which is autoionization, following photoexcitation of an inner-shell electron, see figure 15. Therefore an inverse Auger notation is used to distinguish different DR channels. *KLL* DR, for

example, denotes the capture of a free electron into the $L$ shell accompanied by the excitation of a bound $K$ shell electron into the $L$ shell. To distinguish different DR channels, the charge state of the ion before the recombination process and the level structure of the intermediate state is specified. The Xe $KLL$ DR resonance $\mathrm{Li}_1$, for example, refers to the resonance exciting the intermediate state $[1s2s^2 2p_{1/2}]_1$ in initially lithium-like xenon ions. There are a number of different final states this specific intermediate state can decay to. The energy differences of their emitted DR photons are in the order of 10 - 200 eV and therefore beyond the energy resolution of the X-ray detectors used in the experiments presented here.

The resonance strength for an isolated DR resonance from an initial state i through a doubly-excited state d to a final state f can be expressed as [61]

$$S_{idf} = \frac{g_d}{2g_i} \frac{\pi^2 \hbar^3}{m_e E_{res}} \frac{A_r(d \to f) A_a(d \to i)}{\sum A_r + \sum A_a} \tag{35}$$

Here $g_d$ and $g_i$ are the statistical weights of the intermediate and the initial state, respectively. $A_r$ is the radiative transition rate, $A_a$ is the autoionisation rate, and $E_{res}$ is the resonant energy. The factor 2 is due to the two possible spin states of the continuum electron. The summation is over all possible autoionisation and radiative decay channels from the intermediate state. Similar to the RR cross section, see equation (32), the dielectronic capture rate $A_d$ can be obtained from the autoionisation or Auger rate $A_a$ by the principle of detailed balance.

$$\begin{aligned} A_d &= \frac{g_d}{2g_i} A_a(d \to i) \\ &= \frac{2\pi}{2g_i} \sum_{m_d} \sum_{m_i m_s} \int sin\,\theta\, d\theta\, d\phi \mid \langle \Psi_d; J_d m_d || V || \Psi_i E_e; J_i m_i, \vec{p_e} m_s \rangle \mid^2 \end{aligned} \tag{36}$$

The integral is over the direction $(\theta, \phi)$ of the incoming continuum electron with the kinetic energy $E_e = p_e^2/2m_e$. The first summation is over the possible initial magnetic quantum numbers $m_i$ and the two possible spin states of the electron $m_s$. The second summation is over the possible magnetic quantum numbers of the intermediate state $m_d$. The interaction operator $V$ is the summation over the Coulomb $V_C = \sum_{i<j} \frac{1}{r_i - r_j}$, with $r_i$ being the position of the i$^{th}$ electron, and Breit interaction operators $V_B$, discussed in chapter 2.1.3

### 2.3.3 Polarisation of Dielectronic Recombination Lines: Density Matrix Formalism

The density matrix formalism is used to derive the polarisation properties of the stabilising radiation in dielectronic recombination. This formalism allows a description of mixed quantum states. It allows quantum mechanic calculations with statistical ensembles, described by the density operator, i.e. it allows to account for ensembles in which a probability distribution describes the state of the system. The density matrix formalism was introduced by J. von Neumann in 1927 [62]. In 1989 it was applied by M. Inal et al. [26] to calculate the polarisation of DR lines. Here in this chapter, we follow the textbook of V. Balashov [63].

In the case of DR, the method is used to describe the population of different magnetic sublevels in the excitation of autoionising states in electron-ion collision. A non-statistic population of the magnetic sublevels of a state is called alignment. The decay radiation of aligned states is polarised. The density matrix formalism allows us to define an initial state of the collision system and to follow this system through the collision process, hereby keeping all quantum information [64]. In the collision process, the magnetic sublevels of the intermediate state are populated. The probability distribution for the population of these magnetic sublevels is described by matrix elements of the density operator. By making use of a proper set of operators, we then deduce the polarisation properties of the stabilising radiation.

#### Polarisation of Photons: Stokes Parameters

The Stokes parameters are a practical notation to represent the polarisation of photons. The polarisation of photons is defined as the orientation of the electric field, i.e. for linearly polarised light the plane in which the electric field vector $\vec{E}_{\vec{x},t}$ is oscillating and the degree to which the light is linearly polarised. For electromagnetic waves propagating in the $\vec{z}$-direction with $E_{x(t)} = E_{x0}\, cos(\omega t)$ and $E_{y(t)} = E_{y0}\, cos(\omega t + \delta)$, the Stokes parameters $P_n$ are defined in the following way [65]:

$$P_i = \frac{s_i}{s_0}, \;\; i = 1, 2, 3 \quad \text{with} \tag{37}$$

$$s_0 = \frac{1}{2}(E_{x0}^2 + E_{y0}^2), \qquad s_1 = \frac{1}{2}(E_{x0}^2 - E_{y0}^2), \tag{38}$$

$$s_2 = E_{x0}\, E_{y0}\, cos(\delta), \qquad s_3 = E_{x0}\, E_{y0}\, sin(\delta) \tag{39}$$

$s_0$ represents the total photon intensity, $s_1$ the difference in intensities transmitted through a linear polariser with its transmission direction parallel to the x-axis and

y-axis, respectively, $s_2$ the difference in intensities transmitted through a linear polariser with its transmission direction set at angles 45° and -45°, with respect to the x-axis, and $s_2$ and $s_3$ the difference in intensities transmitted through a circular polariser with its transmission set for right-hand-circular and left-hand-circular polarisation, respectively. The degree P and the angle $\chi$ of photon linear polarisation are related to $P_1$ and $P_2$ as

$$P = \sqrt{P_1^2 + P_2^2}, \quad cos(2\chi) = \frac{P_1}{P}, \quad sin(2\chi) = \frac{P_2}{P} \tag{40}$$

**The Density Matrix Formalism**

In the density matrix theory, the state of a physical system is characterised by means of statistical operators which describe the system in either a pure quantum state or as an ensemble of mixed states with any degree of coherence [64]. The density operator is a generalisation of a state vector, which describes mixed states. A mixed state is a system of orthogonal states $|\psi_i\rangle$ with the probability $p_j$ of finding the system in the particular pure state $|\psi_j\rangle$, with $\sum_i p_i = 1$ [66]. The density operator

$$\hat{\rho} = \sum_i p_i \, |\psi_i\rangle \, \langle\psi_i| \tag{41}$$

with the projection operator $R = |\psi_i\rangle \langle\psi_i|$, acting on the state vector $|\phi\rangle$, projects the component of $|\phi\rangle$ parallel to each $|\psi_i\rangle$ and weights it by $p_i$. The mixed states are described by matrix elements of the density operator, e.g. in the representation $|\xi\rangle$ [63].

$$\rho_{mn} = \langle\xi_m| \, \rho \, |\xi_n\rangle = \sum_i p_i \, \langle\xi_m|\psi_i\rangle \, \langle\psi_i|\xi_n\rangle \tag{42}$$

The spin-density matrix is a particular case of a density matrix, which describes a mixed system in the representation of angular momenta: spin, orbital, and/or total angular momentum [63]. For a system of particles with spin s and orbital angular momentum l, for uncoupled l and s, the density matrix is: $\langle lm_l sm_s|\rho|lm_{l'} sm_{s'}\rangle$. For a system of sharp total angular momentum j, the density matrix is: $\langle jm|\rho|jm'\rangle$.

A further method to describe mixed systems in the representation of angular momenta are statistical tensors [63].

$$\rho_{kq(j,j')} = \sum_{mm'} (-1)^{j'-m'} (jm, j'-m'|kq) \, \langle jm|\rho|j'm'\rangle \tag{43}$$

where $(jm, j'-m'|kq)$ are Clebsch-Gordan coefficients. According to the properties of the Clebsch-Gordan coefficients, there are altogether $\sum_k(2k+1) = (2j+1)(2j'+1)$ statistical tensors $\rho_{kq(j,j')}$, which coincides with the number of different combinations of m, m'. Normalising the statistical tensors to $\rho_{00(j,j')}$ with $\sum_j(2j+1)^{1/2}\rho_{00(j,j')} = 1$ yields the reduced statistical tensors:

$$\mathcal{A}_{kq\,(j,j')} = \frac{\rho_{kq\,(j,j')}}{\rho_{00\,(j,j')}} \tag{44}$$

In our case, a plasma in an EBIT, as will be explained later on, the system under consideration is symmetric with respect to a particular quantisation axis, defined by the electron beam direction. The magnetic sublevel population is the same for $\pm m_j$. The density matrix $\langle jm|\rho|jm'\rangle$ is diagonal with respect to the projections $m = m'$ and the components of the statistical tensor with non-zero $q$ vanish [63].

### Polarisation of Dielectronic Recombination Lines

The polarisation of the RS in the DR process depends on the population of the magnetic sublevels $|J_d, m_d\rangle$ of the intermediate state $|\alpha_d J_d\rangle$, where $J_d$ is the total angular momentum of the intermediate state and $\alpha_d$ represents the other quantum numbers needed to characterise this state. The reduced matrix element for the resonant electron capture $\langle\alpha_d J_d||V||\alpha_0 J_0, lj : J_d\rangle$ is the central building block from which most DR properties can be calculated. Using the density-matrix theory, the initial state of the collision system is given by $|\alpha_0 J_0, lj\rangle$: an ion in the state defined by its total angular momentum $J_0$ and other quantum numbers represented by $\alpha_0$, and a free (unpolarised) electron with orbital and total angular momentum, $l$ and $j$, respectively. This system goes through the interaction, represented by the operator $V$ mediating the interaction, i.e. the resonant capture of the electron, to the intermediate state $|\alpha_d J_d\rangle$.

For the RS to be polarised, the magnetic sublevels of the intermediate state have to be aligned, i.e. populated non-statistically. The X-rays produced by the decay of individual magnetic sublevels are polarized differently. Figure 16 illustrates this for an electric-dipole (E1) allowed transition between a state with angular momentum J = 1 and J = 0. For $\Delta m = 0$, π-light is emitted, while for $\Delta m = \pm 1$, $\sigma^{\mp}$-light is emitted. Figure 17 illustrates the polarisation of the photons associated with these transitions. π-light is associated with the z component of the transition dipole matrix element [46]. The electron charge cloud oscillates along the z-axis. π-light is emitted predominantly perpendicular to the z-axis. It is linearly polarised along the z-axis. σ-light is associated with complex linear combinations of the x and y

components of the transition dipole matrix element [46]. The electron charge cloud rotates around the z-axis. σ-light is emitted predominantly along the z-axis, with a smaller component perpendicular to the z-axis. The component along the z-axis is circularly polarised, while the component perpendicular to the z-axis is linearly polarised perpendicular to the z-axis.

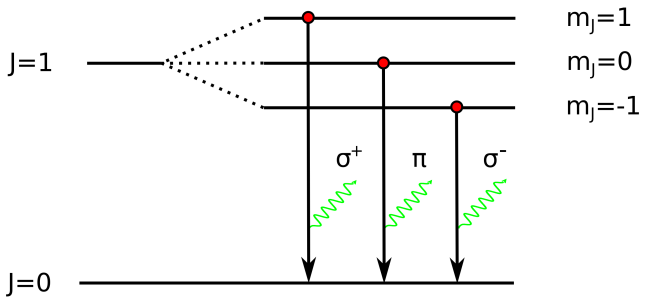


Figure 16: Different E1 transitions from a $J = 1$ state to a $J = 0$ state with $\Delta m = 0, \pm 1$ for Zeeman-splitting of magnetic sublevels of the $J = 1$ state in the strong magnetic field of the nucleus.

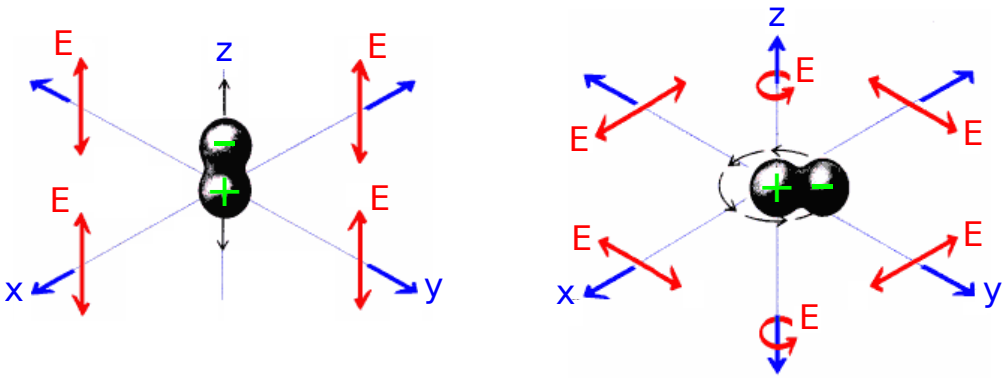


Figure 17: Polarisation of X-rays emitted in transitions with $\Delta m = 0$, π-light, (left side) and $\Delta m = \pm 1$, σ-light, (right side) for different directions with respect to the quantisation axis, the z-axis. Modified from [67]

In our case, the unidirectional electron beam breaks the isotropy of the ionic system. The system becomes aligned to the electron beam direction. Figure 18 illustrates the quantisation of the total angular momentum for an intermediate state with $J_d = 3/2$ along the electron beam direction. For this symmetric system, i.e. the aligned ion, magnetic sublevels with the same modulus of the magnetic quantum number are populated equally: $\sigma_{m_J} = \sigma_{-m_J}$. For the population of these magnetic sublevels with different modulus of the magnetic quantum number and hence the

alignment of the state, selection rules apply which are given by the Clebsch-Gordan coefficients.

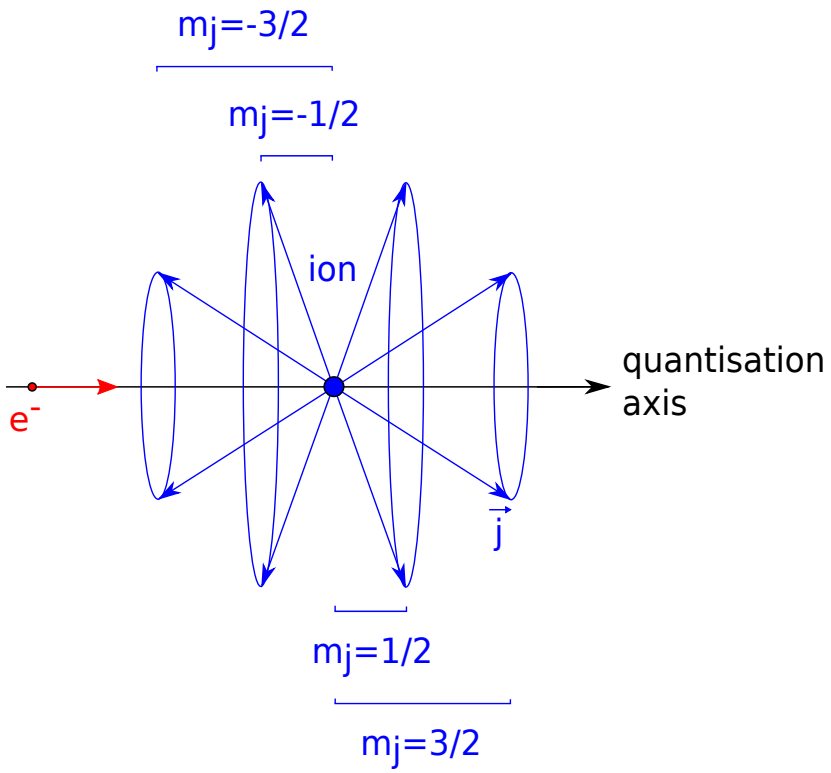


Figure 18: Illustration of the symmetry breaking of a ionic system with total angular momentum $J = 3/2$ by an electron beam. The angular momentum becomes quantised along the electron beam direction.

In the density matrix formalism, the magnetic sublevel population of the intermediate state is described most naturally in terms of alignment parameters $\mathcal{A}_{k0\,(\alpha_d J_d)}$, see equation (44). For the resonant capture of an (unpolarised) electron by an ion, these parameters can be expressed in the form [19]:

$$\mathcal{A}_{k0\,(\alpha_d J_d)} = \frac{N}{8\pi[J_0]} \sum_{ll'jj'} (-1)^{J_d+J_0-1/2} [l,l',j,j']^{1/2} \langle \alpha_d J_d || V || \alpha_0 J_0, lj : J_d \rangle$$
$$\langle \alpha_d J_d || V || \alpha_0 J_0, l'j' : J_d \rangle^* \langle l0l'0|k0\rangle \begin{Bmatrix} j & l & 1/2 \\ l' & j' & k \end{Bmatrix} \begin{Bmatrix} j & J_d & J_0 \\ J_d & j' & k \end{Bmatrix} \tag{45}$$

where N denotes a normalisation constant, $\langle l0l'0|k0\rangle$ a Clebsch-Gordan coefficient, $[a,b,...] \equiv (2a+1)(2b+1)...$ and where the standard notation for the Wigner 6-j symbols has been utilized. The summations $\sum_{ll'jj'}$ are over the partial electron waves for initial and final continuum electron momentum quantum numbers for the

capture into the doubly-excited intermediate state. The interaction operator $V$ is $V = V_C + V_B$, i.e. for the Coulomb and Breit, see equation (23), interaction.

The alignment parameters can also be written in terms of the partial electronic capture cross sections into magnetic substates $\sigma_{m_d}$ of the state with total angular momentum $J_d$:

$$\mathcal{A}_{k0(J_d)} = (-1)^{J_d+m_d} \sum_{m_d} \sqrt{(2J_d+1)(2k+1)} \begin{Bmatrix} J_d & J_d & k \\ -m_d & m_d & 0 \end{Bmatrix} \frac{\sigma_{m_d}}{\sum_{m'_d} \sigma_{m'_d}} \tag{46}$$

The rank k of the alignment parameter is the multipole order of the emitted radiation: $k = 2^L$ with L=1 for the electric dipole E1 and the magnetic dipole M1 transitions, and L=2 for the electric quadrupole E2 and the magnetic quadrupole M2 transitions, and so on. Here we will only take the dominant electric dipole term with L=1 and k=2 into account. This approximation seems valid for the mid-Z ions under consideration here and furthermore for our experimental precision in measuring the degree of linear polarisation of the stabilising radiation.

The specific collision system under consideration here, a unidirectional electron beam recombining into ions, is symmetric with respect to the the electron beam direction which introduces a quantisation axis, see figure 18. For such an aligned ion, $q = 0$, the tensor $\mathcal{A}_{20\,(\alpha_d J_d)}$ is nonzero only if $k \leq 2J_d$. Otherwise the Clebsch-Gordan coefficient vanishes. This restriction implies, in particular, that only excited states with $J_d > 1/2$ can be aligned.

In the experiments presented here, the DR resonances of interest have intermediate states with $J_d = 1/2, 1, 3/2$ and $5/2$. The alignment parameters in terms of partial electronic capture cross sections into magnetic substates are:

$$\mathcal{A}_{20(J_d=1/2)} = 0 \tag{47}$$

$$\mathcal{A}_{20(J_d=1)} = \frac{\sqrt{2}(\sigma_1 - \sigma_0)}{\sigma_0 + 2\sigma_1} \tag{48}$$

$$\mathcal{A}_{20(J_d=3/2)} = \frac{\sigma_{3/2} - \sigma_{1/2}}{\sigma_{3/2} + \sigma_{1/2}} \tag{49}$$

$$\mathcal{A}_{20(J_d=5/2)} = -\frac{4\sigma_{1/2} + \sigma_{3/2} - 5\sigma_{5/2}}{\sqrt{14}(\sigma_{1/2} + \sigma_{3/2} + \sigma_{5/2})} \tag{50}$$

The defined alignment of the intermediate state $\mathcal{A}_{20(J_d)}$ is now used to calculate

the polarisation of the stabilising radiation for the transition $\alpha_d J_d \longrightarrow \alpha_f J_f$. For the specific geometrical setup of the experiments presented in this thesis, the polarisation is measured in the direction perpendicular to the axis of alignment, the degree of linear polarisation of the RS becomes [63]:

$$P = \frac{3\alpha_2^\gamma \mathcal{A}_{20(\alpha_d J_d)}}{\alpha_2^\gamma \mathcal{A}_{20(\alpha_d J_d)} - 2} \tag{51}$$

with the intrinsic anisotropy parameter for photoemission:

$$\alpha_2^\gamma = \frac{3}{2}\sqrt{J_d(J_d+1)}(-1)^{J_d+J_f+3} \begin{Bmatrix} J_d & J_d & 2 \\ 1 & 1 & J_f \end{Bmatrix} \tag{52}$$

which take the following values for different combinations of $J_d$ and $J_f$:

| $J_d$ | $J_f$ | $\alpha_2^\gamma$ | $J_d$ | $J_f$ | $\alpha_2^\gamma$ |
|---|---|---|---|---|---|
| 0 | 1 | 0 | 1/2 | 1/2 | 0 |
| 1 | 0 | $1/\sqrt{2}$ | 1/2 | 3/2 | 0 |
| 1 | 1 | $-1/2\sqrt{2}$ | 3/2 | 1/2 | 1/2 |
| 1 | 2 | $1/10\sqrt{2}$ | 3/2 | 3/2 | $-2/5$ |
| 2 | 1 | $\sqrt{7}/2\sqrt{10}$ | 3/2 | 5/2 | 1/10 |
| 2 | 2 | $-\sqrt{7}/2\sqrt{10}$ | 5/2 | 3/2 | $\sqrt{7}/5\sqrt{2}$ |
| 2 | 3 | $1/\sqrt{70}$ | 5/2 | 5/2 | $-4\sqrt{2}/5\sqrt{7}$ |
| 3 | 2 | $\sqrt{3}/5$ | 5/2 | 7/2 | $1/2\sqrt{14}$ |

Table 1: Anisotropy parameters $\alpha_2^\gamma$ characterising the polarisation of emitted photons. Modified from [63].

In DR a specific intermediate state $|\alpha_d J_d\rangle$ usually decays into different final states $|\alpha_f J_f\rangle$, which cannot be resolved with the polarimeters used here. For each of these transitions, the degree of linear polarisation $P_L$ and the radiative rate $A_r^{df}$ are calculated. Flexible Atomic Code [36] calculations were performed to derive these values. To derive the cumulative polarisation of the transition from a specific intermediate state to the unresolvable final states, the polarisation of each of the contributing transition is weighted with its radiative rate and averaged.

$$P = \frac{\sum_f P_{L,f} A_r^{df}}{\sum_f A_r^{df}} \tag{53}$$

As an example, the calculation of the degree of linear polarisation of the *KLL* DR resonance into Li-like xenon designated $\mathrm{Li}_1$ with the initial state $[1s^2 2s_{1/2}]_1$ and the intermediate state $[1s2s^2 2p_{1/2}]_1$ is sketched here. With the calculated rates and

| Final State | Polarisation $P_L$ | Radiative Rate $A_r^{df}$ $[s^{-1}]$ | Photon Energy [keV] |
|---|---|---|---|
| $[1s^2 2s^2]_0$ | -0.442 | $2.9{\cdot}10^{15}$ | 30.04 |
| $[1s^2 2s_{1/2} 2p_{1/2}]_0$ | 0.0 | $1.8{\cdot}10^{11}$ | 29.94 |
| $[1s^2 2s_{1/2} 2p_{1/2}]_1$ | 0.0 | $3.5{\cdot}10^{11}$ | 29.92 |
| $[1s^2 2p_{1/2}^2]_0$ | -0.442 | $6.3{\cdot}10^{13}$ | 29.74 |
| $[1s^2 2p_{1/2} 2p_{3/2}]_1$ | 0.181 | $3.9{\cdot}10^{12}$ | 29.41 |
| $[1s^2 2p_{1/2} 2p_{3/2}]_2$ | -0.039 | $1.5{\cdot}10^{13}$ | 29.39 |

Table 2: Degree of linear polarisation, radiative rate and photon energy for decays from the intermediate state $[1s2s^2 2p_{1/2}]_1$ into different possible final states in the RS transition of the *KLL* DR resonance $\mathrm{Li}_1$ in highly charged xenon ions. Each configuration in this table is in *j-j* coupling notation.

polarisations of the specific transitions, see table 2, this yields a cumulative degree of linear polarisation of: $\mathrm{P}_{\mathrm{Li}_1}$ = -0.441

Breit interaction only affects the polarisation of decays from specific intermediate states. For these, BI affects their alignment. The summation in equation (45) runs over all partial electron waves, $|lj\rangle$, contributing in the interaction. If only one partial wave contributes, the polarisation of the RS does not depend on BI. This can be explained by the fact that since the electron-electron interaction operator is scalar, it cannot affect the magnetic sublevel population of excited ions if only a single partial wave contributes in the resonant capture transition [22]. If only one partial wave contributes, the alignment of the intermediate state is given solely by Clebsch-Gordan coefficients. In the following experiments, the polarisation of the stabilising X-rays for different DR resonances has been measured. Calculations taking only Coulomb interaction and calculations which also take Breit interaction into account have been performed and compared to the measurements. This allows a systematic study of the influence of Breit interaction on the electron-electron interaction.

# 3 Experimental Setup

Two polarisation measurements have been carried out at heavy ion facilities at the Max Planck Institut für Kernphysik in Heidelberg: the FLASH- and HD-EBIT - electron beam ion trap - facilities. The setups used at these two facilities both consist of the same constituents: an EBIT, a Compton polarimeter based on silicon PIN (SiPIN) diodes and another detector, a germanium detector, see figure 19. Highly charged ions are produced and trapped in the EBIT using a monoenergetic and unidirectional electron beam. The polarisation of X-rays emitted in collisions of electrons and ions are measured with the Compton polarimeter, where the X-rays from the ion trap are scattered and then detected by SiPIN diodes. Unscattered X-rays are detected by a germanium detector for diagnostic purposes. This chapter focusses on the functioning principle of each of these elements of the setup, while the following two chapters, chapter 4 and 5, deal with the actual experiments.

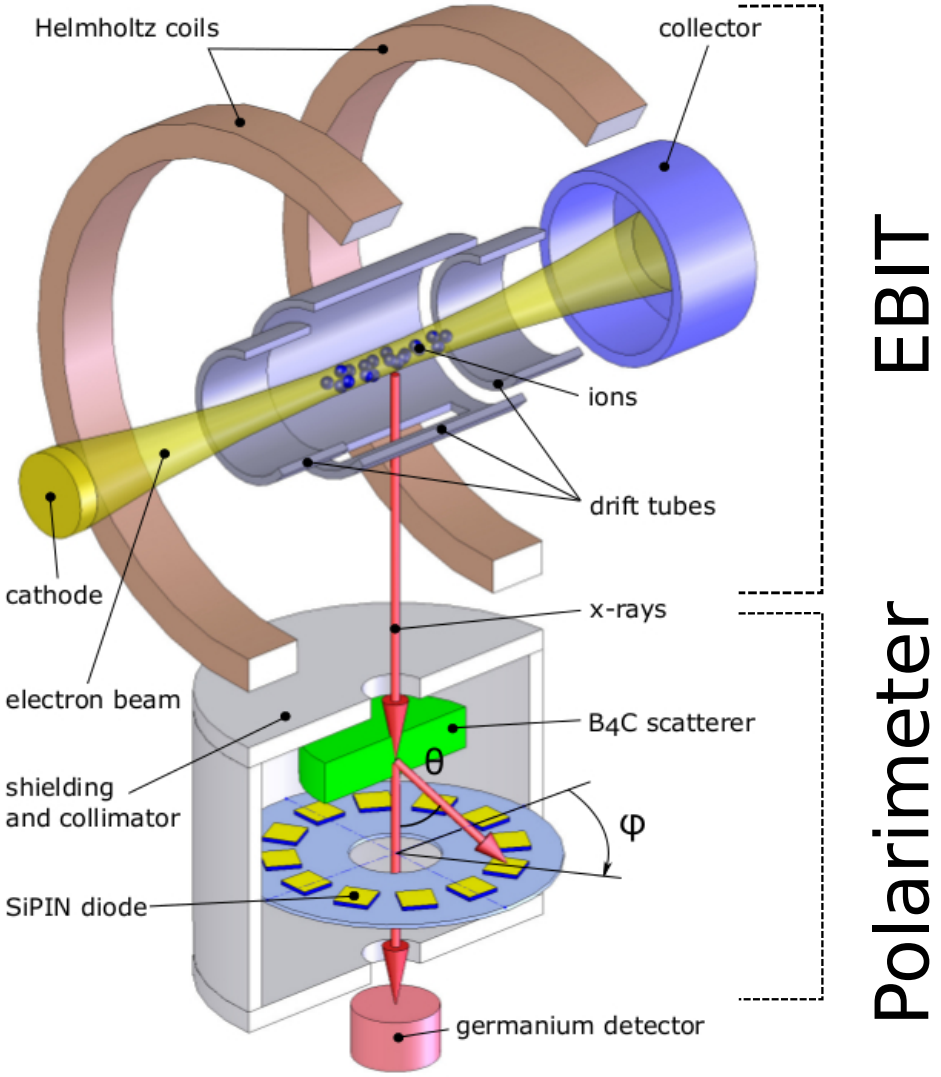


Figure 19: Setup used for the measurements at heavy ion facilities at the Max Planck Institut für Kernphysik in Heidelberg. Highly charged ions are produced and trapped in an electron beam ion trap (EBIT). The polarisation of X-rays emitted in collisions of electrons and ions are measured with a Compton polarimeter. A germanium detector records unscattered X-rays from the trap.

## 3.1 Principle of an Electron Beam Ion Trap

The basic principle of an EBIT is to produce and trap highly charged ions in a cylindrical volume with the dimensions of a human hair of a few centimetres length, using a unidirectional and monoenergetic electron beam. In contrast to other devices which are capable of producing high charge states of ions, such as e.g. heavy-ion Experimental Storage Rings, ESR, an EBIT is a table-top device with the size of a regular room. ESRs store ion beams with an unprecedented quality, i.e. cooled and intense beams at high-$Z$ and with precisely known energies and charge states at small momentum spread. They are used in spectroscopy experiments of X-ray transitions in the heaviest one- and few-electron ions. In EBITs, ions are produced at rest. Here experiments focus on QED and atomic structure studies [1]. A further source of HCIs are Electron Cyclotron Resonance Ion Sources (ECRIS), in which a plasma is magnetically confined by a combination of solenoids and a multipole configuration of permanent magnets. The plasma is produced by microwaves, which are guided into the plasma chamber. For ECRIS, the charge state distribution is broad and the production of highest charge states is not possible.

The history of EBITs starts with the development of the EBIS - Electron Beam Ion Source - in Dubna, Russia, 1965 by Donet et al. and their production of bare nitrogen and highly charged gold ions [68]. Improvements were made on the design to provide better plasma stability and the possibility to do spectroscopy on the trapped ions, which culminated in the development of the EBIT by Levin and Marrs at Livermore, USA, in 1988 [69]. To achieve the production of higher charge states of the heaviest ion species, so called "Super"-EBITs nowadays generate electron beam energies of up to 200 keV. The original Super EBIT at Livermore has even produced bare uranium ($U^{92+}$) in 1994 [70]. The EBIT design has been successfully used at many heavy ion facilities around the world, as well as at the MPIK in Heidelberg, where there are currently a wide assortment of EBITs in operation. We conducted our experiments at two of these, the FLASH-EBIT and the HD-EBIT. The FLASH-EBIT is designed to be used at radiation facilities around the world. It derives its name from an experiment at the Free-electron LASer at Hamburg, Germany [71]. The HD-EBIT is a Super EBIT designed for electron beam energies of up to 350 keV.

Most EBITs are of similar design. The main constituent of every EBIT is the electron beam. It is emitted from a cathode in the electron gun. The beam is accelerated towards the trapping region. On its way it is compressed by a strong magnetic field to a diameter of a few tens of µm. It is then deaccelerated, decompressed and dumped on the collector. The electron beam is at the same time

responsible for ionising and trapping the ions. This short introduction to the working principles of EBITs follows the path of the electron beam.

### Electron Gun

The design of the electron gun is optimized to produce a unidirectional electron beam with a very high beam compression, i.e. a small beam diameter. Therefore it consists of an arrangement of electrodes - the cathode, anode and focus electrode - and magnetostatic components - the bucking and trimming coils, see figure 20. The cathode is made of tungsten infused with barium oxide. It is heated up to temperatures beyond 1000°C. The cathode is put on a negative potential relative to the anode. Electrons leaving the cathode due to thermionic emission are accelerated towards the anode. A design based on the work by Pierce [72] has been used for the geometry of the cathode, its holder and the focus electrode. The cylindrically shaped focus electrode enclosing the cathode helps pulling electrons away from the cathode and guiding them towards the anode. By adjusting the potential of the focus electrode, the electron beam current can be manipulated.

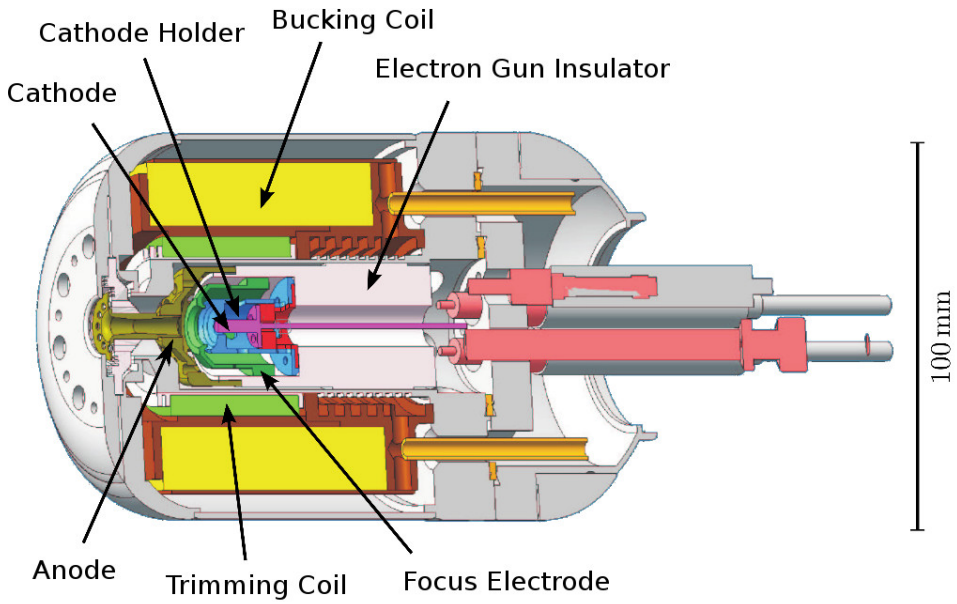


Figure 20: Axial schematic view of the electron gun of the FLASH-EBIT. Adapted from [73]

The main parameter characterising the electron beam responsible for a high ionisation rate in the trap is the electron beam current density $j_e$, which is given by

$$j_e = \frac{I_e}{\pi r_H^2} \tag{54}$$

with the electron beam current $I_e$ and the electron beam radius $r_H^2$. Beam compression is managed through a non-uniform radially symmetric magnetic field of several T produced by a pair of superconducting Helmholtz coils. Unfortunately a high residual magnetic field in the electron gun is counterproductive for a high beam compression, according the the theory of electron beam dynamics by Herrmann [74]. The electron beam has the smallest diameter when the residual magnetic field at the cathode is zero; this is managed through the bucking coil. Furthermore, the beam radius decreases with decreasing beam current. The beam radius is also responsible for the energy resolution of the beam. Because of the build up of space charge due to the electron beam, electrons with a higher radial distance from the beam center experience a slightly different - a few V up to 100 V - potential than electrons at the beam center. Through fine tuning of the magnetic and electric fields in the gun, a compromise between these parameters - beam current density and energy resolution - has to be found for the operation of each EBIT and for the specific goals of each experiment.

### Ion Trap

The trapping of the positively charged HCIs is achieved by an interplay between the negative stationary electric field produced by the electron beam, trapping the HCIs radially, and an arrangement of drift tubes, trapping the HCIs longitudinally, see figure 21. As already mentioned, beam compression is achieved by magnetic lensing by a strong magnetic field of a few T which is produced by a superconducting Helmholtz coil pair. Due to angular momentum conservation electrons from the gun follow the magnetic field lines. The Helmholtz coils are cooled by liquid helium or by a cryocooler.

Through the negative space charge of the electron beam, a cylindrically shaped cloud of HCIs forms around the electron beam. For a given beam energy, the charge state balance within the cloud emerges in an equilibrium condition between several rivalling processes: electron impact ionisation, radiative and dielectronic recombination, as well as charge exchange in collisions between the HCIs and the residual gas in the trap region. The ion abundance ratio for the adjacent charge states $q$ and $q-1$ of an HCI can be expressed in terms of cross sections for the relevant collision processes [32]

$$\frac{n_{q-1}}{n_q} = \frac{\sigma_q^{DR} + \sigma_q^{RR} + \langle \sigma_q^{CX} \rangle}{\sigma_{q-1}^{ion}} \tag{55}$$

where $\sigma_q^{DR}$ and $\sigma_q^{RR}$ are the dielectronic and radiative recombination cross sections

for the ion charge state $q$, $\sigma_{q-1}^{ion}$ the electron impact ionisation cross section for the ion with $q-1$, and $\langle \sigma_q^{CX} \rangle$ the effective charge exchange cross section for collisions with the residual gas.

For the longitudinal trapping of the HCIs, drift tube electrodes are biased to set a specific trap depth, which prevents the HCIs from escaping the trap along the electron beam. Biasing the drift electrode also offers a tool to access and set the ion temperature and the number of ions in the trap. Deeper traps lead to a higher number of ions stored and higher ion temperature. Over time heavier elements, e.g. impurity elements like tungsten from the cathode, are also trapped and further heat up the trap. Therefore the trap is dumped in a certain cycle, which is done by raising the potential of the central trap for a few seconds. Furthermore, the whole trap platform is electrically biased on a given positive potential to accelerate the electron beam towards trapping region. The central drift tube has windows drilled into it, which enable spectroscopic access to the trap.

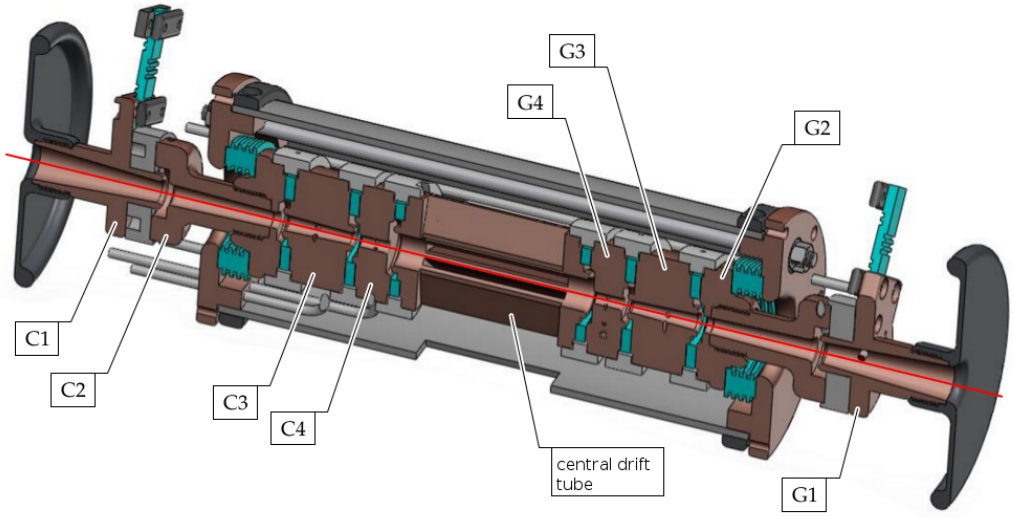


Figure 21: A schematic view of the drift tube assembly of the FLASH-EBIT. The drift electrodes on the side of the gun (G1-G4) and on the side of the collector (C1-C4) as well as the central drift tube can all be put on their own potential. Adapted from [75]

### Collector

The electron beam is dumped in the collector after passing through the trapping region. The collector is on the same potential as the electron gun to deaccelerate the electron beam. The collector magnetic coil suppresses the magnetic field from the Helmholtz coils which leads to a beam widening. The beam impinges on the inner

walls of the collector. Its associated heat is transported away by water cooling. At the backside of the collector there is an extractor electrode which is put on a negative potential with respect to the cathode to ensure that no electrons leave the collector.

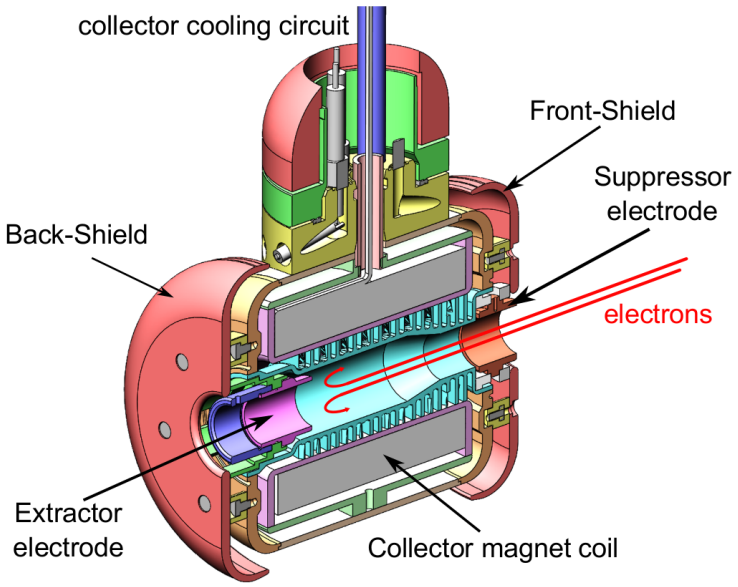


Figure 22: A schematic representation of the electron collector. Adapted from [73].

### Injection System

The gas injection system enables a collimated gas beam with well regulated flux being injected into the trap. It consists of a needle valve and different pumping stages. While the needle valve is used to regulate the gas flux, the differential pumping enables the gas to be injected without significantly raising the pressure in the trap. The pressure in the gas system is in the order of $10^{-7}$ mbar, while the overall pressure in the EBIT is better than $10^{-10}$ mbar.

## 3.1.1 FLASH-EBIT

The FLASH-EBIT was used in our first polarimeter experiment with HCIs. It is capable of running with acceleration voltages of up to 80 kV and providing beam currents of up to 550 mA. The FLASH-EBIT is constructed in a way that makes it easy to transport and exploit radiation facilities around the world. It is pumped to vacuum levels of down to $10^{-11}$ mbar and cryostatic cooling puts the trapping region and the superconducting Helmholtz coils down to temperatures of 4 K. The FLASH-EBIT was the first cryostatically cooled EBIT, not relying on tanks filled

with helium for its cooling, but on a closed cycle refrigerator, which significantly lowers operation cost. The magnets provide a magnetic field of 6 T, which leads to a beam compression of $\sim 50\ \mu m$. Its trap region is radially symmetric, consisting of a central electrode with radial windows for spectroscopy and four electrodes on each side of the central one, see figure 23. The electron gun has a cathode with a spherically concave shape with a diameter of 3 mm and a concave radius of 5 mm. It is made of tungsten impregnated with barium and can be brought up to a temperature of 1100°C.

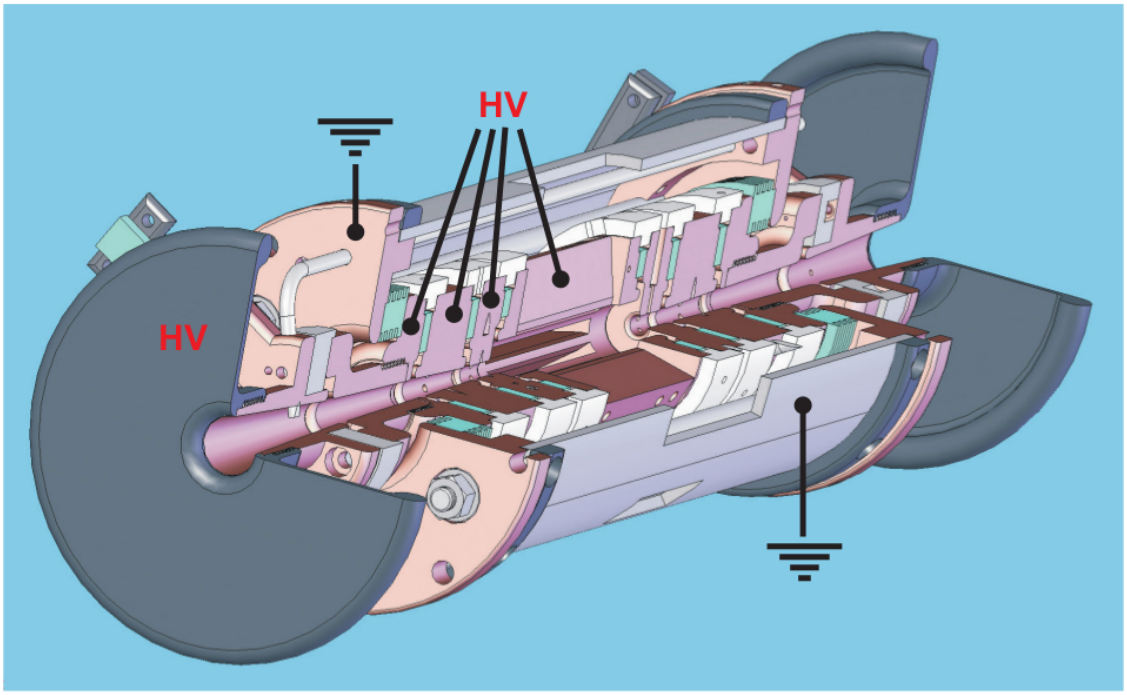


Figure 23: Schematic representation of the axialsymmetrical trap construction of the FLASH-EBIT. The nine trap electrodes are put on high voltage. The housing is grounded. Adapted from [76]

### 3.1.2 Heidelberg EBIT

The HeiDelberg EBIT (HD-EBIT) has a design which allows energies up to 350 keV, with currents up to 750 mA, and at the same time easy access for spectroscopy experiments. It is arranged vertically with four elongated apertures in the central drift tube, allowing optical access to the trapped ions. One of these, offers a 250 µm beryllium window for X-ray spectroscopy. The electron gun in the HD-EBIT has a similar design as in the FLASH-EBIT. The cooling system of the superconducting magnet, two Helmholtz coils, comprises three thermal shields, at 50 K and 20 K, with the magnet residing in a liquid helium tank at 4 K. It generates a 8 T magnetic

field at a current of 76.24 A, which compresses the electron beam to a diameter of 50 μm. The cooling system of the HD-EBIT has to be refilled with liquid helium in intervals of seven days, which requires a complete shutdown of the EBIT. The trap as such consists of nine cylindrically shaped drift tube electrodes made of copper. The radius of the innermost tube is 5 mm. All of them can be biased independently to form a specific trap. The HD-EBIT was constructed in Freiburg, Germany, in 1998, was transported to Heidelberg two years later and since then has produced a broad variety of ion charge states: $Hg^{78+}$, $W^{74+}$, $Xe^{54+}$, $Kr^{36+}$, $Ge^{30+}$.

## 3.2 SiPIN Diode Compton Polarimeter

The SiPIN based Compton polarimeter design, see figure 24, is based on the sensitivity of the angular distribution of Compton scattered X-rays to their degree of linear polarisation, which is given by the Klein-Nishina formula, see equation (28). Incoming X-rays are collimated and then scattered in a 10 mm thick scatterer. The scattered X-rays are detected in an array of twelve SiPIN diodes. Their azimuthal angular scattering distribution, which relates to their degree of linear polarisation through the Klein-Nishina formula, see equation (28), is sampled by the SiPIN chips at a polar scattering angle of $\theta = 50°$.

Compton polarimetry is well established in the X-ray energy region from 80 keV up to several MeV. The Compton polarimeter presented here functions in region from 10 keV to 35 keV, where most X-ray transitions of mid- and high-Z ions are. Here, there are several sources of difficulties, which are high photoabsorption cross sections in the scattering material, see chapter 2.2, low energy deposition in the scatterer and a high background of naturally occurring X-rays. The low energy deposition in the scatterer, which is due to a low energy transfer to the electron in Compton scattering of X-rays with energies below 35 keV, see figure 11, makes the use of active scatterers, e.g. germanium crystals, impossible. At higher X-ray energies, the use of active scatterers makes a coincidence measurement between the electrons and scattered X-rays possible, which significantly reduces background levels. To still make Compton polarimetry possible in the X-ray energy region from 10 keV to 35 keV, low-$Z$ materials with relatively small photoabsorption cross sections, here beryllium and boron carbide ($B_4C$), are employed as passive scatterers. Furthermore, as detector chips, 380 μm thin SiPIN diodes are used as detector chips, which offer a small volume to the absorption of naturally occurring X-rays. The manufacturing of such thin chips has only recently become possible.

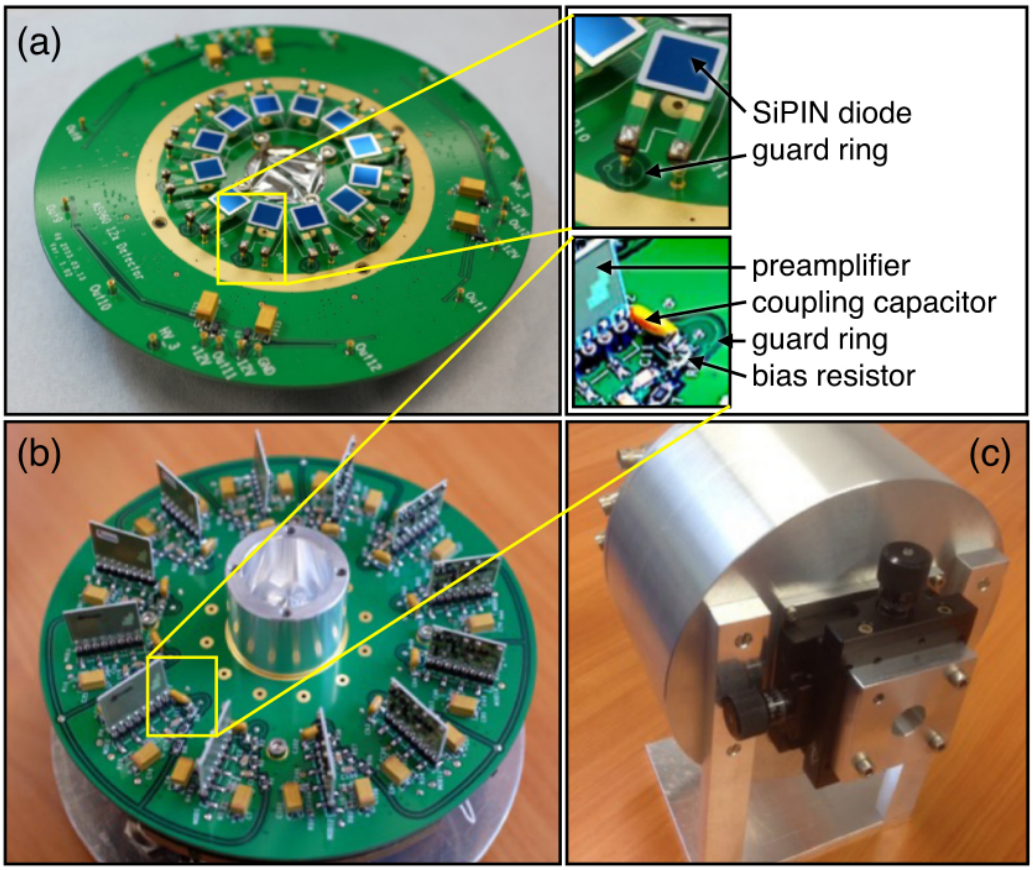


Figure 24: (a) Top side of the motherboard with the mounted SiPIN diodes. (b) Bottom side of the motherboard with the mounted preamplifiers. (c) The assembled polarimeter with the x-y table holding the collimator. Taken from [77]

### 3.2.1 SiPIN Chips

The Compton scattered X-rays are absorbed in twelve SiPIN diodes, which are silicon p-n junctions, with an additional layer of intrinsic, un-doped silicon in between, operated in reverse bias to function as detector chips. In the SiPIN diodes, the X-rays are photoabsorbed and create electron-hole pairs. The number of electron-hole pairs is proportional to the energy of the absorbed X-ray. For radiation with the energy $E_{in}$ above 1.74 keV, the $K$ shell ionisation of the silicon atom is the most significant process [78]. The photoelectron generally leaves the atom with an energy of $E_{in}$-1.74 keV and continues ionising the silicon while the $K$ shell hole is filled by fluorescence or Auger processes. A fraction of the incoming photon energy also goes into the lattice, heating it up. Thus, even though the band gap between the valance and the conduction band is 1.6 eV in silicon, on average, the photon energy necessary to create a single electron-hole pair is 3.65 eV. To separate the electron-hole pair before it recombines, an electric field has to be applied in the

semiconductor. The most often used method to realise this is to use a pn-junction of a semiconductor material in reverse bias.

A p-n junction is an interface between two types of semiconductor material, a p- and an n-type semiconductor inside a single crystal. In the p-doped region holes are the majority charge carrier while in the n-doped region electrons are the majority charge carriers. On their own, p- and n-doped semiconductors are conductive. If they are connected to each other, a depletion zone with no majority charge carriers emerges, see figure 25. By manipulating such junctions, they can be used as diodes, allowing a current flow in only one direction. If no external voltage is applied to the junction, an equilibrium condition is reached with a potential difference across the junction. Electrons from the n-region and holes from the p-region near the p-n interface diffuse in the neighbouring region. The emerging potential difference counteracts the diffusion.

In reverse bias the depletion zone can be extended over the whole volume of the semiconductor chip, which is then empty of free charge carriers. In reverse bias, the n-doped region is biased positively with respect to the p-doped region. Holes in the p-type region are pulled to the negative potential. Electrons in the n-type region are pulled to the positive potential. The width of the depletion zone increases. At the same time the voltage barrier causes a high resistance to the flow of majority carriers. If an X-ray creates electron-hole pairs, they will be separated by the electric field and drift to the contacts, where their charge is collected by preamplifiers.

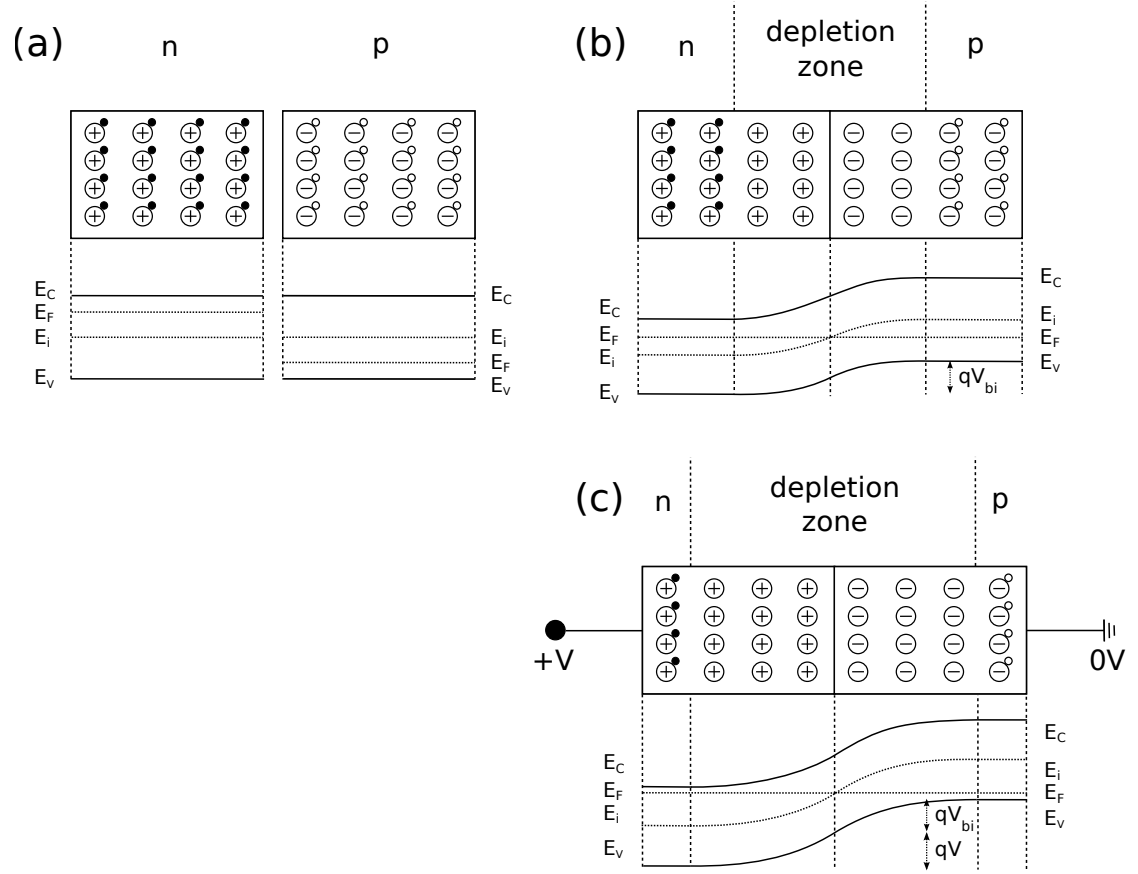


Figure 25: Depletion of a pn-junction in reverse bias. (a) n- and p-doped semiconductor materials. The "p" (positive) side contains an excess of electron holes. The n-side contains an excess of electrons. $E_C$: minimum conduction band energy. $E_F$: Fermi energy. $E_i$: intrinsic semiconductor Fermi energy. $E_V$: maximum valence band energy. (b) n- and p-type semiconductor are brought into contact. A depletion zone emerges. (c) pn-juntion is operated in reverse bias. The depletion zone widens.

In a SiPIN diode there is an additional layer of un-doped silicon in between the p- and n-doped layers. The un-doped, or often weakly n-doped, silicon is an intrinsic semiconductor with an equal amount of free electrons and holes. If the SiPIN diodes is operated in reverse bias, the depletion zone extends into the whole intrinsic region. In comparison to a pn-junction, the depletion zone is larger at the same applied voltage, which provides a larger active area for photodetection.

For data acquisition considerations, the capacity of the detector chips plays a large role. A small capacity leads to smaller signal shaping times. Smaller shaping times in turn lead to a shorter dead time of the detector and thus higher possible count rate. In our case, the fully depleted SiPIN diodes in reverse bias, the depletion zone in between the small n- and p- layers form a plate capacitor with the capacity $C = \epsilon_r \epsilon_0 \frac{A}{d}$, with A as the area of the chips and d as their thickness. For our detector

chips, this leads to a capacitance of 100 pF.

### 3.2.2 Data Acquisition

The small charge produced in the SiPIN chips, $\sim 10^{-15}$C per 60 keV X-ray, makes the use of a preamplifier in the data acquisition system in front of the analogue-to-digital converter (ADC) necessary. The preamplifier, a low-noise general purpose charge sensitive eV-5093 [1], is located as close to the detector chips as possible, right beneath them, to minimise the capacitance noise which comes from the length of the cable between the chips and the preamplifier. The detector chips, represented by its capacity $C_d$ in figure 26, are set on high voltage, -80 V, through bias resistors $R_b$. They are connected to the preamplifiers through coupling capacitances $C_c$. The preamplifiers used in the setup are resistor reset preamplifiers, which means that after the signal amplification the voltage is reset continuously to the base level through a feedback resistor $R_f$.

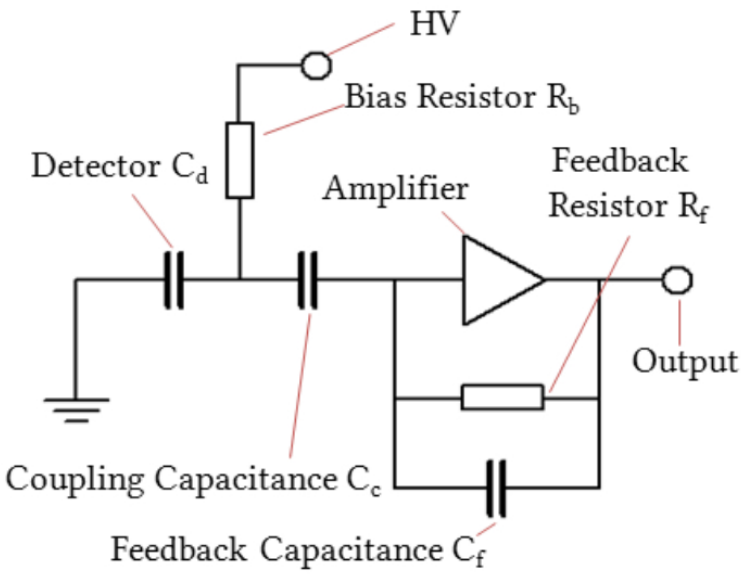


Figure 26: Detector chip bias HV supply and preamplicfication of signals. Taken from [77]

The data acquisition (DAQ) system determines the total energy of the signal and sends it to a computer via a USB connection. The DAQ consists of 64 channels with 8 ADC - analogue to digital converters - in total. It is manufactured by Struck. With a sampling rate of 100 MHz the analogue signal from the preamplifier is digitalised. A moving window deconvolution algorithm is implemented on field programmable

[1] produced by the "eV" company

gate arrays (FPGA) for event selection and signal shaping to reconstruct signal strength.

### 3.2.3 Data Analysis

In the Compton polarimeter the azimuthal angular scattering distribution of Compton scattered X-rays is measured by an array of twelve circularly arranged SiPIN diodes. The distribution is fitted with the Klein-Nishina formula to deduce the degree of linear polarisation of the X-rays. The azimuthal angular scattering distribution is sampled at a given polar angle interval $d\theta$ at a given X-ray energy $\hbar\omega$. In our case the given polar angle interval is around $\theta \simeq 50°$ and the X-ray energy either $\hbar\omega \simeq 13$ keV for krypton or 31 keV for xenon ions. To deduce the degree of linear polarisation P, the Klein-Nishina formula is reorganised.

$$\begin{aligned} \frac{d\sigma}{d\omega} &= \frac{r_0^2}{2}\left(\frac{\hbar\omega'}{\hbar\omega}\right)^2\left(\frac{\hbar\omega'}{\hbar\omega}+\frac{\hbar\omega}{\hbar\omega'}-sin^2\theta-P\,sin^2\theta\,cos\left(2\left(\varphi-\varphi_0\right)\right)\right) \\ X &\equiv \frac{r_0^2}{2}\left(\frac{\hbar\omega'}{\hbar\omega}\right)^2\left(\frac{\hbar\omega'}{\hbar\omega}+\frac{\hbar\omega}{\hbar\omega'}-sin^2\theta\right)\;; \quad Y \equiv \frac{r_0^2}{2}\left(\frac{\hbar\omega'}{\hbar\omega}\right)^2 P\,sin^2\theta \end{aligned} \tag{56}$$

With this notation, the Klein-Nishina formula becomes:

$$\begin{aligned} \frac{d\sigma}{d\omega} &= X - Y cos(2(\varphi-\varphi_0)) \\ P = \frac{1}{M}\frac{Y}{X}\;; \quad &\text{with} \;\; M = \frac{sin^2\theta}{\frac{\hbar\omega'}{\hbar\omega}+\frac{\hbar\omega}{\hbar\omega'}-sin^2\theta} \end{aligned} \tag{57}$$

The parameter M is called modulation factor. It characterises the polarimeter response to 100% linearly polarised X-rays. A high modulation factor is desirable as the uncertainty of P, derived from equation (57), scales with 1/M. The modulation factor of a polarimeter assembly depends on its geometry and is derived from a Monte-Carlo simulation. Through fitting a measured azimuthal angular scattering distribution with equation (57), the parameters X and Y can be deduced.

### 3.2.4 Polarimeter Simulation

A Geant4 [2] Monte Carlo simulation was used to derive the modulation factor of the Compton polarimeter used in the experimental setup. The detector geometry in the simulation is a simplified version of the real polarimeter. It consists of the

[2] https://geant4.web.cern.ch/geant4/

SiPIN diodes, and the epoxy with which they are glued on the printed circuit board (PCB). Furthermore, it consists of a collimator and a scatterer. For experiments with krypton ions, at 13 keV X-ray energies per photon, we used an aluminium collimator and a 10 mm thick beryllium scatterer. For xenon, at X-ray energies of 31 keV, we used a brass collimator and a 15 mm thick boron carbide scatterer. Presented here are the simulation with 31 keV X-rays; we also performed the same simulations with 13 keV X-rays.

A beam of 100% linearly polarised X-rays with 31 keV are generated and collimated to the scatterer, see figure 27. The dominant scattering processes in this energy range were included in the used Geant4 physics list: Compton and Rayleigh scattering. The scattering distribution is sampled by the detector ships, with a geometry exactly like the one of the real polarimeter.

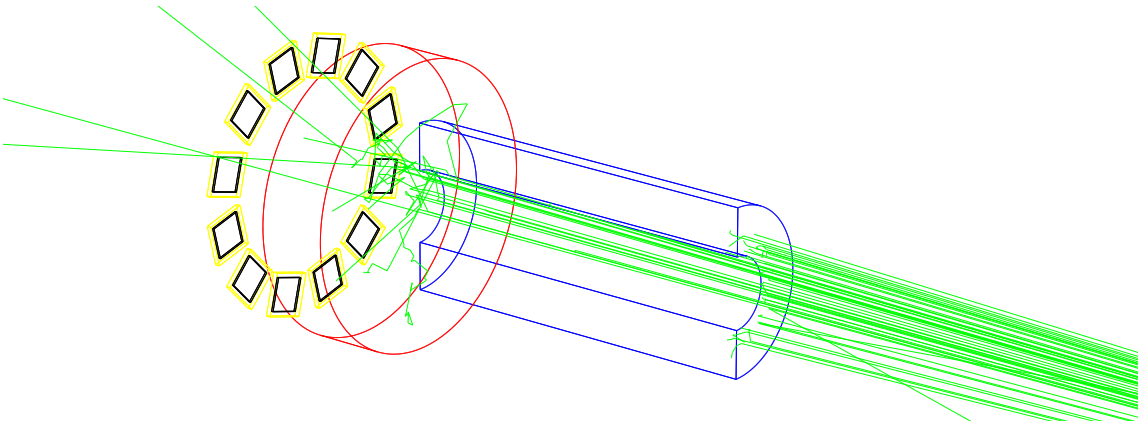

Figure 27: Simulated X-ray events in the SiPIN based polarimeter. Events are simulated in the Geant4 framework. 100% linearly polarised X-rays with 31 keV, shown in green, are generated and collimated by the blue collimator, to the scatterer, shown in red. The scattered X-rays are detected by twelve SiPIN diodes, shown in black. The epoxy, with which they are glued to the PCB, is depicted in yellow.

In each of the twelve detector chips, energy spectra of the scattered X-rays were recorded, see figure 28. The peak at 31 keV corresponds to Rayleigh scattered X-rays. The energy deposition of the X-ray is negligible in Rayleigh scattering for this energy range. The broader peak at 30.3 keV corresponds to the Compton Peak of Compton scattered X-rays. In the actual experiment with the real polarimeter chips, we cannot resolve these two peaks. Plotting the number of counts within these peaks as a function of the azimuthal angle of the particular chips yields the azimuthal angular scattering distribution, see figure 29. We fitted this distribution with the Klein-Nishina formula and obtained a value of $M = 0.318$ for the modulation factor. The contribution of Rayleigh scattering to the scattering events is of the order of

10%. We estimated that taking these events into account, in comparison to only accounting for Compton scattered X-rays, changes the values for the degree of linear polarisation derived in our experiments by approximately 1%. The statistical and systematic errors in the experiments conducted with the SiPIN polarimeter exceed this relative uncertainty of 1% by one order of magnitude, which is why this error is neglected in the data analysis of these experiments. For 13 keV X-rays, the modulation factor is 0.305.

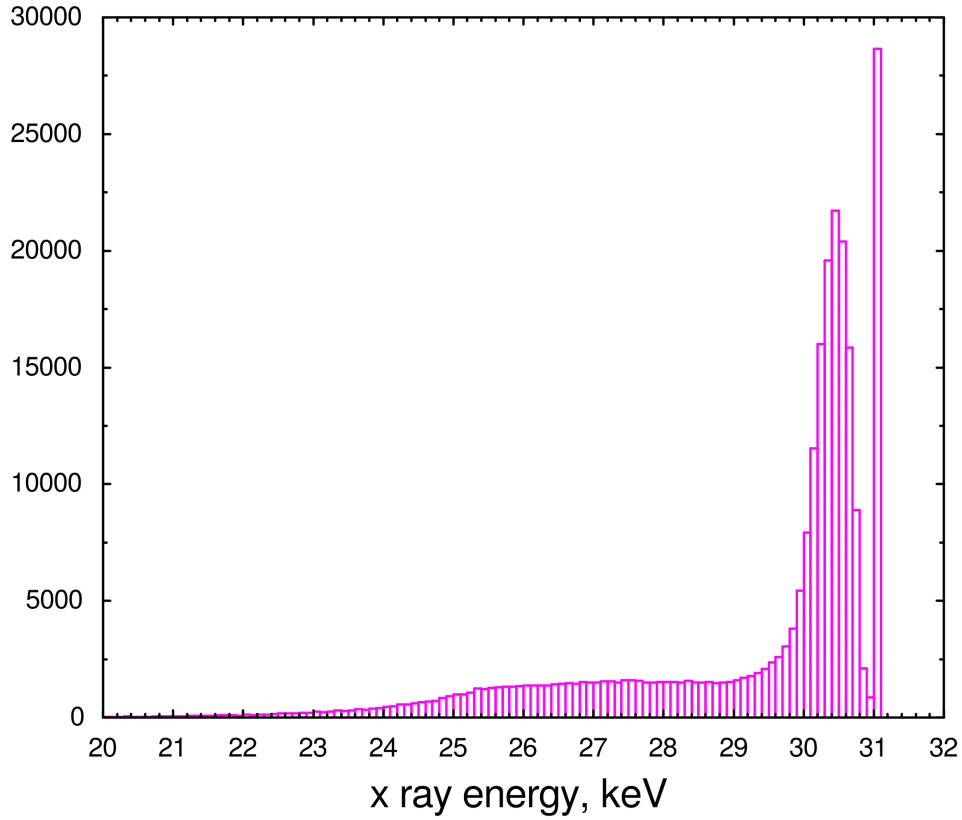


Figure 28: Geant4 simulation of scattered X-rays in the SiPIN polarimeter. The figure shows the energy spectrum of Compton and Rayleigh scattered X-rays, at 31 keV, in beryllium. The peak at 31 keV corresponds to Rayleigh scattered X-rays, while the peak at 30.3 keV corresponds to Compton scattered X-rays.

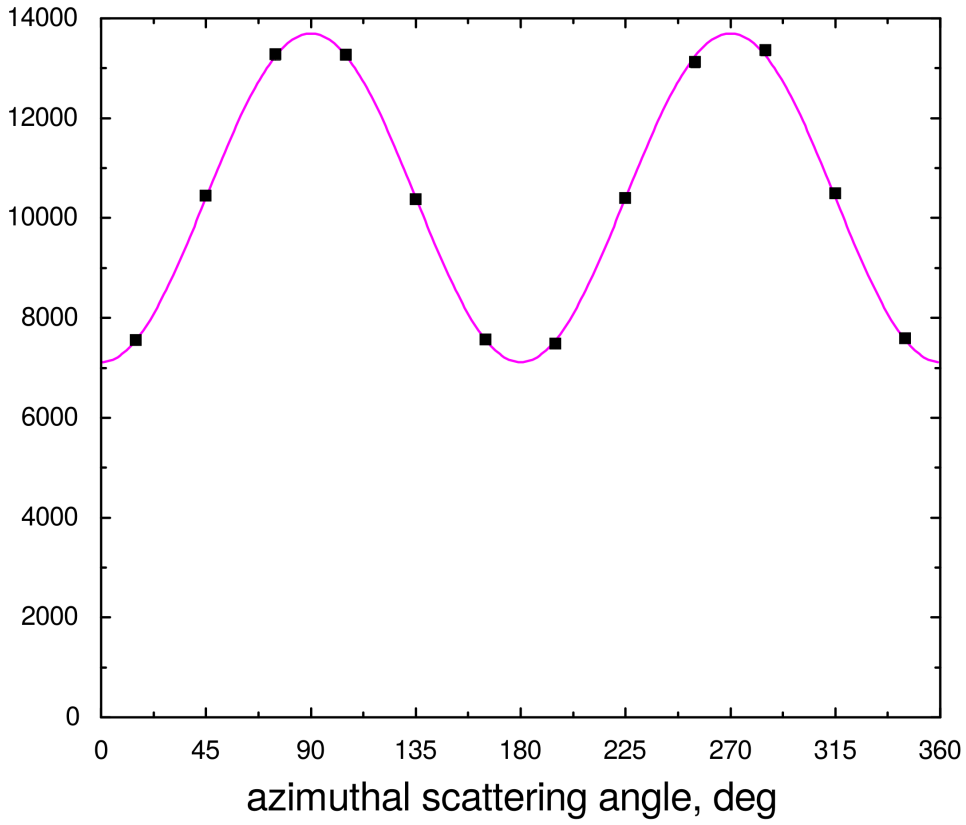


Figure 29: Geant4 simulation of scattered X-rays in the SiPIN polarimeter. The figure shows the azimuthal angular scattering distribution of Compton and Rayleigh scattered X-rays at 31 keV. The distribution is fitted with the Klein-Nishina formula.

# 4 Polarimetry of *KLL* Dielectronic Recombination Transitions into Highly Charged Krypton Ions

In this chapter, the first measurement of the degree of linear polarisation of X-rays emitted by highly charged ions during *KLL* DR using the Compton polarimetry technique is presented. The measurement was performed at the FLASH-EBIT at the Max-Planck Institut für Kernphysik in Heidelberg in December 2013. The experimental setup has already been discussed in chapter 3: it consists of an EBIT, for the production and storage of highly charged krypton ions, and a Compton polarimeter based on SiPIN diode detector chips and a germanium detector for diagnostic purposes, see figure 30. Five *KLL* DR resonances, of which four have a strong polarisation, were investigated, see table 3. The cited values for the degree of linear polarisation are theoretical predictions derived with the FAC framework [36]. For detailed information on the theoretical calculations, see chapter 2.3.3.

| Intermediate State | Electron Beam Energy (keV) | $P_{L,\,theo}$ |
|---|---|---|
| $Be_2$: $[(1s2s^2 2p_{1/2})_1 2p_{3/2}]_{3/2}$ | 9.1978 | 0.42 |
| $Be_3$: $[1s2s^2(2p^2_{3/2})_2]_{5/2}$ | 9.2392 | 0.48 |
| $B_1$: $[1s2s^2 2p^2_{1/2} 2p_{3/2}]_1$ | 9.2968 | 0.40 |
| $He_2$: $[(1s2s)_0 2p_{1/2}]_{1/2}$ | 8.8995 | 0.00 |
| $Li_1$: $[1s2s^2 2p_{1/2}]_1$ | 8.9540 | -0.84 |

Table 3: *KLL* DR resonances into highly charged krypton ions of interest, denoted by their charge state before electron capture, their energy for the recombining electron and their intermediate charge state. Each configuration in this table is in *j-j* coupling notation. The degree of linear polarisation $P_{L,\,theo}$ of their stabilising radiation has been calculated with the FAC code.

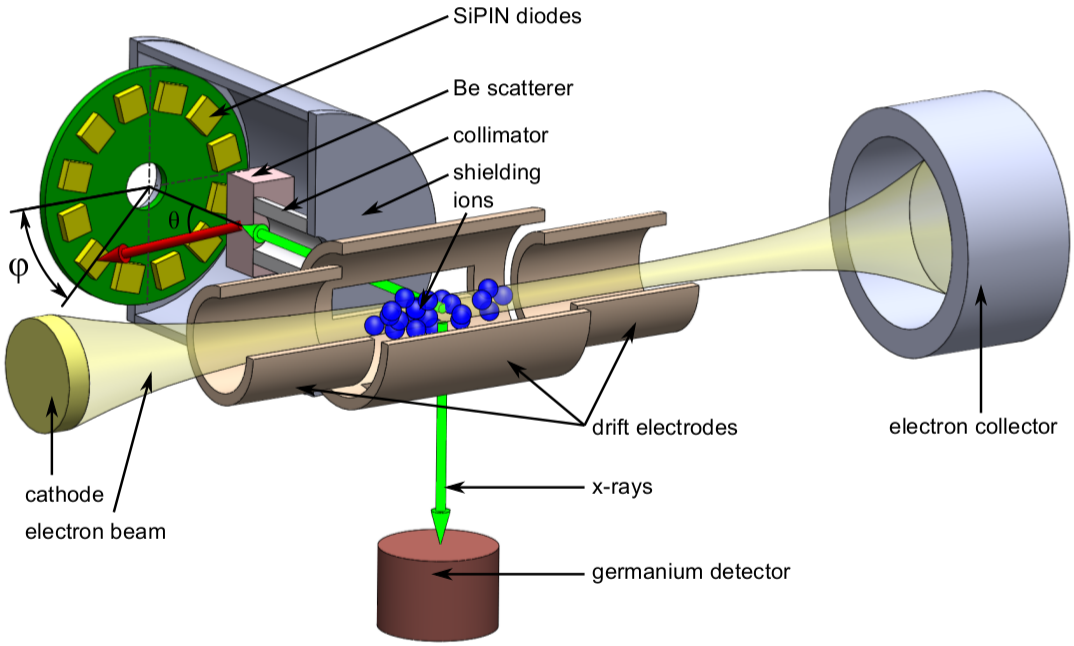


Figure 30: Experimental setup for the measurement of the degree of linear polarisation of *KLL* DR into highly charged krypton ions. Highly charged krypton ions are produced via electron impact ionisation. The polarisation features of X-rays produced in electron-ion recombination are measured by the SiPIN Compton polarimeter. A germanium detector is used for diagnostic purposes. Taken from [79]

The beryllium- and boron-like resonances have high predicted resonance strengths and relatively high degrees of polarisation, which makes them suitable candidates for a proof of principle measurement. The $He_2$ resonance which emits unpolarised X-rays was used to check the polarimeter system for systematic errors. For the $Li_1$ resonance an influence of Breit interaction on the polarisation of the stabilising radiation was predicted from theoretical calculations. With taking only Coulomb interaction into account, the degree of linear polarisation is predicted to be $P_L$ = -0.95; taking Breit interaction into account as well, it becomes $P_L$ = -0.84. To measure the degree of polarisation of the stabilising radiation of these resonances, the electron beam energy is fixed at a corresponding resonance energy. In the Compton polarimeter, the X-rays coming from the ion trap are Compton scattered in a 10 mm thick block of beryllium. The azimuthal angular scattering distribution of these X-rays in the beryllium scatterer is sampled by an array of SiPIN diode chips. The scattering distribution is then fitted with the Klein-Nishina formula, see chapter 2.2.2, to deduce their degree of linear polarisation

## 4.1 Experiment

The experiment consists of three parts. First the krypton *KLL* DR resonances had to be identified. To do that, the FLASH-EBIT had to be configured to achieve a good enough energy resolution for the electron beam energy to resolve the resonances while still producing a sufficiently high enough yield of DR X-rays to be able to perform polarimetry experiments. The second step was deducing the radiative recombination (RR) background, see chapter 2.3.1. The last step was to perform the polarimetry measurement for the resonances of interest.

### 4.1.1 Identifying the *KLL* DR Resonances

To identify the Kr *KLL* DR resonances at electron beam energies of 8.8 - 9.7 keV and X-ray energies of approximately 13 keV, a high purity germanium detector is used to record energy spectra of X-rays from the trap. An electron beam with a current of approximately 100 mA is guided through a magnetic field of 6 T to the centre of ion trap, where it has a beam diameter of approximately 50 µm. A collimated beam of krypton gas is injected into the trap with an injection pressure of $4{\cdot}10^{-7}$ mbar. The trap depth, the potential of the central drift tube in relation to neighbouring tubes, was set to 45 V. Every 300 s the trap is dumped by raising the potential of the central drift tube for 3 s to keep heavy highly charged ions, like tungsten and barium emitted from the cathode, from accumulating in the trap.

Plotting the X-ray energy spectra as a function of electron beam energy, while performing scans of the Kr *KLL* DR energy region, yields a two dimensional spectrum of the *KLL* DR resonances, see figure 31(a). The horizontal line of bright spots at an X-ray energy of 13 keV are the *KLL* DR resonances of highly charged Kr ions. They are located on a diagonal line, nearly invisible in the spectrum, which is due to non resonant *L* shell RR. Figure 31(b) shows a projection of the X-ray events with an X-ray energy in the DR range on the electron beam energy axis. The DR resonances of different charge states and via different intermediate states are clearly visible on top of a non-resonant RR background. With the operating parameters of the FLASH-EBIT, a resolution of the electron beam energy of approximately 20 eV at 9.1978 keV was achieved. To identify the DR resonances, FAC calculations were carried out to deduce the energy and resonance strength of the DR resonances of highly charged Kr ions in the He- through O-like charge states. Figure 31(c) shows the calculated spectrum. To interpret this spectrum and to compare it to the measured one, it is necessary to keep in mind that, for the calculated resonance strengths, the ion abundance of different charge states was not taken into

account. To conduct experiments yielding resonance strengths, completely different scan schemes are used [61]. Absolute resonance strengths have no importance for the purposes of this experiment. Thus, only the calculated electron energies of the resonances were used to locate the DR resonances of interest. The two well resolved resonances, $He_1$ and $O_1$ at 8.8206 keV and 9.6542 keV, respectively, were used to calibrate the electron beam energy.

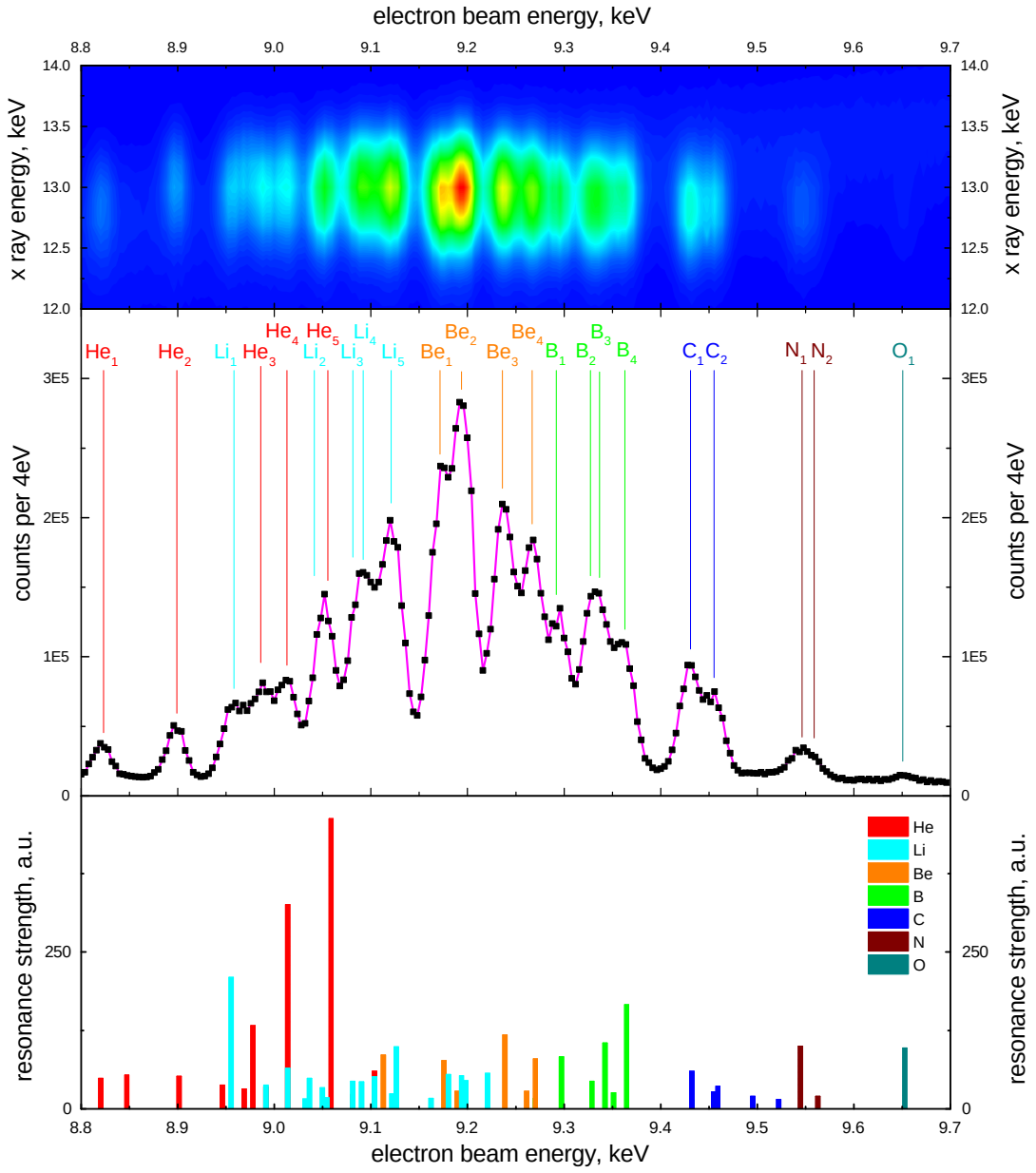


Figure 31: (a) Intensity plot of X-ray events measured while perfoming scans with the electron beam energy. (b) Projection of the X-ray events with an X-ray energy in the *KLL* DR range on the electron beam energy axis. The resonances are identified with the help of FAC calculations, depicted in (c).

X-ray energy spectra were recorded by using the germanium detector while simultaneously scanning the electron beam energy through the region of the *KLL* DR resonances. Figure 32 shows an energy spectrum recorded by using the germanium detector for the electron beam energy tuned into the $Be_3$ resonance. The energy resolution of the germanium detector was 750 eV FWHM at 13 keV. For energies lower than 10 keV, the spectrum is dominated by bremsstrahlung. The lines at approximately 3 keV and 5 keV are due to trapped impurity ion species. The main peak at 13 keV is due to *KLL* DR and *L* shell RR into highly charged krypton ions. Thus, the contribution of RR to the *KLL* DR X-ray line has to be deduced.

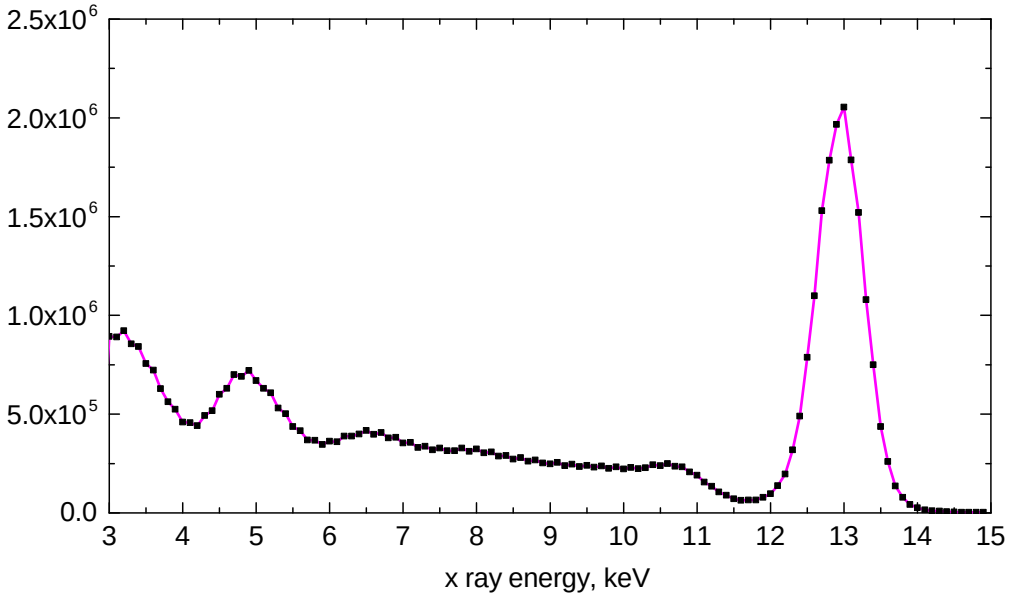


Figure 32: An X-ray spectrum in the germamium detector with the electron beam energy in the region of the $Be_3$ *KLL* DR resonance of highly charged krypton.

### 4.1.2 Deducing the Radiative Recombination Background

In order to be able to analyse the data from the Compton polarimeter for the *KLL* DR X-ray lines, the level of background X-rays due to RR has to be deduced. When tuning into a *KLL* DR resonance with the electron beam energy and analysing the X-ray energy spectra in the polarimeter chips, it is impossible to distinguish between X-rays coming from the DR and the RR processes, see figure 35. Therefore, the RR background contribution to the *KLL* DR peaks was deduced from the measured energy spectra, see figure 33 and 34. The resonances of interest, and their neighbouring lines, were fitted with Gaussian profiles, while the RR background was fitted with a first order polynomial because for small electron beam energy intervals

around the resonances of interest, the RR background is approximately linear. The RR contributions $f_{RR}$ to the DR peaks, with $f_{DR}+ f_{RR} =1$, are:

| Intermediate State | $f_{RR}$ |
|---|---|
| $Be_2$ | 0.10 |
| $Be_3$ | 0.12 |
| $B_1$ | 0.19 |
| $He_2$ | 0.26 |
| $Li_1$ | 0.21 |

Table 4: Contribution of RR X-rays, $f_{RR}$, to the DR X-ray lines.

Furthermore, FAC calculations were carried out to deduce the degree of linear polarisation of the RR background X-rays, which was found to be $P_{RR}=0.59\pm0.15$. The error for this calculated value is due to an uncertainty about the charge state distribution of the krypton ions in the trap.

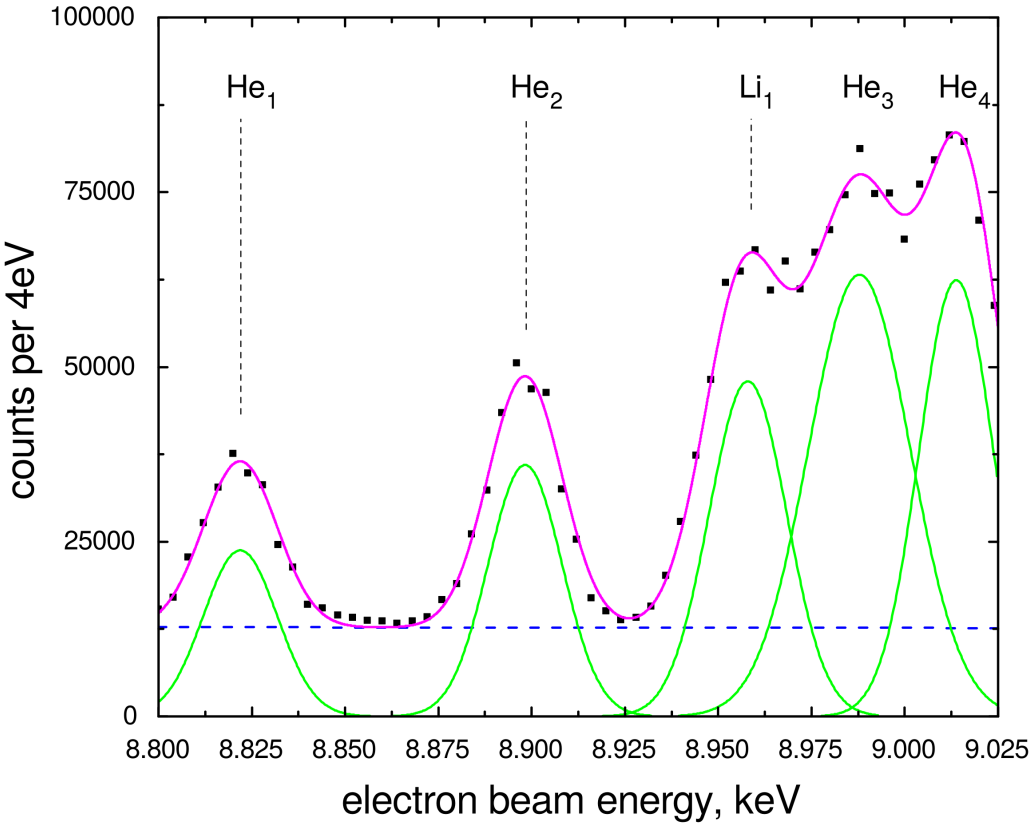


Figure 33: Projection of the X-ray events with an X-ray energy in the *KLL* DR range on the electron beam energy axis for electron beam energies in the region around the $He_2$ and $Li_1$ resonances. The magenta line is the fit of the intensity function. Lines corresponding to different DR resonances are in green and the background due to RR is the blue dotted line.

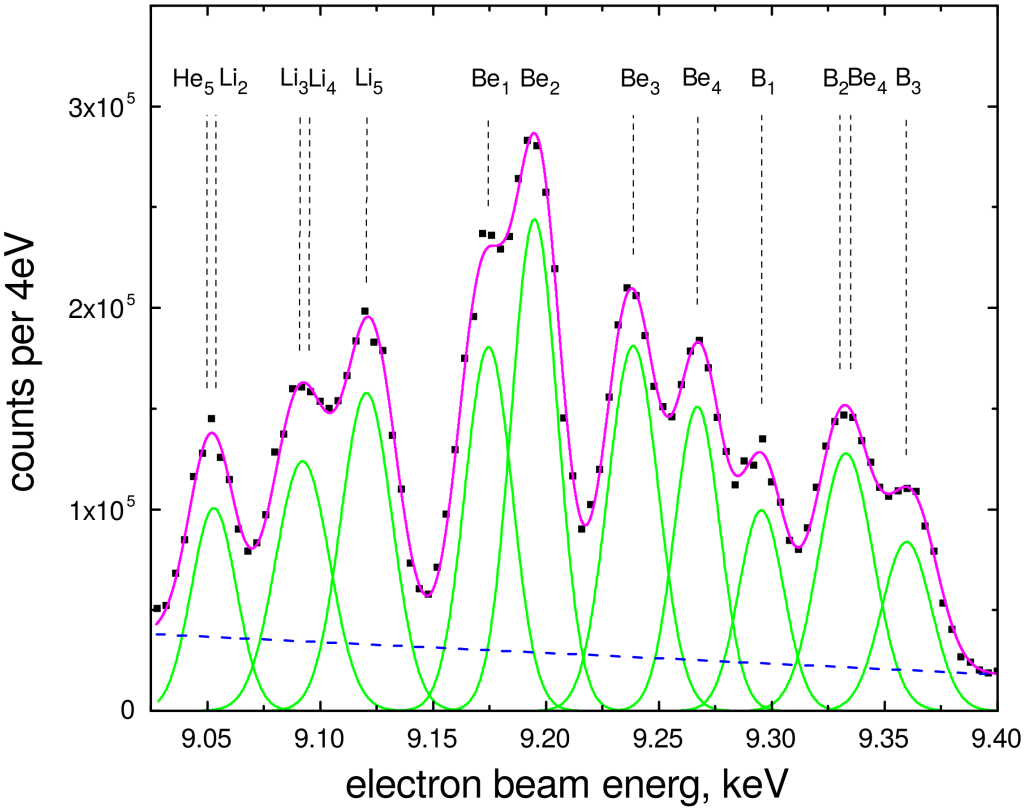


Figure 34: Same as figure 33 except for electron beam energies around the $Be_2$, $Be_3$ and $B_1$ resonances.

### 4.1.3 Polarimetry

The Compton polarimeter, placed perpendicular to the electron beam propagation direction, was used to measure the degree of linear polarisation of the *KLL* DR X-rays. With the electron beam energy tuned into a DR resonance of interest, energy spectra in the twelve polarimeter channels were recorded. Due to changes in the temperature and pressure in the EBIT, small shifts of energies of the DR resonances can occur. To prevent the electron beam energy to go off resonance, the recording was stopped every twelve hours and scans over the DR region were conducted to adjust the beam energy to account for possible shifts.

Figure 35 shows a typical energy spectrum in one of the polarimeter channels. The feature below 6 keV is due to electronic noise. The broad peak at 13 keV encompasses *L* shell RR and *KLL* DR X-rays. The peak at 13 keV was fitted with a Gaussian profile and the background was approximated by a first order polynominal. The energy resolution varied substantially for the detector chips from 3.2 keV to 4.0 keV FWHM at 13 keV.

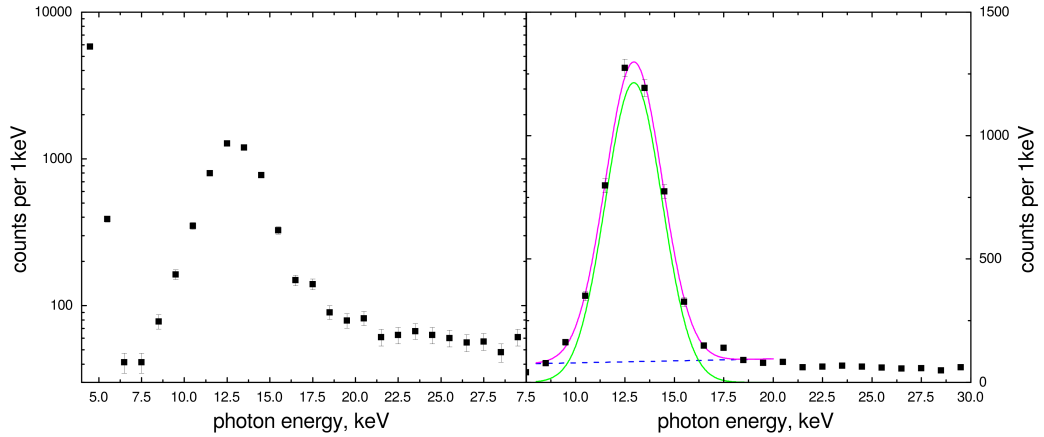


Figure 35: Energy spectrum of scattered X-rays in a SiPIN polarimeter channel with the electron beam energy tuned into the $Be_2$ *KLL* DR resonance of highly charged krypton. The spectrum on the left is in logarithmic scale and shows the feature due to electronic noise below 6 keV. The spectrum on the right shows the fit, the magenta line, of the *KLL* DR X-ray line. A gaussian function, the green line, is used to fit the line. A first order polynominal, the blue dashed line, is used to approximate the background.

Figure 36 shows the energy spectra of the channel with the most statistics for each of the measured DR lines. For the $Be_2$ and $Be_3$ resonances, as well as for the $He_1$ resonance, the most DR X-ray events were accumulated. Especially for the $Li_1$ resonance, the statistics we accumulated are relatively low as compared to the level of background.

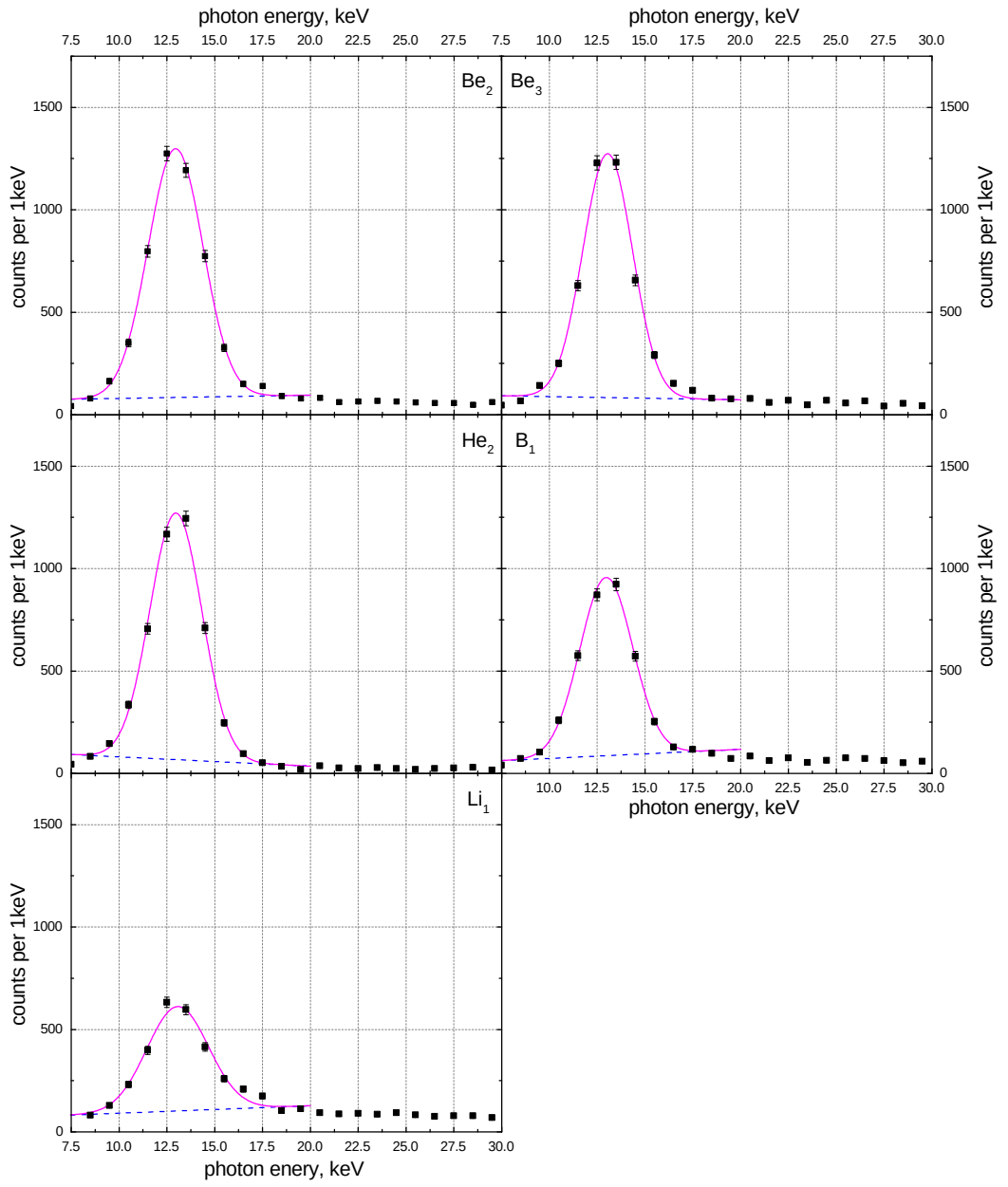


Figure 36: Energy spectra of scattered X-rays in the SiPIN polarimeter channels with the most statistics for each of the measured *KLL* DR lines of highly charged krypton. The fitted line shapes are in magenta, the fitted background is the blue dashed line.

Figures 37 and 38 show the energy spectra in each of the twelve polarimeter channels for the $Be_2$ resonance. The figures show the accumulated DR, and RR, events for different azimuthal scattering angles. There are two maxima in intensity at scattering angles of 90° and 270°, as well as minima in between the maxima. The energy spectra for all polarimeter channels are fitted with Gaussian profiles to deduce the scattering intensity, i.e. the area under the Gaussian profile. This

procedure is repeated for all DR resonances of interest. Figure 39 shows the intensity modulation, i.e. the area under the Gaussian as a function of azimuthal scattering angle, for each of the five resonances.

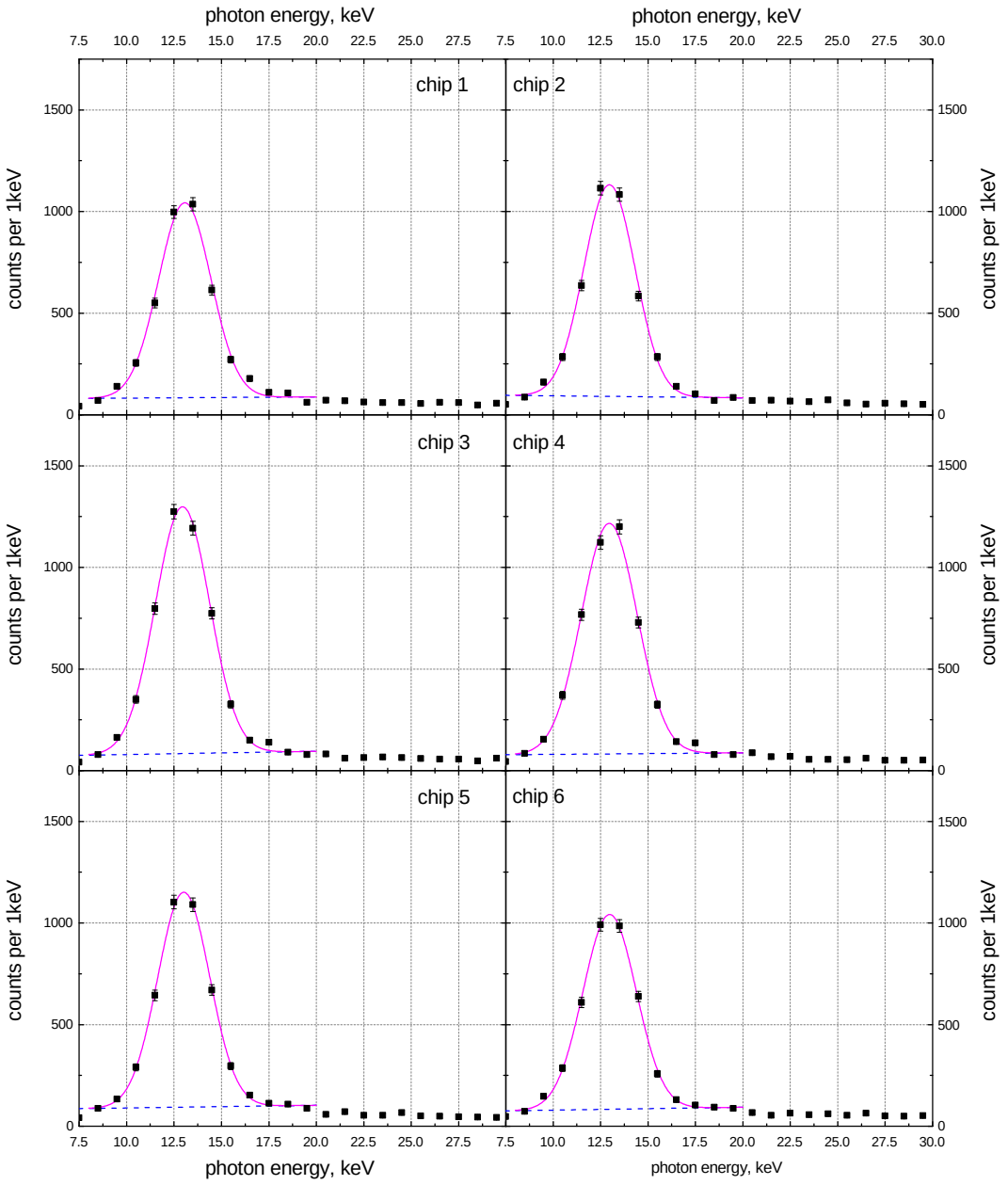


Figure 37: Energy spectrum of scattered X-rays in the first six SiPIN polarimeter channels with the electron beam energy tuned into the $Be_2$ *KLL* DR resonances of highly charged krypton. The fitted line shapes are in magenta, the fitted background is the blue dashed line.

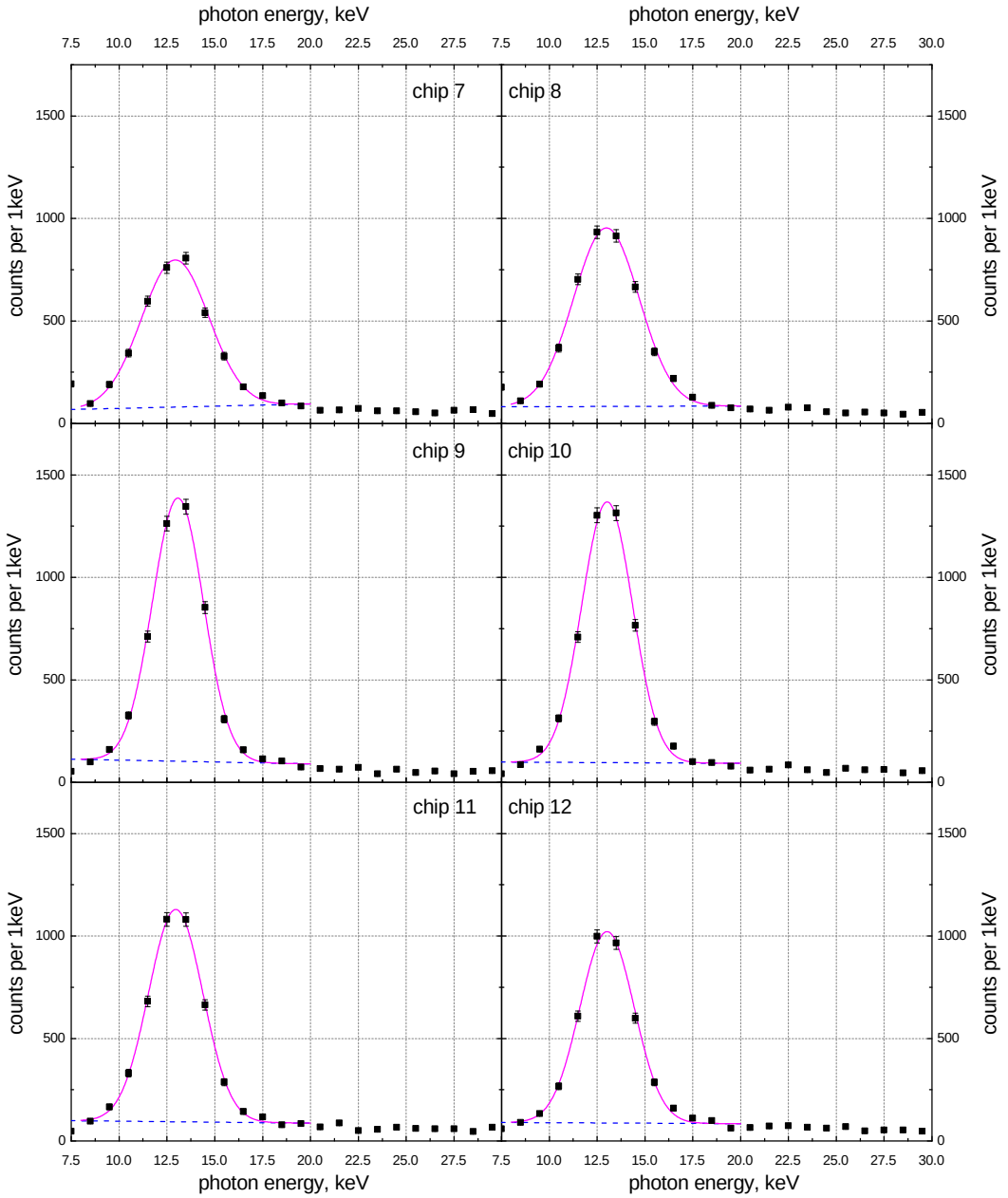


Figure 38: Same as figure 37 except for channel seven to twelve.

## 4.2 Results

Plotting the azimuthal angular scattering intensity modulations for all measured resonances yields figure 39. The modulations for the $Be_2$, $Be_3$ and $B_1$ resonances are similar in form. The varying strengths of the modulations indicates different degrees of linear polarisation. The rather flat modulation for the $He_2$ resonance indicates a very low degree of linear polarisation. For the $Li_1$ line, the modulation is inverted in comparison to the other measured modulations. This indicates a

negative degree of linear polarisation.

For the fitting of these azimuthal angular scattering distributions with the Klein-Nishina formula, the RR contribution to the DR peaks, see table 4, has to be taken into account. The measured degree of polarisation consists of a part due to RR, $f_{RR}$, and a part due to DR, $1 - f_{RR}$.

$$\frac{d\sigma}{d\omega} = (1 - f_{\mathrm{RR}})(X - Y cos(2 \cdot (\varphi - \varphi_0))) + f_{\mathrm{RR}}(X - M P_{\mathrm{RR}} X cos(2 \cdot (\varphi - \varphi_0))) \quad (58)$$

$X$, $Y$ and $\varphi_0$ are left as free fitting parameters. Here, $\varphi_0$ accounts for possible geometrical misalignment of the electron beam axis. The fits yield the following values for the degrees of linear polarisation, see table 5.

| Intermediate State | $P_{L,\,exp}$ | $P_{L,\,theo\,(C+B)}$ | $P_{L,\,theo\,(C)}$ |
|---|---|---|---|
| $Be_2$: $[(1s2s^2 2p_{1/2})_1 2p_{3/2}]_{3/2}$ | 0.45±0.03 | 0.42 | 0.42 |
| $Be_3$: $[1s2s^2(2p^2_{3/2})_2]_{5/2}$ | 0.43±0.03 | 0.48 | 0.48 |
| $He_2$: $[(1s2s)_0 2p_{1/2}]_{1/2}$ | 0.01±0.03 | 0.00 | 0.00 |
| $B_1$: $[1s2s^2 2p^2_{1/2} 2p_{3/2}]_1$ | 0.36±0.04 | 0.40 | 0.41 |
| $Li_1$: $[1s2s^2 2p_{1/2}]_1$ | -0.72±0.09 | -0.84 | -0.95 |

Table 5: Polarimeter results for the degree of linear polarisation for *KLL* dielectronic recombination lines for highly charged krypton ions, denoted by their intermediate charge state. Measured degree of linear polarisation $P_{L,\,exp}$, in comparison with the theoretical calculations (FAC) taking only Coulomb interaction into account $P_{L,\,theo\,(C)}$ and also accounting for Breit interaction $P_{L,\,theo\,(C+B)}$.

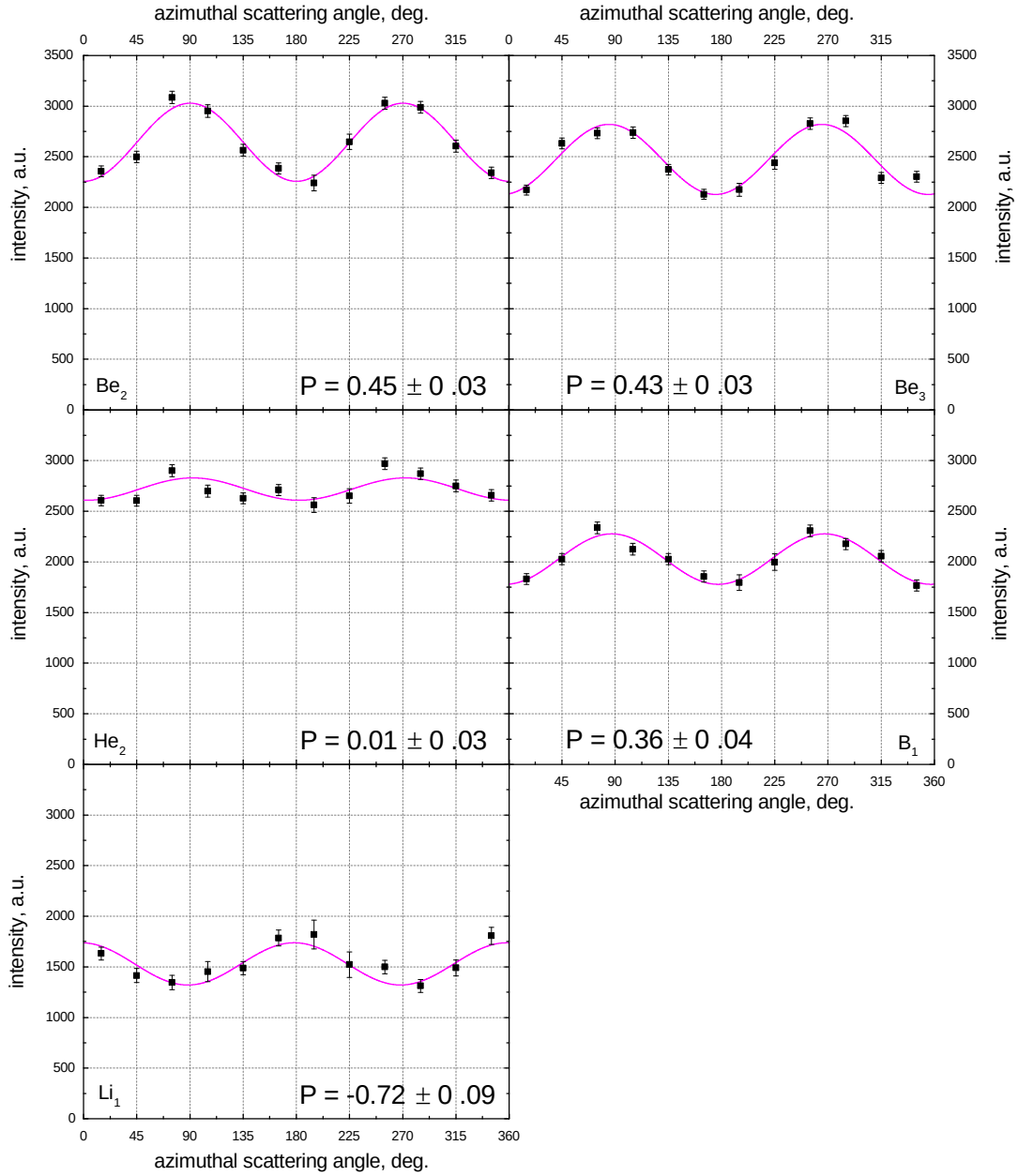


Figure 39: Measured azimuthal angular scattering distributions of X-rays due to *KLL* dielectronic recombination into highly charged krypton ions for different DR resonances.

## 4.3 Conclusion: Magnetic Sublevel Population of Excited Intermediate States

As discussed in the chapter on the polarisation of DR lines 2.3.3, the polarisation of the RS in the DR process depends on the population of the magnetic sublevels $\sigma_m$ of the intermediate state $|\alpha_d J_d, m_d\rangle$, produced by the resonant electron capture. Aligned states produce polarised radiation. In our case, by measuring the polarisation of the RS in DR, we probe the alignment of the intermediate states, the distributions of $\sigma_m$. To discuss the magnetic sublevel population of the intermediate state for the measured resonances and the resulting degree of linear polarisation, the total angular momenta of the initial and intermediate states, as well as the total angular momentum of the most likely final state, have to be taken into account. For the resonances of interest, the RS to the dominant final state has a radiative decay rate of at least one order of magnitude higher than the second strongest. For the computation of the polarisation of DR lines, transitions to all possible final states are taken into account. For this illustration here, only the strongest decay is taken into account.

| Resonance | Initial State | Intermediate State | Final State |
|---|---|---|---|
| $Be_2$ | $[1s^2 2s^2]_0$ | $[(1s2s^2 2p_{1/2})_1 2p_{3/2}]_{3/2}$ | $[1s^2 2s^2 2p_{1/2}]_{1/2}$ |
| $Be_3$ | $[1s^2 2s^2]_0$ | $[1s2s^2(2p^2_{3/2})_2]_{5/2}$ | $[1s^2 2s^2 2p_{3/2}]_{3/2}$ |
| $He_2$ | $[1s^2]_0$ | $[(1s2s)_0 2p_{1/2}]_{1/2}$ | $[1s^2 2s]_{1/2}$ |
| $B_1$ | $[1s^2 2s^2 2p_{1/2}]_{1/2}$ | $[1s2s^2 2p^2_{1/2} 2p_{3/2}]_1$ | $[1s^2 2s^2(2p^2_{1/2})_0]_0$ |
| $Li_1$ | $[1s^2 2s]_{1/2}$ | $[1s2s^2 2p_{1/2}]_1$ | $[1s^2 2s^2]_0$ |

Table 6: Initial, intermediate and most likely final states of the measured *KLL* DR resonances of highly charged krypton ions.

The $He_2$ *KLL* DR resonance was used to probe for systematic effects in the polarimeter setup which influence the measured degree of linear polarisation. The intermediate state of the $He_2$ resonance has a angular momentum of $J_d = 1/2$ and thus the magnetic substates $m_d$=+1/2, -1/2, which have the same population probability. Therefore, the $He_2$ line is unpolarised. The experimental value for the degree of linear polarisation, $P_{L,He_2}$=0.01±0.03, rules out systematic effects in the polarimeter affecting the polarisation measurements.

The $Be_2$, $Be_3$ and $B_1$ resonances have a positive degree of linear polarisation. In the non-relativistic limit, this can be explained by taking into account which magnetic sublevels of the intermediate states are allowed to be populated for each

resonance. The free electron has its angular momentum perpendicular to the electron beam direction in the rest frame of the ion. Ionic substates with the least projection of the total angular momentum on the quantisation axis are populated with the highest probability. For the $Be_2$ and $Be_3$ resonances, these are sublevels with $|m_d|$ =1/2. For the $B_1$ resonance, these are the states with $|m_d|$ =0. In all three cases, this leads to negative alignment parameters, see equations (49), (50) and (48). For transitions to the dominant final states, with $J_f$=1/2, 3/2 and 0, respectively, the anisotropy parameters are $\alpha_2^{\gamma,f}$=1/2, $\sqrt{7}/(5\sqrt{2})$ and $1/\sqrt{2}$, which leads to a positive degree of linear polarisation for the $Be_2$, $Be_3$ and $B_1$ resonances, see equation (51).

For the $Li_1$ resonance, the population of the magnetic sublevel with $|m_d|$ =0 is forbidden in the non-relativistic limit [6]. In the collision, substates with $|m_l|$ =0 are predominantly populated. For its intermediate state $[1s2s^22p\ ^3P_1]_1$, which is product state of a spatial $|L = 1, m_l\rangle$ and a spin part $|S = 1, m_s\rangle$, the only possible combinations of momenta are given by the Clebsch-Gordan coefficients $\langle 1110|11\rangle$ and $\langle 1010|10\rangle$, for which only the former has a value different from zero. Therefore sublevels with $|m_d|$ =1 are populated, which leads to a positive alignment parameter, see equation (48). With an anisotropy parameter $\alpha_2^{\gamma,f}$=$1/\sqrt{2}$, this yields a negative degree of polarisation, see equation (51). In a relativistic treatment, the cross section for the population of magnetic sublevels with $|m_d|$ =0 becomes bigger due to spin-orbit interaction, which modifies the degree of polarisation of the RS.

Calculations using two different descriptions of the electron-electron interaction operator during the resonant electron capture were performed: calculations which only take Coulomb interaction into account, as well as fully accounting for the relativistic electron-electron interaction, with the Breit interaction term included. The Breit term enters directly in the calculations of the transition matrix elements $\langle \alpha_d J_d||V||\alpha_0 J_0, lj : J_d\rangle$ as V=$V_C$+$V_B$, with the Coulomb potential $V_C$ and the Breit potential $V_B$. As mentioned before, Breit interaction does not play a role if only a single partial wave of a free electron is allowed for the particular transition, see chapter 2.3.3. This is the case for the two beryllium-like resonances measured here, $Be_2$ and $Be_3$. The total angular momentum of their initial state is 0: $\left[1s^22s^2\right]_0 + e \longrightarrow \left[1s2s^22p_{1/2}2p_{3/2}\right]_{3/2,5/2}$. Thus only the $d_{3/2}$ and $d_{5/2}$ partial electron waves contribute to the formation of the $Be_2$ and $Be_3$ resonances, respectively. For the $B_1$ resonance, $\left[1s^22s^22p_{1/2}\right]_{1/2} + e \longrightarrow \left[1s2s^22p_{1/2}^22p_{3/2}\right]_1$, the $s_{1/2}$ and $d_{3/2}$ electron partial waves are allowed. For the $Li_1$ resonance, $\left[1s^22s\right]_{1/2} + e \longrightarrow \left[1s2s^22p_{1/2}\right]_1$, the $p_{1/2}$ and $p_{3/2}$ partial waves contribute. Therefore in the case of $B_1$ and $Li_1$, interference of different partial waves of the free electron enters into the calculation

of the matrix transition element and the polarisation of the RS depends on the interaction operator and thus on the Breit interaction term. For the $B_1$ resonance, the degree of linear polarisation becomes $P_{L,\,theo\,(C+B)}$ =-0.40 in fully relativistic calculation in comparison to $P_{L,\,theo\,(C)}$ =-0.41 with only the Coulomb interaction included, which is far from resolvable with the precision of the present experiment. For the $Li_1$ resonance, the degree of linear polarisation becomes $P_{L,\,theo\,(C+B)}$ =-0.84 in a fully relativistic calculation in comparison to $P_{L,\,theo\,(C)}$ =-0.95. In terms of the population of magnetic sublevels, this means that for the $Li_1$ resonance, the population of the $|m_d|$ =0 sublevels increases by a factor of 30. The experimental value of $P_{L,\,exp}$=-0.72±0.09 has too big an error to draw any conclusions of the influence of Breit interaction on the electron-electron interaction in DR for highly charged krypton ions.

To conclude, analysing the degree of linear polarisation of X-rays emitted in *KLL* DR into highly charged krypton ions probes the alignment of the doubly-excited intermediate state, which, in the non-relativistic limit, can be explained by illustrating which magnetic sublevels are allowed to be populated. Calculations which only take Coulomb interaction between electrons into account, as well as fully relativistic calculations taking also Breit interaction into account, have been performed to further our understanding of relativistic particle dynamics under the presence of strong electromagnetic fields. Unfortunately, the accumulated statistics do not allow any decisive statement concerning the influence of Breit interaction on the electron-electron interaction in DR.

# 5 Influence of Breit Interaction on the Polarisation of *KLL* Dielectronic Recombination Transitions

In this chapter, the first measurement of the influence of Breit interaction on the degree of linear polarisation of X-rays emitted by highly charged ions during *KLL* DR is presented. The measurement was performed at the HD-EBIT at the Max-Planck Institut für Kernphysik in Heidelberg in March 2014. The experimental setup has already been discussed in chapter 3: it consists of an EBIT, for the production and storage of highly charged xenon ions, and a Compton polarimeter based on SiPIN detector chips and germanium detector for diagnostic purposes, see figure 40. Three *KLL* DR resonances with strong polarisations were investigated, see table 7. The cited values for the degree of linear polarisation are theoretical predictions derived with the FAC and RATIP [37] framework, which are consistent. For detailed information on the theoretical calculations, see chapter 2.3.3.

| Intermediate State | Electron Energy (keV) | $P_{L,\,theo}$ |
|---|---|---|
| $Be_2$: $[(1s2s^22p_{1/2})_1 2p_{3/2}]_{5/2}$ | 21.075 | 0.50 |
| $Be_3$: $[(1s2s^22p_{1/2})_0 2p_{3/2}]_{3/2}$ | 21.112 | 0.40 |
| $Li_1$: $[1s2s^22p_{1/2}]_1$ | 20.454 | -0.44 |

Table 7: Dielectronic recombination resonances of interest for *KLL* DR into highly charged xenon ions, denoted by their charge state before electron capture: their energy for the recombining electron, their intermediate charge state and the calculated degree of linear polarisation $P_{L,\,theo}$ of their stabilising radiation. Each configuration in this table is in *j-j* coupling notation.

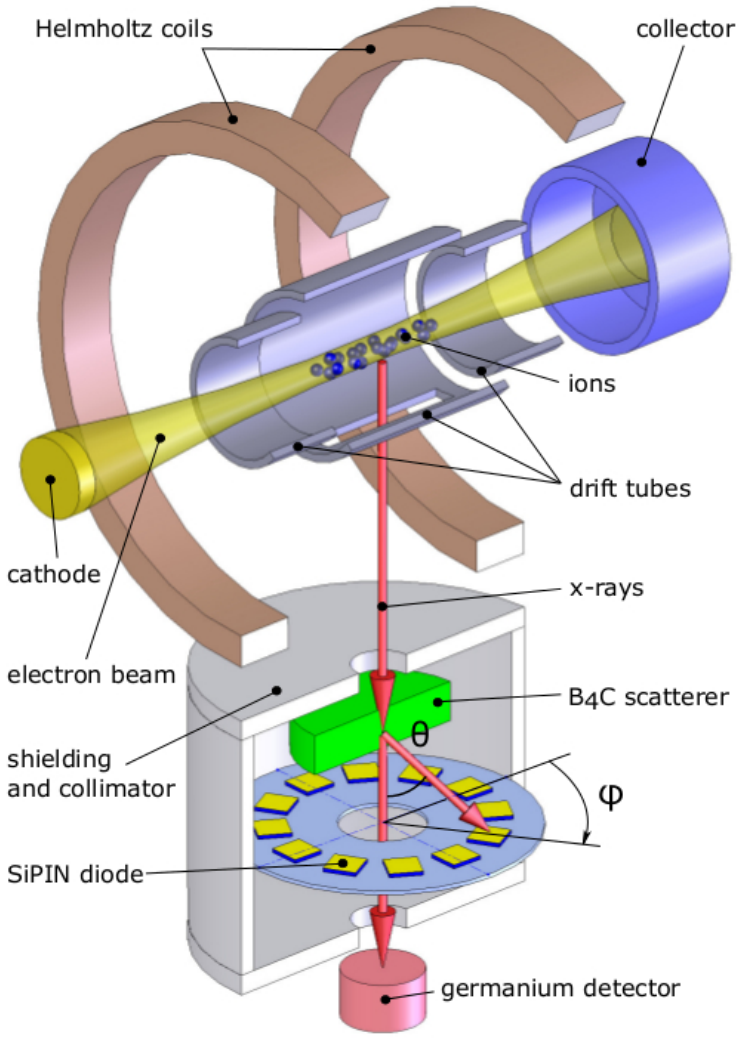


Figure 40: Experimental setup for the first measurement of the influence of Breit interaction on the degree of linear polarisation of *KLL* DR into highly charged xenon ions. Highly charged xenon ions are produced via electron impact ionisation. The polarisation features of X-rays produced in electron-ion recombination are measured by the SiPIN Compton polarimeter. A germanium detector is used for diagnostic purposes. In the actual setup, the detectors are placed at the side window of the ion trap. For illustrative purposes, they are placed below the trap in this figure.

In many ways this experiment is similar to the polarisation measurement of *KLL* DR lines of highly-charged krypton ions performed by our group at the FLASH-EBIT in 2013, see chapter 4. The main goal of the experiment with xenon ions was to clearly resolve the influence Breit interaction has on the polarisation of the stabilising radiation of the $Li_1$ resonance of highly charged xenon ions. Theory calculations have been carried out by Fritzsche et al. [6] to predict a substantial influence. Taking Breit interaction into account reduces the degree of polarisation from $P_{L,\,theo\,(C)} = -0.95$ to $P_{L,\,theo\,(C+B)} = -0.44$. The beryllium-like $Be_2$ and

$Be_3$ resonances were chosen because of their high resonance strength and relatively high degree of polarisation of their stabilising radiation, which is not influenced by Breit interaction. Their polarisation was measured to check the functionality of the polarimeter system.

To measure the degree of polarisation of the stabilising radiation of these resonances, the electron beam energy is fixed at a corresponding resonance energy. In the Compton polarimeter, the X-rays coming from the ion trap are Compton scattered in a 15 mm thick block of boron carbide. The azimuthal angular scattering distribution of these X-rays in the boron carbide scatterer is sampled by an array of SiPIN diode chips. The scattering distribution is then fitted with the Klein-Nishina formula, see chapter 2.2.2, to deduce their degree of linear polarisation.

Because in the here described measurements resonances of xenon are investigated, instead of krypton as in chapter 4, the X-ray energies are considerably higher. Namely, for xenon, the emitted photons have an energy of 31 keV. Hence the employed polarimeter needs to be optimised for this higher energy. In comparison to the krypton experiment, a plate of boron carbide was chosen as scatterer because at an X-ray energy of 31 keV it performs better than beryllium [77]. Another difference was that the germanium detector, detecting unscattered X-rays for diagnostic purposes, is placed behind the polarimeter. This was a necessary arrangement because no other X-ray window to the trap was available at the HD-EBIT. X-rays impinging on the germanium crystal are in this arrangement attenuated by the boron carbide scatterer, which is particularly pronounced at energies below 20 keV.

## 5.1 Experiment

Similar to the experiment with krypton ions, the HD-EBIT was configured to resolve and identify the xenon *KLL* DR resonances while still producing a high enough yield of DR X-rays to be able to perform polarimetry experiments. Then the RR contribution to the DR line was deduced. The last step was to perform the polarimetry measurement for the resonances of interest.

### 5.1.1 Identifying the *KLL* DR Resonances

To identify the Xe *KLL* DR resonances at electron beam energies of 20.2 - 22.2 keV and X-ray energies of approximately 31 keV, a high purity germanium detector is used to record energy spectra of X-rays from the trap. An electron beam with a current of approximately 400 mA is guided through a magnetic field of 8 T to the centre of ion trap, where it has a beam diameter of approximately 50 µm. A

collimated beam of xenon gas is injected into the trap with an injection pressure of approximately $10^{-8}$ mbar. The trap depth, the potential of the central drift tube in relation to neighbouring tubes, was set to 45 V.

Figure 41(a) shows the two dimensional spectrum of the *KLL* DR resonances recorded while performing scans over the Xe *KLL* DR energy region. The *KLL* DR resonances of highly charged xenon ions at an X-ray energy of 31 keV are located on a diagonal line, nearly invisible in the spectrum, which is due to non resonant *L* shell RR. Figure 41(b) shows a projection of the X-ray events with an X-ray energy in the DR range on the electron beam energy axis. The DR resonances are clearly visible on top of a non resonant RR background. A resolution of the electron beam energy of approximately 17 eV at 21.075 keV was achieved. To identify the DR resonances, FAC calculations were carried out. Figure 41(c) shows the calculated spectrum. As in the experiment with krypton ions, only the calculated electron energies of the resonances were used to locate the DR resonances of interest. The two well resolved resonances, $He_1$ and $C_1$ at 20.244 keV and 21.728 keV, respectively, were used to calibrate the electron beam energy.

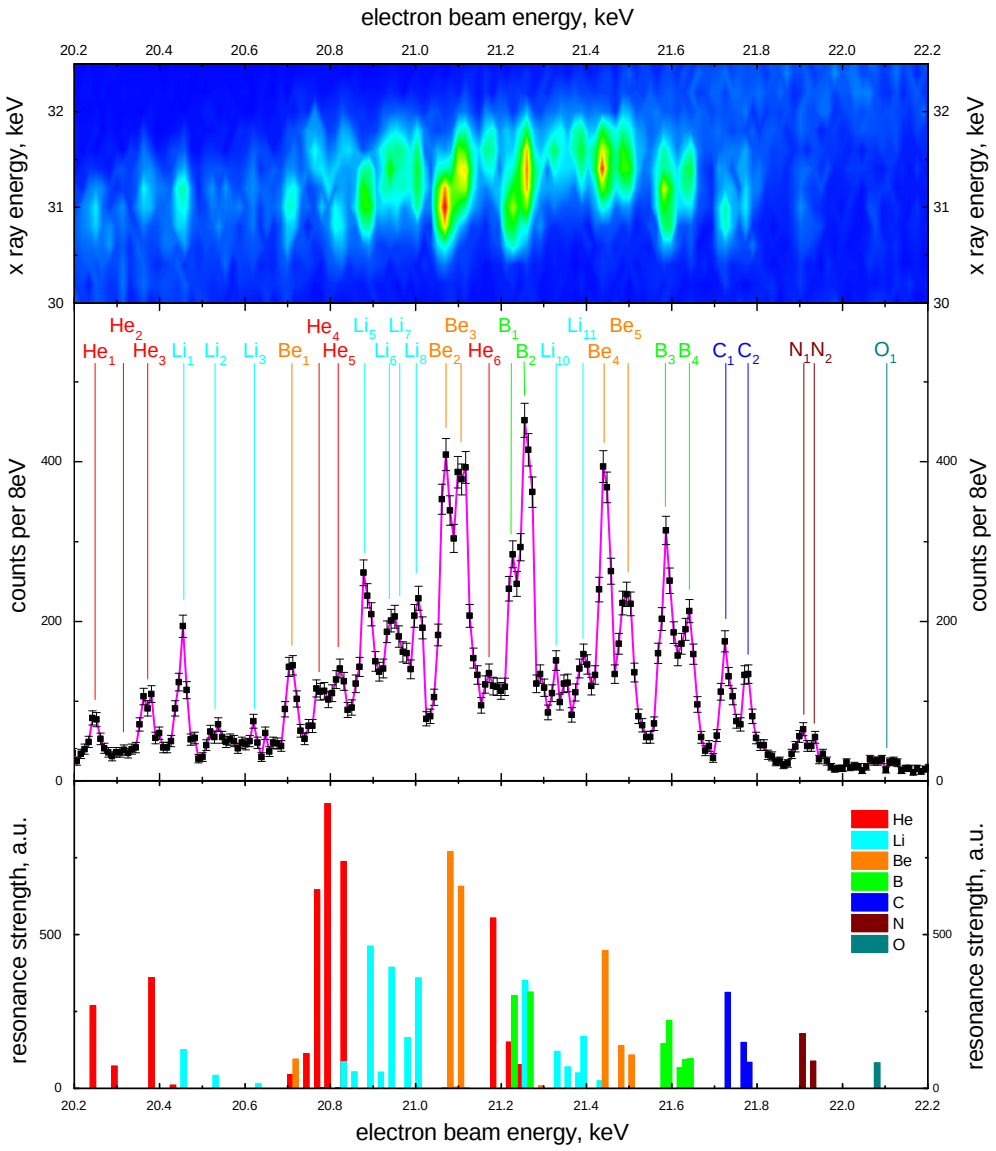


Figure 41: (a) Intensity plot of X-ray events measured while perfoming scans with the electron beam energy. (b) Projection of the X-ray events with an X-ray energy in the *KLL* DR range on the electron beam energy axis. The resonances are identified with the help of FAC calculations, depicted in (c).

X-ray energy spectra were recorded by using the germanium detector while simultaneously scanning the electron beam energy through the region of the *KLL* DR resonances. Figure 42 shows energy spectra recorded by using the germanium detector for the electron beam energy ranges of the $Be_2/Be_3$ and $Li_1$ resonances. The energy resolution was 640 eV FWHM at 31 keV. With these spectra, one has to keep in mind that the germanium detector was placed behind the Compton polarimeter. Thus X-rays have to pass the scatterer in the Compton polarimeter before reaching the germanium detector. For lower X-ray energies the cross section

for the photoelectric effect becomes larger, which explains the gradual cut off for lower energies in the spectra. In the spectra there are several pronounced X-rays lines: the *KLL* DR line at 31 keV, which also includes RR into the $L_{12}$ (J=1/2) shell; the RR line for the $L_3$ (J=3/2) orbital at 28.4 keV for the $Li_1$ range and 29.4 keV for the $Be_2/Be_3$ range. As in the experiment with at the FLASH-EBIT with krypton, the contributions both due RR to the *KLL* DR X-ray line cannot be resolved with the polarimeter and had to be deduced.

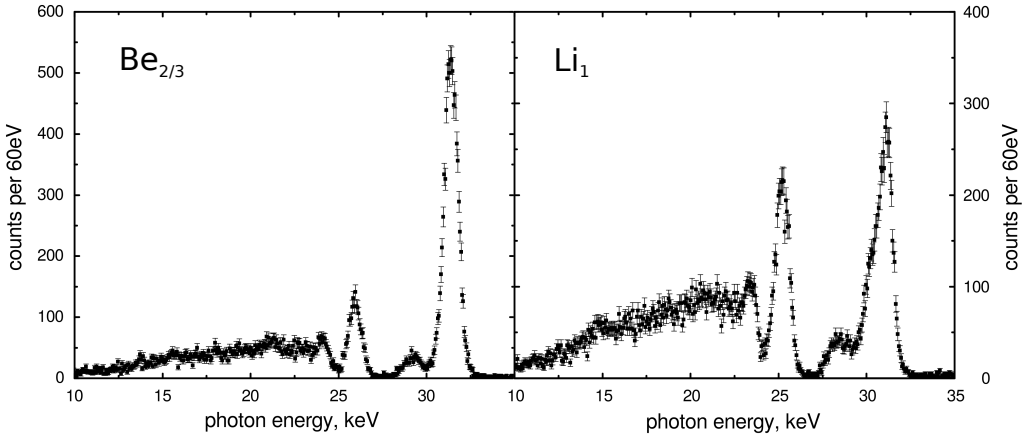


Figure 42: X-ray energy spectra in the germanium detector with the electron beam energy in the region of the $Be_2/Be_3$ region (left figure) and in the region of the $Li_1$ region.

### 5.1.2 Deducing the Radiative Recombination Background

The RR background contribution to the *KLL* DR peaks was deduced from the measured energy spectra, see figure 43 and 44, which are projections of the X-ray events in the energy region of DR on the electron beam energy axis. As in the experiment with krypton ions, the resonances of interest, and their neighbouring lines, were fitted using Gaussian profiles, while the RR background was fitted by a first order polynominal. The RR contributions $f_{RR}$ to the DR peaks, with $f_{DR} + f_{RR} = 1$, are:

| Intermediate State | $f_{RR}$ |
|---|---|
| $Be_2$ | 0.24 |
| $Be_3$ | 0.20 |
| $Li_1$ | 0.20 |

Table 8: Contribution of RR X-rays, $f_{RR}$, to the DR X-ray lines.

FAC calculations were carried out to deduce the degree of linear polarisation of the RR background X-rays, which was found to be $P_{RR}$=0.50±0.15.

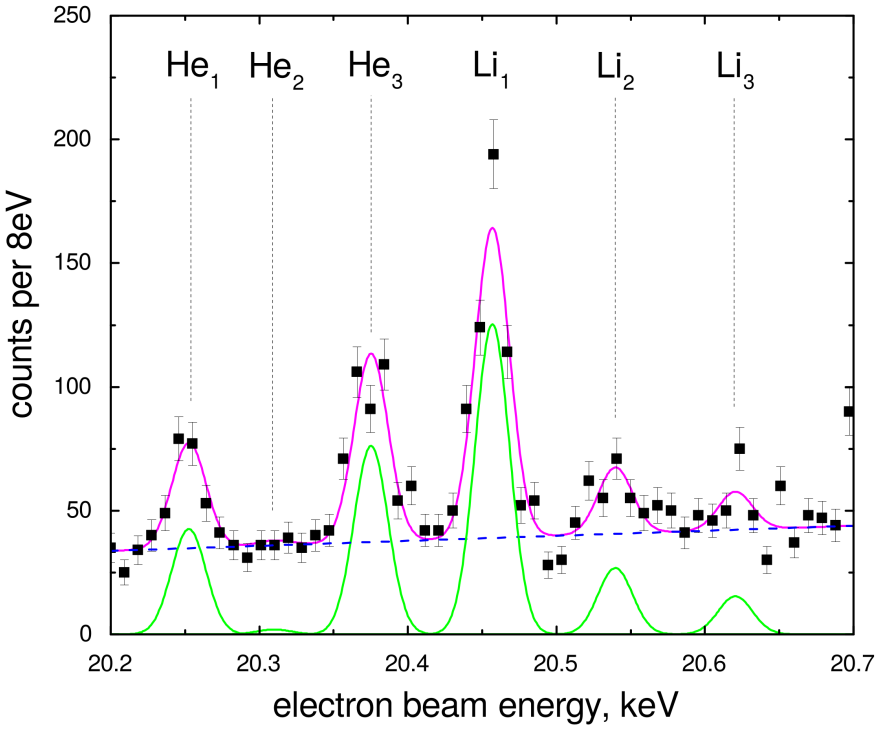


Figure 43: Projection of the X-ray events with an X-ray energy in the *KLL* DR range on the electron beam energy axis for electron beam energies in the region around the $Li_1$ resonances. The magenta line is the fit of the intensity function. Lines corresponding to different DR resonances are in green and the background due to RR is the blue dotted line.

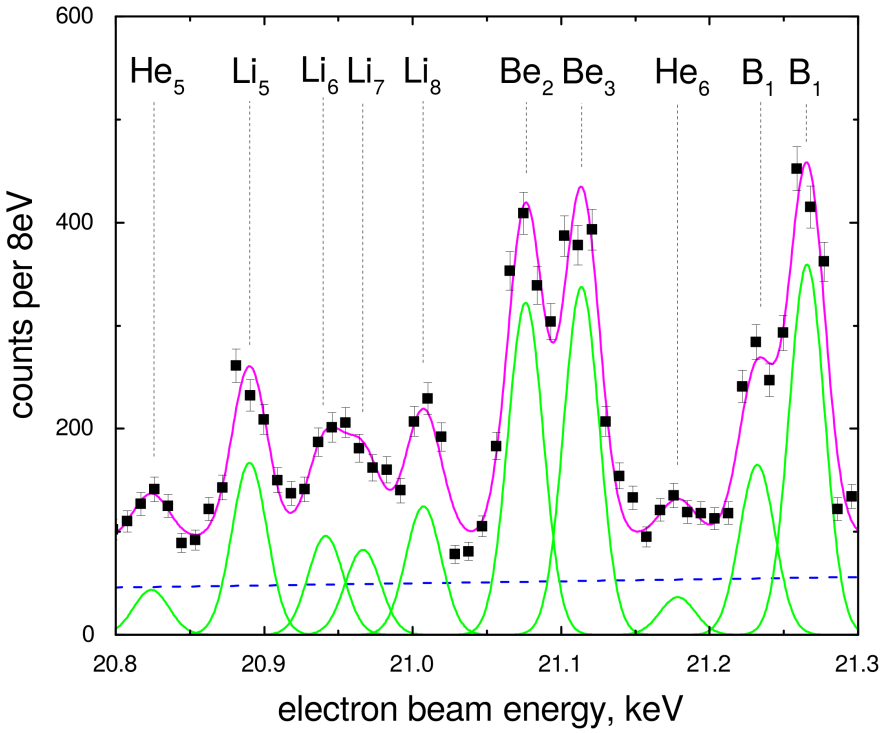


Figure 44: Same as figure 43 except for electron beam energies around the $Be_2$ and $Be_3$ resonances.

### 5.1.3 Polarimetry

Energy spectra in the twelve channels of the polarimeter were now recorded with the electron beam energy tuned into the *KLL* DR resonances of interest. The HD-EBIT has to be refilled with liquid helium every week. For this all EBIT operations have to be shut down. After each shut down, the DR resonances had to be identified again.

Figure 45 shows a typical energy spectrum in one of the polarimeter channels. The peak at 31 keV encompasses *KLL* DR X-rays and RR into the *L* shell. The broad X-ray continuum below 27 keV encompasses impurity lines and bremsstrahlung. For the beryllium-like resonances, the energy resolution was 3.5 keV FWHM and, for the $Li_1$ resonance, it was 2.5 keV FWHM. Between the measurements of the beryllium-like and lithium-like resonances, the data acquisition system was changed. The peak at 31 keV was fitted with a Gaussian profile and the background with a second order polynominal.

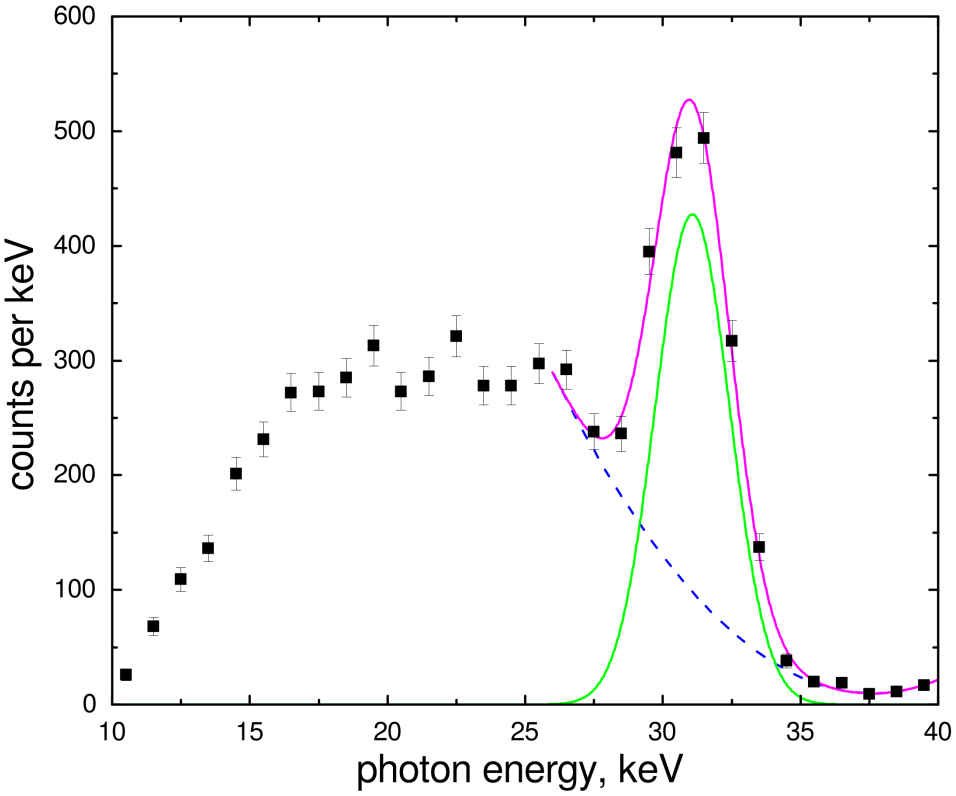


Figure 45: Energy spectrum of scattered X-rays in a SiPIN polarimeter chip with the electron beam energy tuned into the $Be_2$ *KLL* DR resonance of highly charged xenon. A gaussian function, the green line, is used to fit the DR X-ray line. A first order polynominal, the blue dashed line, is used to approximate the background.

Figure 46 shows the energy spectra with the most statistics for each of the measured *KLL* DR lines. The same amount of statistics for each of the resonances was accumulated, which will lead to similar errors for the measured degrees of linear polarisation. The $Li_1$ resonance is weaker than the beryllium-like ones and therefore more time was spent measuring it, which leads to a bigger accumulation of events in the X-ray continuum.

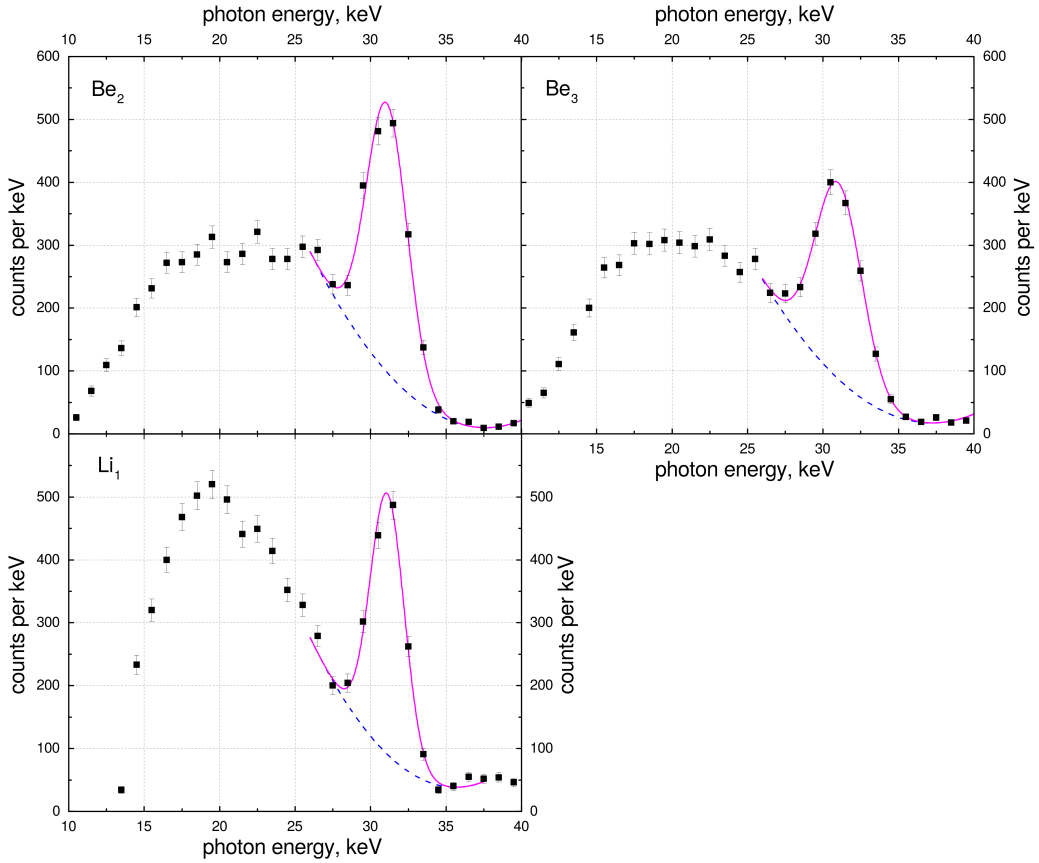


Figure 46: Energy spectra of scattered X-rays in the SiPIN polarimeter chip with the most statistics for each of the measured *KLL* DR lines of highly charged krypton. The fitted line shapes are in magenta, the fitted background is the blue dashed line.

Figures 47 and 48 show the energy spectra in each of the twelve polarimeter channels for the $Be_2$ resonance. The figures show the accumulated DR, and RR, events for different azimuthal scattering angles. The energy spectra for all polarimeter channels are fitted with Gaussian profiles to deduce the scattering intensity, i.e. the area under the Gaussian profile. This procedure is repeated for all DR resonances of interest. Figure 49 shows the intensity modulation, i.e the area under the Gaussian as a function of the azimuthal scattering angle, for each of the three resonances.

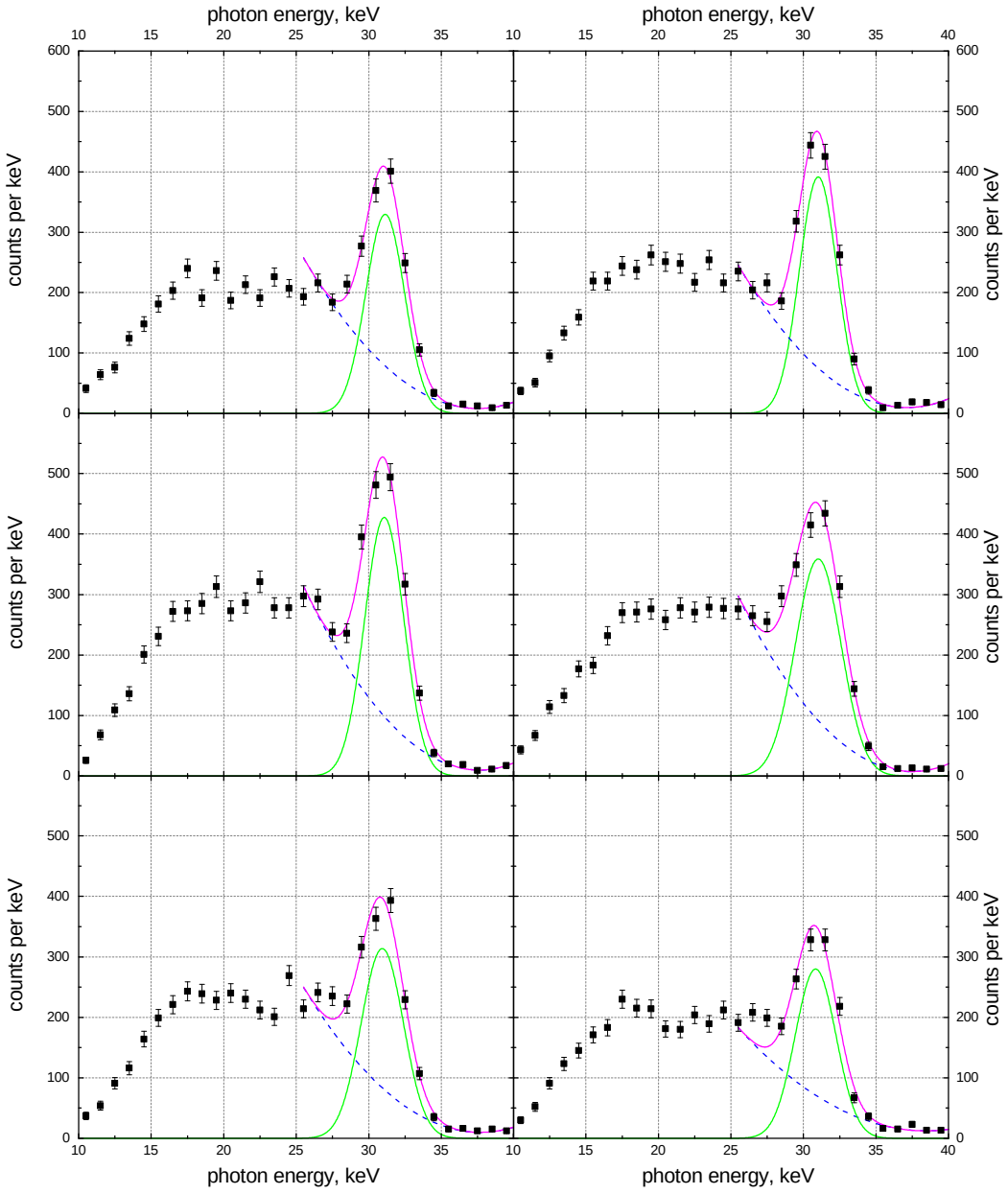


Figure 47: Energy spectrum of scattered X-rays in the first six SiPIN polarimeter chips with the electron beam energy tuned into the $Be_2$ *KLL* DR resonance of highly charged xenon ions. The fitted line shapes are in magenta, the fitted background is the blue dashed line.

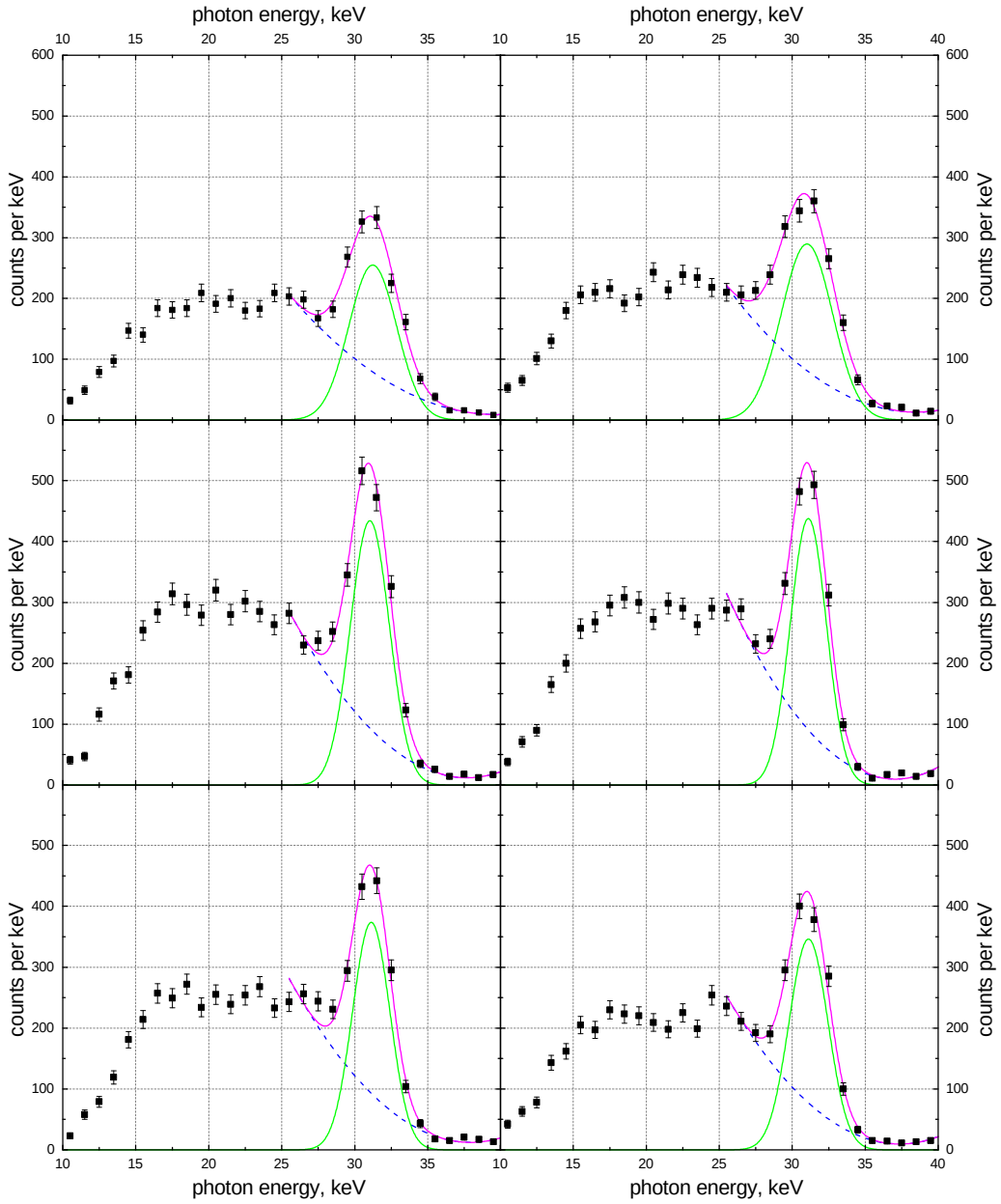


Figure 48: Same as figure 47 except for channel seven to twelve.

## 5.2 Results

Plotting the azimuthal angular scattering intensity modulations for all measured resonances yields figure 49. As in the experiment with krypton ions, the modulation for the $Be_2$ and $Be_3$ lines indicate a positive degree of linear polarisation while, for the $Li_1$ line, the modulation indicates a negative degree of linear polarisation.

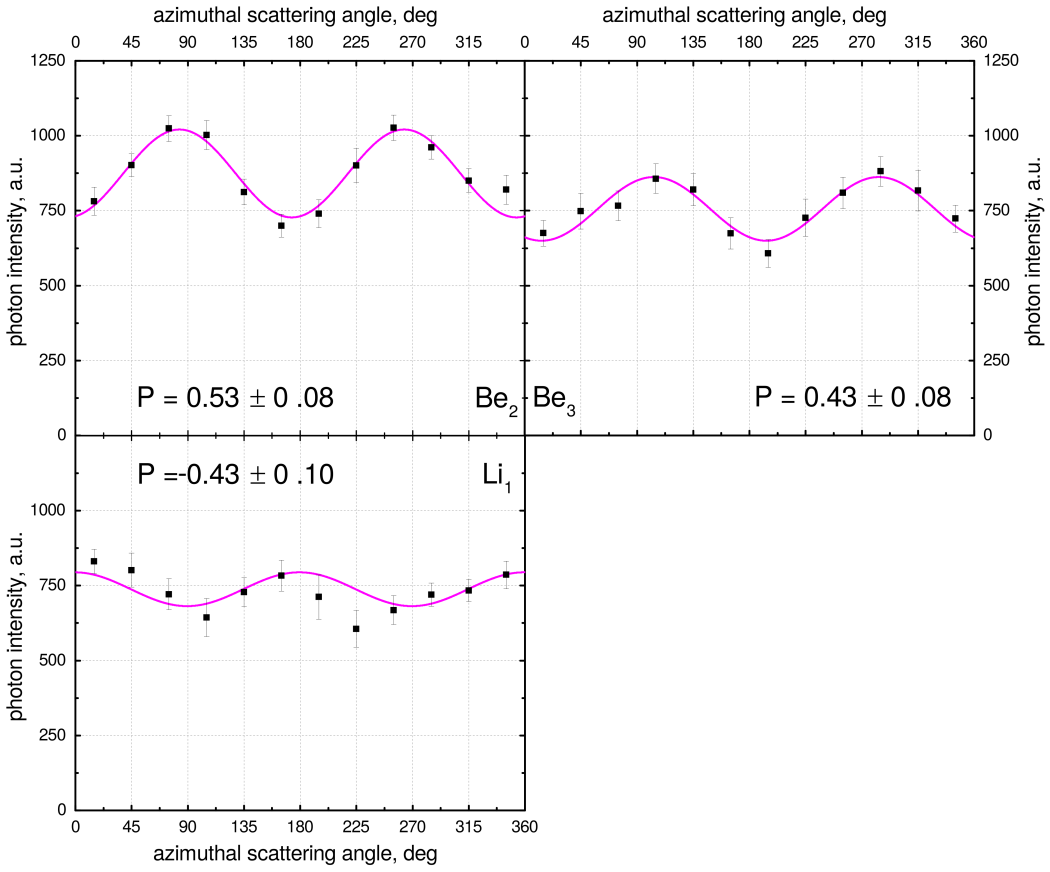


Figure 49: Measured azimuthal angular scattering distributions of X-rays due to *KLL* dielectronic recombination into highly charged xenon ions for different DR resonances. For information on the notation used, see table7.

The scattering distributions are fitted with the Klein-Nishina formula. An explanation on how to account for background X-rays due to RR in the fit has been given in chapter 4.2. The fits yield the following values for the degrees of linear polarisation.

| Intermediate State | $P_{L,\,exp}$ | $P_{L,\,theo\ (C+B)}$ | $P_{L,\,theo\ (C)}$ |
|---|---|---|---|
| $Be_2$: $[(1s2s^22p_{1/2})_1 2p_{3/2}]_{5/2}$ | 0.53±0.08 | 0.50 | 0.50 |
| $Be_3$: $[(1s2s^22p_{1/2})_0 2p_{3/2}]_{3/2}$ | 0.43±0.08 | 0.40 | 0.40 |
| $Li_1$: $[1s2s^22p_{1/2}]_1$ | -0.43±0.10 | -0.44 | -0.95 |

Table 9: Polarimeter results for the degree of linear polarisation for *KLL* dielectronic recombination lines for highly charged xenon ions, denoted by their intermediate charge state. Measured degree of linear polarisation $P_{L,\,exp}$, in comparison with the theoretical calculations taking only Coulomb interaction into account $P_{L,\,theo\ (C)}$ and also accounting for Breit interaction $P_{L,\,theo\ (C+B)}$.

## 5.3 Conclusion: Influence of Breit Interaction on the Polarisation of the $Li_1$ Resonance

Theory calculations with two different codes were carried out: FAC and RATIP [37]. Both agree in respect to the predicted degrees of linear polarisation with and without including Breit interaction. There has already been a discussion about how the polarisation of *KLL* DR lines depends on the alignment of the intermediate doubly-excited state and the partial electronic capture cross sections into magnetic sublevels $\sigma_{m_d}$ in the case of *KLL* DR into highly charged krypton ions 4.2. The same conclusions for the population of magnetic sublevels can be drawn here. In the case of the beryllium-like resonances, the measured values for the degree of linear polarisation agree well with the theoretical values.

For the $Li_1$ resonance, measuring the degree of linear polarisation for a heavier ion, xenon in comparison to krypton, results in a bigger influence of relativistic contributions, like Breit interaction. In this case, the experimental value of $P_{L,\,exp}$ =-0.43±0.10 agrees well with the calculations taking Coulomb as well as Breit interaction into account, $P_{L,\,theo\,(C+B)}$ =-0.44, while it rules out by 5σ calculations only taking the Coulomb interaction into account, which yields $P_{L,\,theo\,(C)}$ =-0.95. In terms of the population probabilities of magnetic sublevels, for an ion as heavy as xenon, the experimental value clearly proves a population probability of the magnetic sublevel with $|m_d|$ =0, which is forbidden in the non-relativistic limit [24].

Figure 50 shows the present status of research on the influence Breit interaction has on the polarisation of the specific DR line $Li_1$. The experiments conducted so far clearly establish that especially for heavier ion species Breit interaction dominates Coulomb interaction for this resonance. Distinguishing the influence the generalised Breit interaction has, which takes into account the frequency of the photon mediating the electron-electron interaction, see equation (23), from the "classical" Breit interaction requires an improvement for the resolution for polarisation measurements in the order of one magnitude for X-ray energies in the region from 10 keV to 35 keV or performing polarisation measurements with heavier ion species.

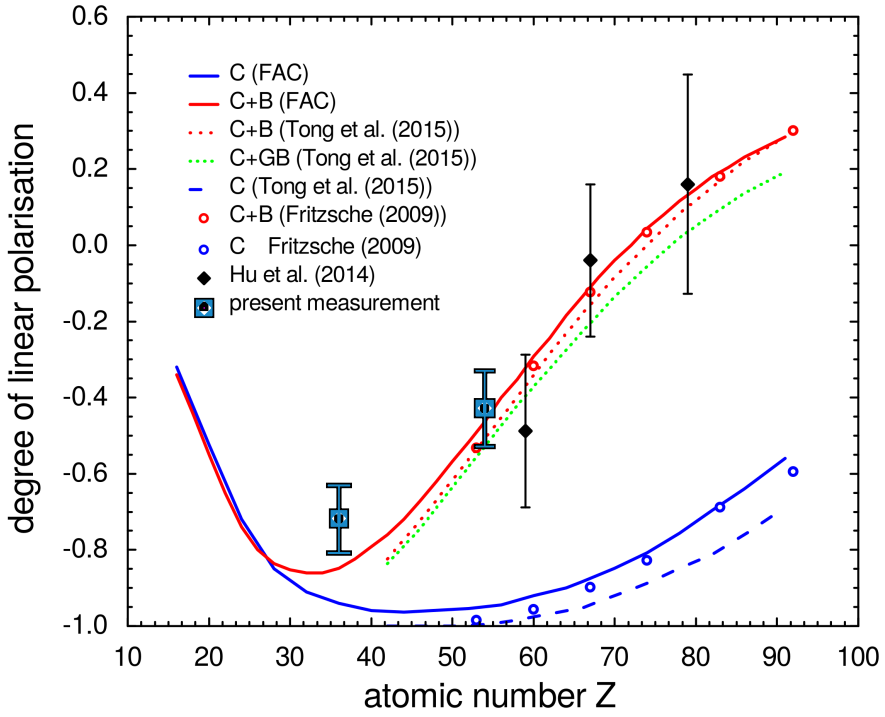


Figure 50: Present status of - theoretical and experimental - research on the influence Breit interaction has on the polarisation of the $Li_1$ resonance in *KLL* DR into highly charged ions. Theory calculations have been carried out by Tong et al [7], Fritzsche [6] and by us (FAC); they include only Coulomb interaction (C), as well as Breit interaction (B) and generalised Breit interaction (GB). Experimental results include an EBIT experiment by Hu et al. [35] and our results [24].

# 6 Silicon Drift Detector Compton Polarimeter

A Silicon Drift Detector (SDD) based Compton polarimeter, see picture in figure 51, was developed for X-ray polarimetry experiments with high energy resolution in the energy region from 6 keV to 35 keV [3]. It was built for polarisation measurements at synchrotrons, where single transitions of HCIs can be photo-excited by synchrotron radiation. For Compton scattered X-rays with an energy of 13 keV, its energy resolution is 600 eV FWHM. The SDD polarimeter was tested in the course of polarisation measurements with an EBIT at the Max Planck Institut für Kernphysik in Heidelberg and at the high-brilliance synchrotron radiation source Petra III at DESY, Hamburg.

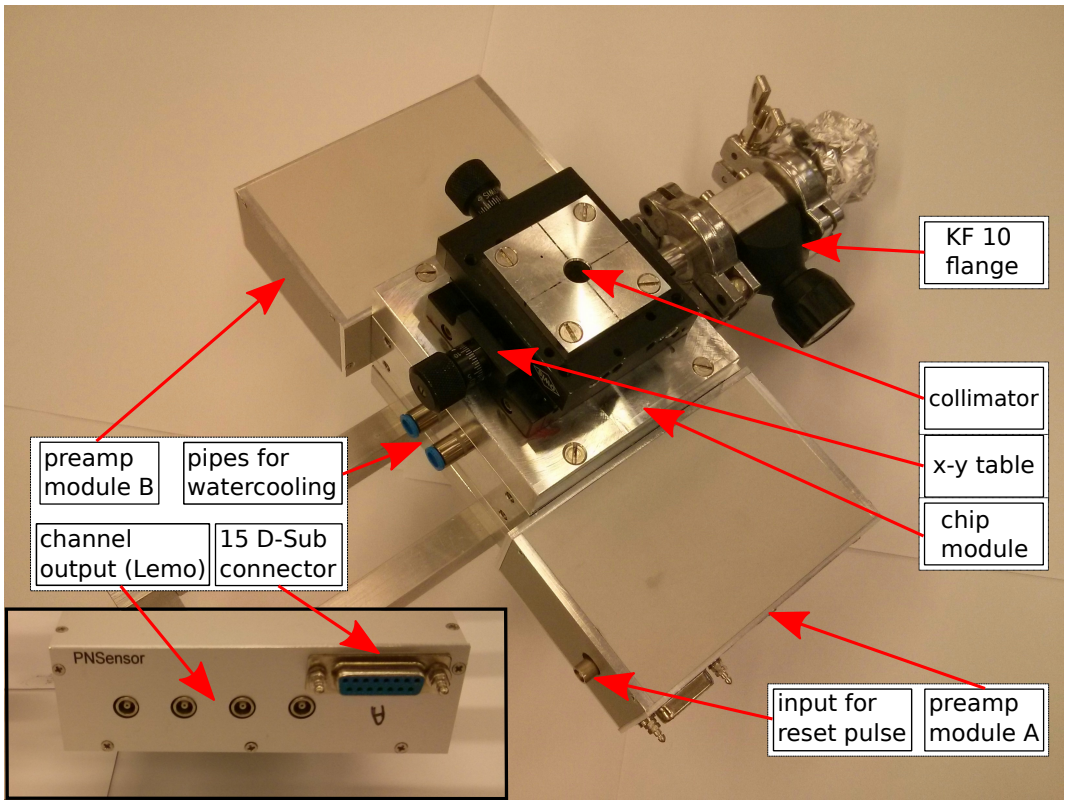


Figure 51: Silicon Drift Detector (SDD) Compton polarimeter. The chip module hosts the eight SDD chips. The preamp modules, one on each side of the chip module, host the SDD chip electronics for four SDD chips each. The collimator hole has a diameter of 9 mm.

[3] in collaboration with the company "pn-sensor" at Munich, where it was built

## 6.1 Principle Of Operation

The SDD polarimeter design is based on the sensitivity of the angular distribution of Compton scattered X-rays to their degree of linear polarisation, as with the previous polarimeter generation based on SiPIN diodes, see chapter 3.2. The polarimeter setup, see figure 51, consists of a chip module, which hosts the eight detector chips, and two preamplifier modules, which house most of the SDD chip electronics. Furthermore it consists of an aluminium collimator and a 15 mm thick beryllium scatterer. X-rays enter the polarimeter through a beryllium window on its frontside, after passing the collimator, which is mounted on an xy-table, where the z-direction is defined by the beam of the incoming X-rays. The X-rays pass through the chip module and leave the module through the beryllium window on its backside. There they are scattered in the beryllium scatterer. Backscattered X-rays re-enter the chip module. Their azimuthal angular scattering distribution is sampled at a polar scattering angle of $\theta = 150°$ by an array of the eight circularly arranged SDD chips.

The SDD chips are located in a dewar, which is evacuated via a KF 10 flange. A Pirani sensor measures the pressure within the chip module. The SDD chips are cooled with Peltier elements, which can be water-cooled via two pipes. On both sides of the chip module there are beryllium windows. The preamplifier modules enclose two four-channel preamplifiers each. The connectors on each preamplifier module are: four Lemo connectors for the channel output, one Lemo connector for the reset pulse and a 15-Pin D-Sub, which is used for the low-voltage supply of the preamplifiers, the HV supply of the SDDs, the output of the temperature diode and the output of the pressure sensor.

### 6.1.1 Silicon Drift Detector Chips

The high X-ray energy resolution of SDDs compared to other semiconductor detectors becomes possible by implementing a new depletion scheme, i.e. sideways depletion, of the silicon wafer. This new depletion scheme was first implemented by E. Gatti and P. Rehak in 1984 [80]. An SDD chip, see figure 52, has two pn-junctions, or more specifically a pnp-junction, in reverse bias as its central element. Sideways depletion of the junction leads to an anode capacitance independent of the active area of the detector, which in turn leads to a low leakage current and thus low noise. This makes thermoelectric cooling of the chips by Peltier elements to further reduce noise possible. Further noise reduction is achieved by on-chip signal amplification by a junction gate field effect transistor (JFET).

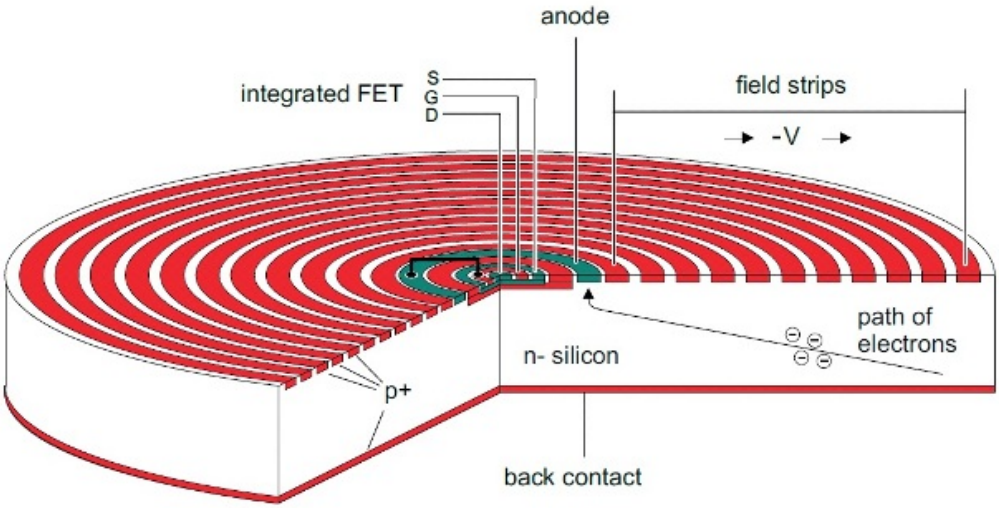


Figure 52: Silicon Dirft Detector (SDD) chip consisting of an $n^-$-type silicon wafer with $p^+$-type contacts attached to its front- and backside. The $p^+$-contacts on the frontside consist of a strip array, which provides the drift field. There is a $n^+$-type anode on its frontside as well as a junction gate field effect transistor (JFET). [81]

SDD chips consist of a fully depleted $n^-$-type silicon wafer, which is completely depleted through a virtual anode, a small ohmic $n^+$-contact, attached on one side, see upper left side of figure 53. The anode is positively biased with respect to $p^+$-contacts covering both faces of the silicon wafer. Thus the pn-junctions are biased in reverse. The capacitance-voltage characteristic between the $p^+$-contacts and the $n^+$-type anode depends on the applied voltage, see lower left side of figure 53. As this voltage comes close to the total depletion voltage, the conductive channel retracts and the conductance drops rapidly. For a fully depleted disc, the conductance only weakly depends on the applied voltage. The anode capacitance does not depend on the area of the disc.

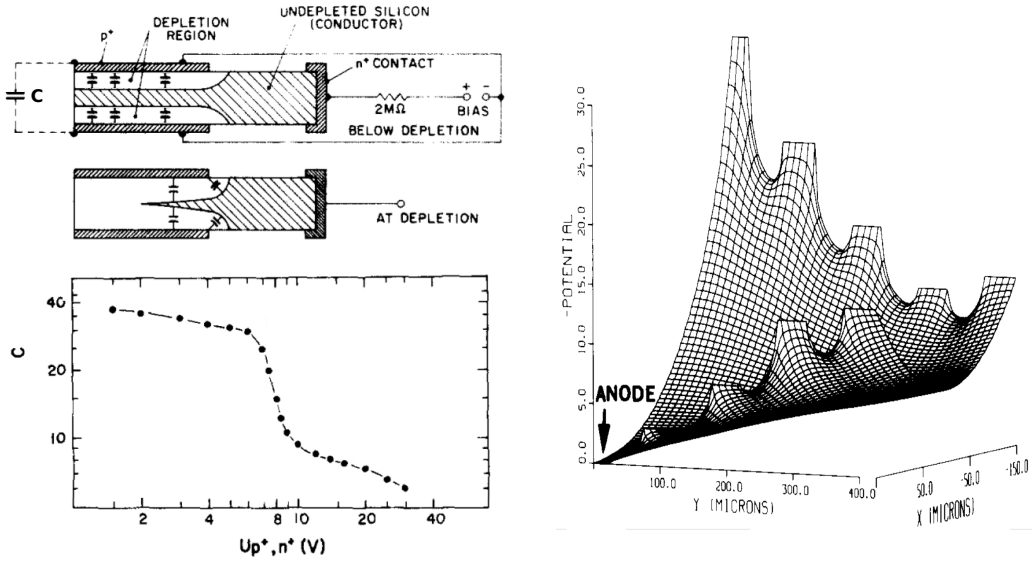


Figure 53: (left side) Illustration of the sideways depletion scheme of a disc-shaped $n^-$-type silicon wafer. A small $n^+$-type silicon anode is attached to the side of the disc, while $p^+$-type silicon contacts are attached to the faces of the discs. The capacitance between the $p^+$-type contacts and the $n^+$-type anode decreases as a function of the applied depletion voltage. (right side) Drift field, i.e. gutter potential, for the electron drift toward the anode. Adapted from [80]

The sideways depletion scheme leaves the option to apply an additional field, independent from the depletion field, for charge transport. With only the depletion field the potential for electrons has a minimum on half of the height of the silicon disc. In the absorption of ionising radiation by the depleted silicon wafer, electron-hole pairs are created. With the application of an additional electric field with a component perpendicular to the surface of the disc, the electrons perform a drift towards the anode, see right side of figure 53. The implementation of such a drift field is achieved by attaching a strip array of $p^+$-contacts, as drift electrodes, on the frontside of the $n^-$-type wafer, see figure 52. The strips of $p^+$n-junctions provide both the depletion and the drift field. Here, the single $p^+$-contact on the backside of the wafer is put on a lower potential than the contacts on its frontside. To create a drift field, a linear potential is applied to the stripes of the $p^+$n-junctions with the anode on the highest potential. In sum, this yields a 2D gutter potential for electrons, see right side of figure 53.

On-chip amplification in combination with a sideways depleted silicon chip with its low-capacitance anode, yields a total detector capacitance of $\simeq 50$ pF. The distance between signal creation, through absorption of an ionising particle, and signal amplification is at a minimum. Microphony effects are, as a result, also at a minimum. This makes low-noise operation and thus a high energy resolution possible.

On-chip amplification is realised by putting JFETs on the chips. Electrons, which are created when ionising radiation impinges on the wafer, drift towards the anode and induce a negative voltage there. This voltage is directly coupled to the gate of the JFET, which is a $p^+$-semiconductor. The negative voltage reversely biases the junction by depleting the transistor channel, an n-type semiconductor. The current drop through source and drain can be measured [78].

### 6.1.2 Detector Supply

In order to operate the SDD polarimeter, the following external devices are necessary.

- Vacuum pump to evacuate the SDD chip module to a pressure of below 0.2 mbar
- Peltier power supply (0.35 A / 4 V) for the cooling of the SDD chips to -20° C
- Low voltage power supply (+12/-24 V; max 100mA) for the preamplifier boards
- High voltage power supply (-180 V; max 6 mA) for the depletion of the SDDs
- Pulse generator (TTL; f $\simeq$ 1 kHz; $T_p \simeq$ 400 ns) for the reset pulse for the SDDs
- Digital pulse processor for DAQ

The Peltier power supply, as well as the low-voltage power supply for the preamplifier boards are housed in a NIM module, which was designed in our group. Its specification are discussed in chapters 6.1.2 and 6.1.2. For the evacuation of the SDD chip module, a scroll pump was used, and for the digital pulse processing, the same modules as for the experiments with the SiPIN based polarimeter was used, see chapter 3.2.2.

#### Vaccuum Supply and Peltier Cooling

The SDD chips are cooled down to a temperature of -20° C to achieve a low leakage current and thus a good energy resolution. As water and ice would damage the chips, the detector module is evacuated to a vacuum of below 0.2 mbar in order to prevent water vapour from condensating and building up ice on the SDDs. The pressure is measured with a Pirani gauge inside the module. The Pirani output

voltage is in the range from 1.0 V (>1 mbar) to 1.36 V (<$10^{-4}$ mbar). At a voltage of 1.2 V, the pressure inside the chip module is at 0.2 mbar.

The cooling is done by two Peltier elements, one for four detector chips each. In order to cool them down to -20°C, a voltage of about 4 V with a current of about 0.35 A has to be applied to the Peltier elements. This is managed with the circuit depicted in figure 54. To control the current through P+ and P- and to keep it below 0.1 A on startup, a series of potentiometers and resistances is used. A low-pass filter keeps high frequency noise from the Peltier elements. The voltage and the current through the Peltier cooler is monitored by volt- and amperemeters. The temperature of one chip on each side is monitored by a temperature diode, whose output voltage is monitored with a voltage change of 0.03 V per degree Celsius temperature change.

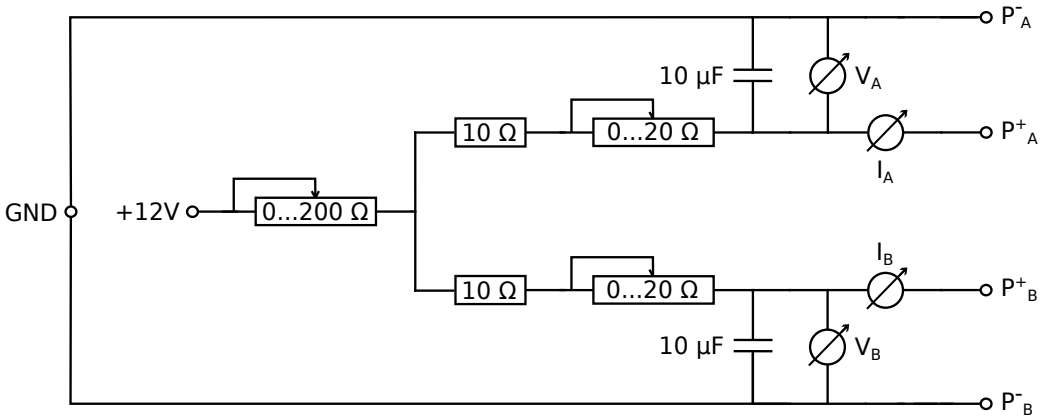


Figure 54: Power supply for the two Peltier coolers inside the the chip module. A 200 Ω potentiometer is used to limit the Peltier current on startup below 0.1 A. With a resistor of 10 Ω and a potentiometer of 20 Ω for each side, the desired voltage drop and current through the Peltier elements is adjusted.

### Low Voltage Preamplifier Power Supply

The preamplifier boards are supplied with +12 V and -24 V with a maximum current of 100 mA via the circuit depicted in Fig. 55. The preamplifier boards not only supply the preamplifiers but also bias the Pirani sensor and the temperature diode. To minimize high-frequency noise, the supply circuit consists of two low-pass filters.

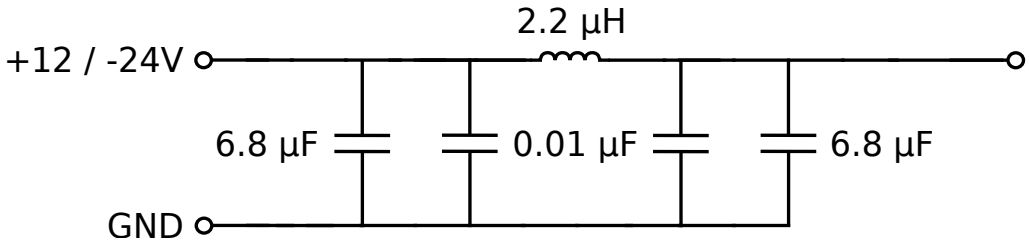


Figure 55: Low-pass filters for the preamplifier board power supply.

### 6.1.3 Polarimeter Simulation

A Geant4 [4] Monte Carlo simulation was used to derive the modulation factor, see chapter 3.2.3, of the SDD polarimeter. The detector geometry in the simulation is a simplified version of the real polarimeter. It consists of an aluminium collimator, the beryllium scatterer and the silicon detector chips. A beam of 100% linearly polarised X-rays with an energy of 13 keV per photon is generated and collimated towards the scatterer, see figure 56. The dominant scattering processes in this energy range were included in the Geant4 physics list: Compton and Rayleigh scattering. The scattering distribution is sampled by the detector chips.

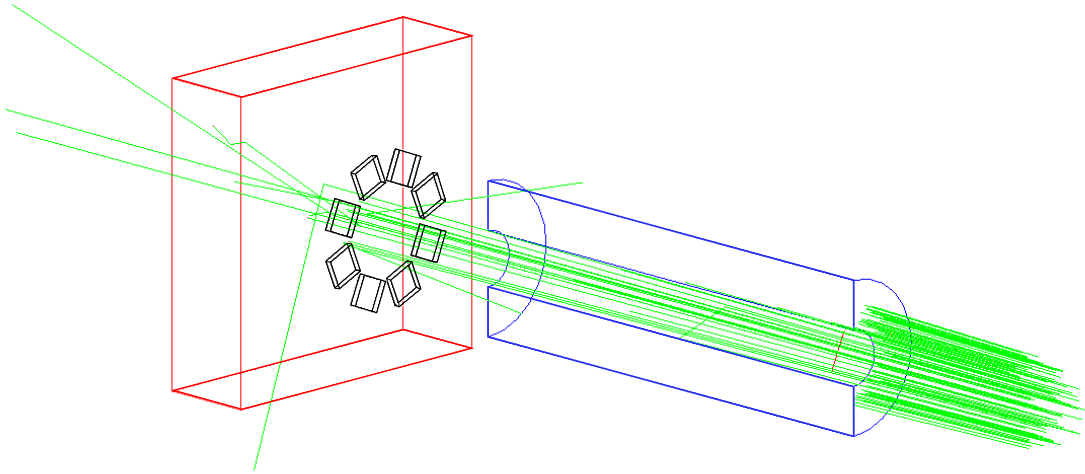

Figure 56: Simulated X-ray events in the SDD based polarimeter. Events are simulated in the Geant4 framework. 100% linearly polarised X-rays with 13 keV per photon, shown in green, are generated and collimated by the blue collimator, towards the scatterer, shown in red. The scattered X-rays are detected by twelve SDD chips, depicted in black.

[4] https://geant4.web.cern.ch/geant4/

In each of the eight simulated detector chips, energy spectra of the scattered X-rays were recorded, see figure 57. The peak at 13 keV corresponds to Rayleigh scattered X-rays. The energy deposition of the X-ray in the scatterer is negligible in Rayleigh scattering for this energy range. The broader peak at 12.4 keV corresponds to the Compton peak of Compton scattered X-rays. The lines shapes are discussed in chapter 6.2. Plotting the number of Compton scattered X-ray events as a function of the azimuthal angle of the particular chips yields the azimuthal angular scattering distribution, see figure 58. This distribution was fitted with the Klein-Nishina formula and a value of M = 0.29 was obtained for the modulation factor.

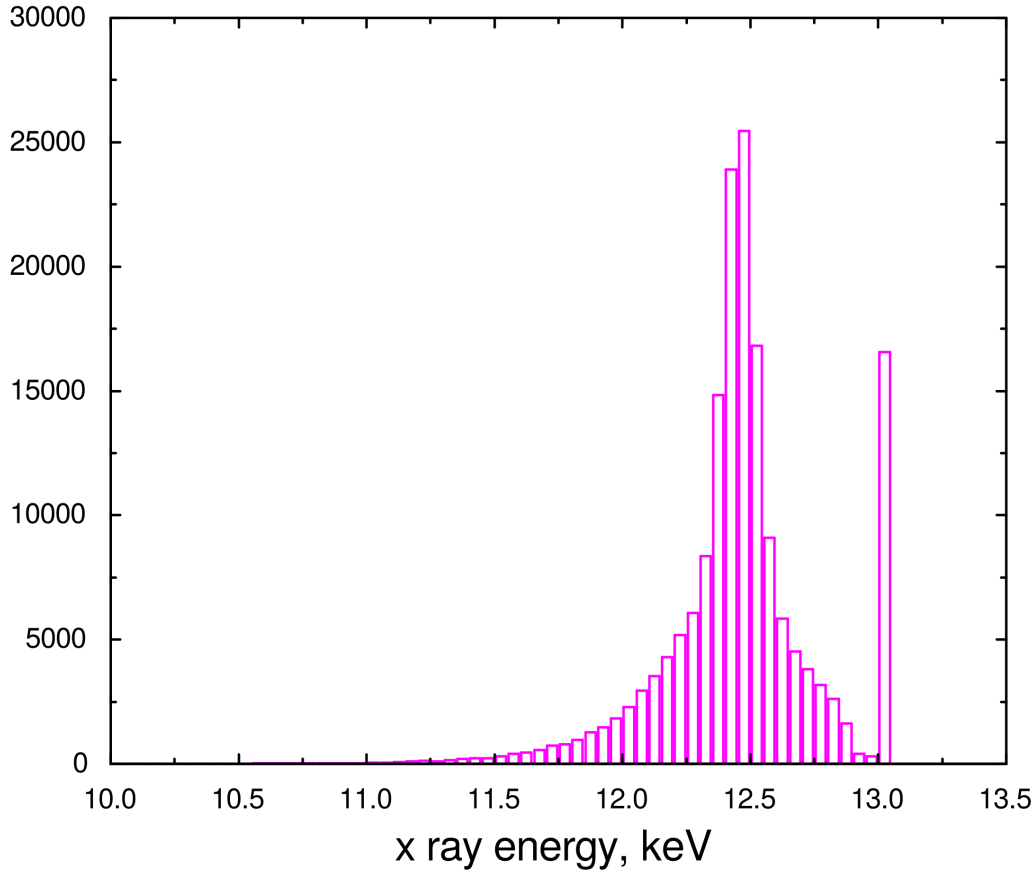


Figure 57: Geant4 simulation of scattered X-rays in the SDD polarimeter. The figure shows the energy spectrum of X-rays with 13 keV which are Compton and Rayleigh scattered in beryllium. The peak at 13 keV corresponds to Rayleigh scattered X-rays, while the peak at 12.4 keV corresponds to Compton scattered X-rays.

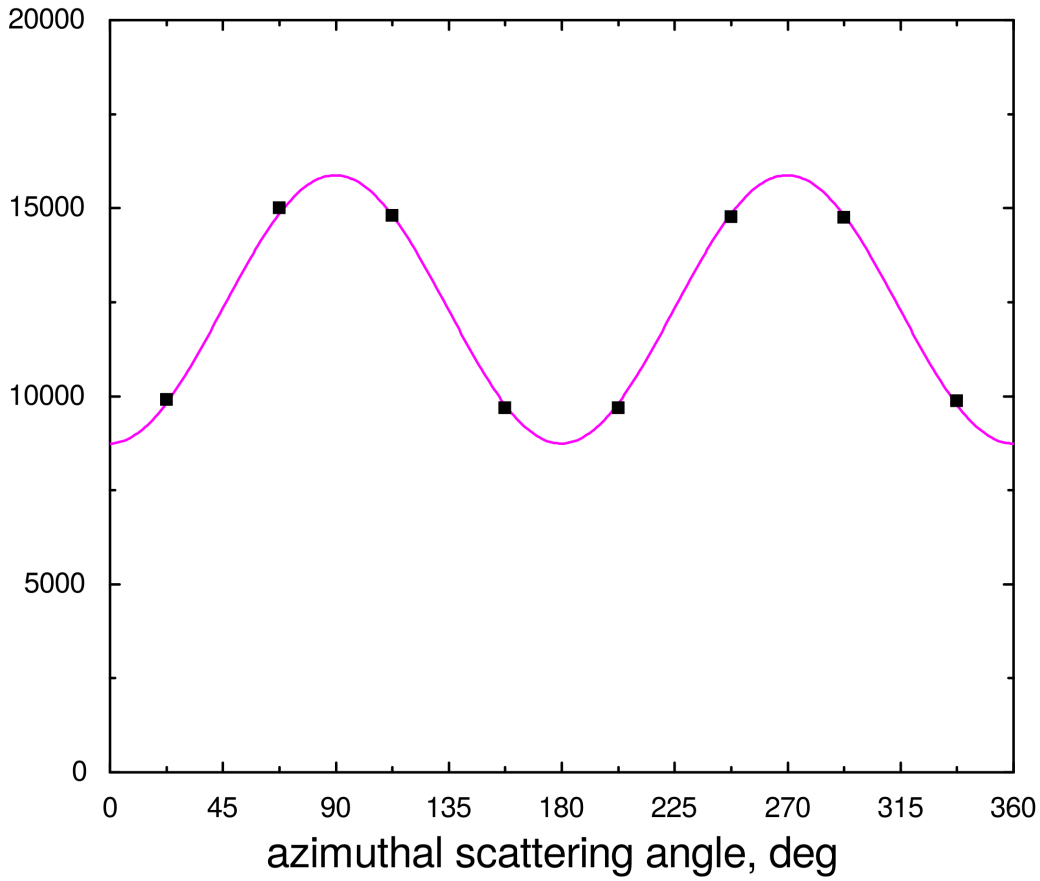


Figure 58: Geant4 simulation of scattered X-rays in the SDD polarimeter. The figure shows the azimuthal angular scattering distribution of Compton scattered X-rays at 12.4 keV. The distribution is fitted with the Klein-Nishina formula, see chapter 2.2.2.

To characterise the performance of the SDD polarimeter for different X-ray energies in the region from 6 keV to 30 keV, further simulations have been conducted. The figure of merit $F = \epsilon M^2$ is used to characterise the polarisation sensitivity [77]. Here, the efficiency $\epsilon$ is defined as the product of the Compton scattering efficiency of X-rays of a given energy in the solid angle covered by the SDD chips and the quantum efficiency of the SDDs for this energy. The scattering efficiency and the modulation factor are derived by a Geant4 simulation, while the quantum efficiency of the SDDs was supplied by their manufacturer. Figure 59 shows the results of the simulation. The limiting factor for polarisation measurements with the SDD polarimeter is its efficiency. For X-rays with energies above 30 keV, the SDDs become more and more transparent. For energies below 6 keV, the Compton scattering cross section becomes too small, see figures 8 and 9. The polarimeter shows its best performance at X-ray energies of 13 keV.

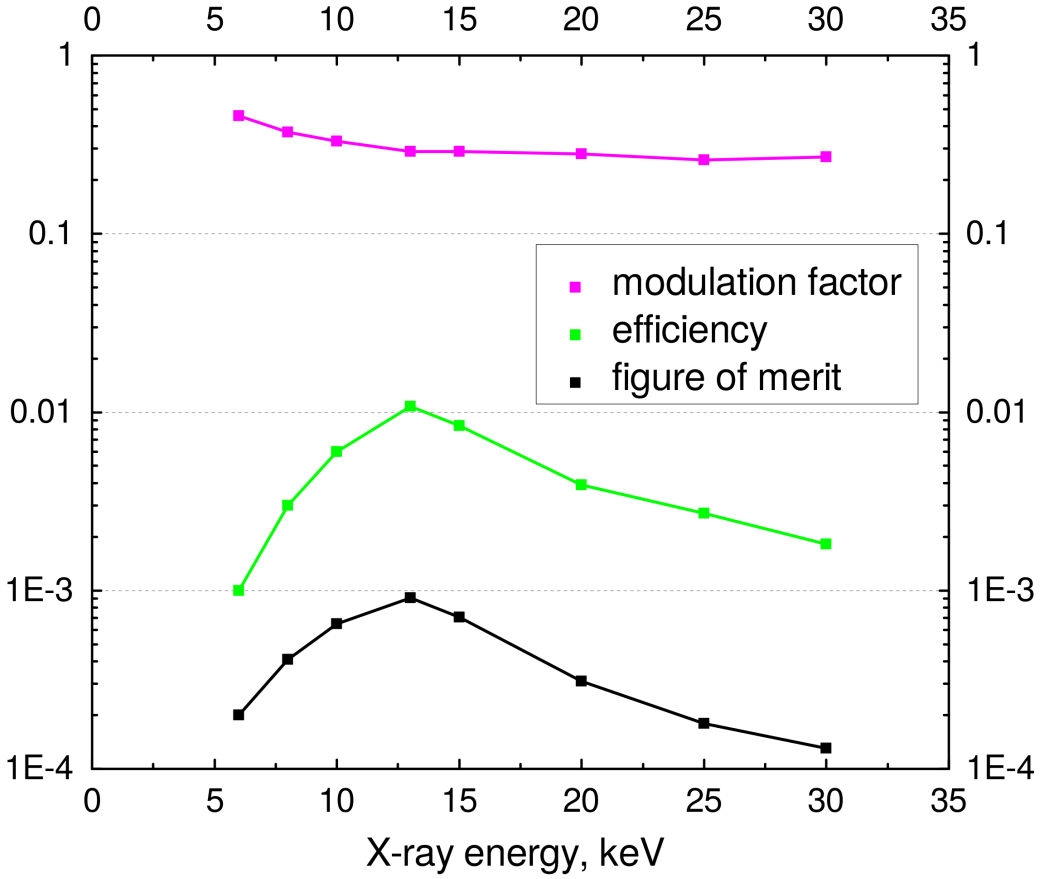


Figure 59: Modulation factor M, efficiency $\epsilon$ and figure of merit F of the SDD polarimeter.

### 6.1.4 Characterisation of the SDD Chips with an $^{241}$Am and $^{55}$Fe Source

The energy resolution of the SDD detector chips was determined using two radioactive sources, $^{55}$Fe and $^{241}$Am. With the sources in front of the chips, the following energy spectra, shown in figure 60 and 61, were recorded. Only the spectrum for one channel for each source is shown. For the $^{55}$Fe source, the FWHM of the peak at 5.9 keV, due to $K\alpha$ X-rays, was deduced through fitting the peak with a Gaussian profile. For the $^{241}$Am source, the FWHM of the peak at 13.9 keV, which is caused by $L\alpha$ X-rays, and of the strong 60 keV gamma line was deduced by fitting the peaks with Gaussian profiles. The measured energy resolutions are listed in table 10.

| Channel | 1 | 2 | 3 | 4 | 5 | 6 | 7 | 8 |
|---|---|---|---|---|---|---|---|---|
| FWHM [eV] @ 5.9 keV | 180 | 183 | 183 | 188 | 188 | 183 | 180 | 190 |
| FWHM [eV] @ 13.9 keV | 265 | 272 | 246 | 251 | 270 | 272 | 274 | 265 |
| FWHM [eV] @ 60 keV | 361 | 427 | 397 | 430 | 434 | 458 | 425 | 434 |

Table 10: Measured energy resolutions of the SDD polarimeter chips at energies of 5.9 keV, 13.9 keV and 60 keV.

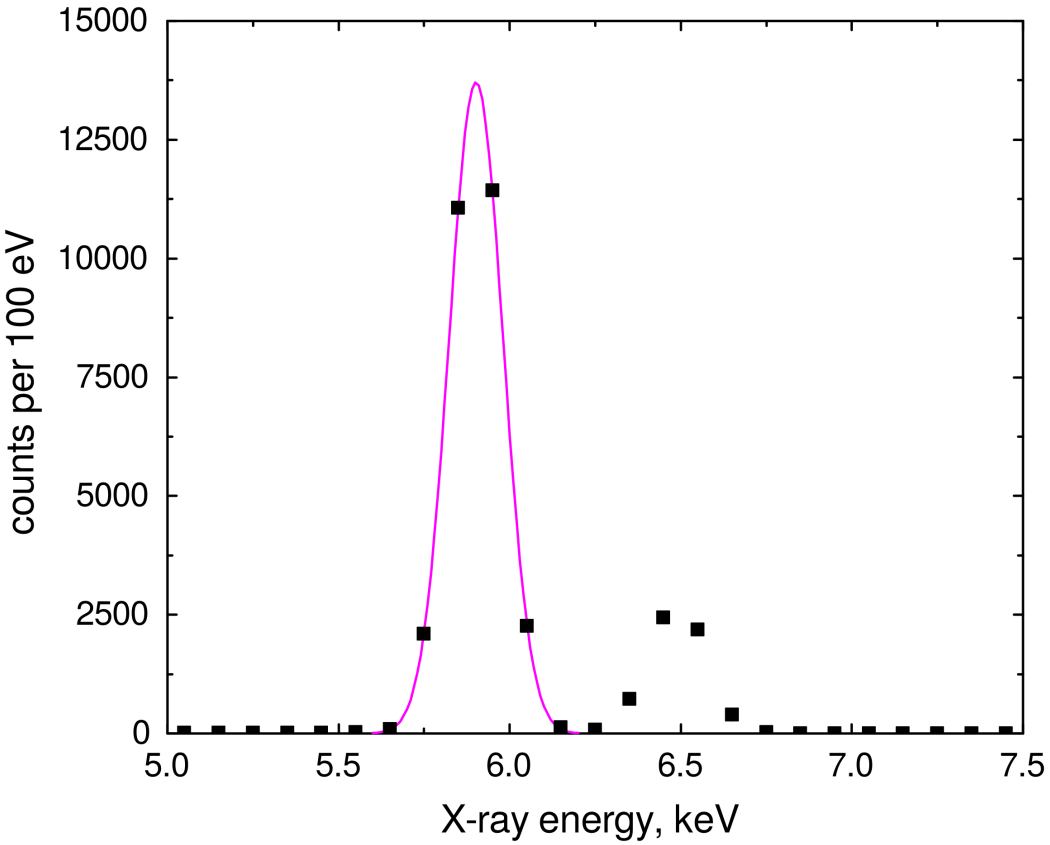


Figure 60: X-ray energy spectrum recorded in channel eight of the SDD polarimeter with an $^{55}$Fe source in front of the SDD chips. The line at 5.9 keV is due to $K\alpha$ X-rays. The line at 6.5 keV is due to $K\beta$ X-rays. The $K\alpha$ peak is fitted with a Gaussian profile, shown in magenta.

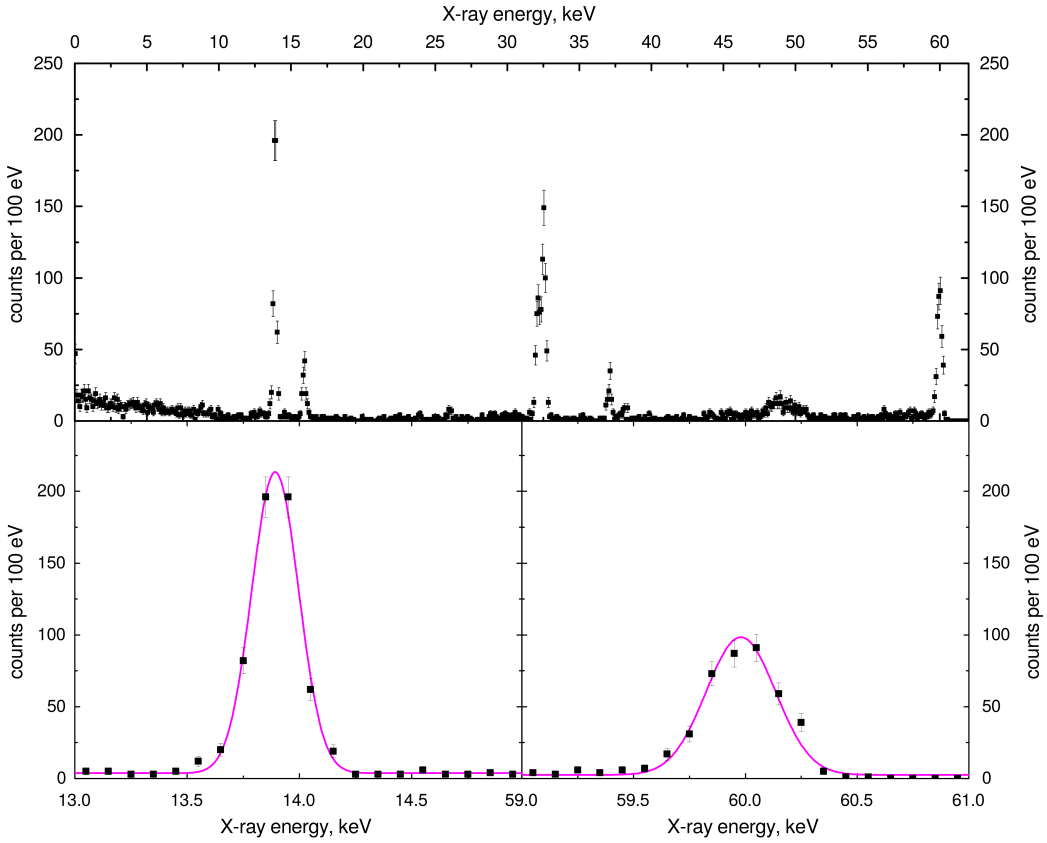


Figure 61: Same as figure 60 except with an $^{241}$Am source. The upper figure shows the whole X-ray spectrum. The lower figures show the line at 13.9 keV, which is due to $L\alpha$ X-rays, and the gamma line at 60 keV, respectively. The 13.9 keV and 60 keV peaks are fitted with Gaussian profiles and a zero order polynominal to approximate the background. The fits are shown in magenta.

## 6.2 Polarisation Measurements of Krypton *KLL* DR at the FLASH-EBIT

In this chapter, a test measurement with the SDD polarimeter at the FLASH-EBIT at the Max Planck Institut für Kernphysik in Heidelberg in March 2016 is presented. The goal of this measurement was to measure the degree of linear polarisation of X-rays emitted by highly charged krypton ions during *KLL* DR. The setup used here was very similar to the ones used for the previous polarisation measurements at the FLASH-EBIT in 2013, see chapter 4, and at the HD-EBIT in 2014, see chapter 5, with the SiPIN polarimeter. The setup consisted of the FLASH-EBIT, the SDD polarimeter and a further semiconductor detector, a one chip SDD, for diagnostic purposes which recorded unscattered X-rays from the trap. There was also a difference in geometry. While in previous measurements the polarimeter was attached to the EBIT side beryllium window, here it was attached to the bottom window. The polarimeter was placed on a plate held by four metal rods with adjustable length. Furthermore incoming X-rays were backscattered towards the SDD chips. In total this yields a more complicated geometry in comparison to the previous experiments at EBITs with the SiPIN polarimeter. As a result of this complicated geometry, the geometrical alignment between X-ray beam from the trap, collimator and scatterer had to be precisely adjusted.

To identify the Kr *KLL* DR resonances at electron beam energies of 8.9 - 9.4 keV, the one chip SDD is used to record energy spectra of X-rays from the trap. The FLASH-EBIT was configured to achieve a resolution of the electron beam energy, which was high enough to resolve the resonances, and maintain a sufficient DR X-ray count rate in the resonance of interest. This was the $Be_1$ resonance with an intermediate state of $[(1s2s^2 2p_{1/2})_1 2p_{3/2}]_{5/2}$ at an electron beam energy of 9175.6 eV. The trap depth was set to 270 V and the beam current was at 200 mA. An FAC calculation yielded a degree of linear polarisation of $P_{L,\,theo} = 0.49$ for the $Be_1$ resonance. This particular resonance was chosen because of its high resonance strength and relatively high degree of polarisation.

Plotting the X-ray energy spectra as a function of the electron beam energy, while performing scans over the Kr *KLL* DR energy region, yields a two dimensional spectrum of the *KLL* DR resonances, see figure 62(a). The horizontal line of bright spots at an X-ray energy of 13 keV are the *KLL* DR resonances of highly charged krypton ions. They are located on a diagonal line, nearly invisible in the spectrum, which is due to non-resonant *L* shell RR. Figure 62(b) shows a projection of the X-ray events with an X-ray energy in the DR range on the electron beam energy

axis. To identify the resonances, this spectrum was compared to FAC calculations. The $Be_1$ and $Be_3$ resonances, at 9.176 keV and 9.239 keV, were used to calibrate the electron beam energies. The resolution for the beam energy was 21 eV at 9.176 keV, which is similar to the resolution achieved in the measurement with the SiPIN polarimeter in 2013, see chapter 4.1.1. In comparison to the measurement in 2013, here, the FLASH-EBIT has been optimised solely for the production of beryllium-like krypton ions. To analyse the polarimeter data, the contribution of RR X-rays from recombination into the $L$ shell to the $Be_1$ $KLL$ DR peak has to be deduced from the spectrum in figure 62(b). The two peaks, $Be_1$ and $Be_2$ were fitted with Gaussian profiles while the background was approximated by a first order polynominal. The fits yield a contribution of RR of the order of 9%, which is similar to the contribution of RR to the DR lines for DR into beryllium-like krypton ions measured during the experiment in 2013, see chapter 4.1.2.

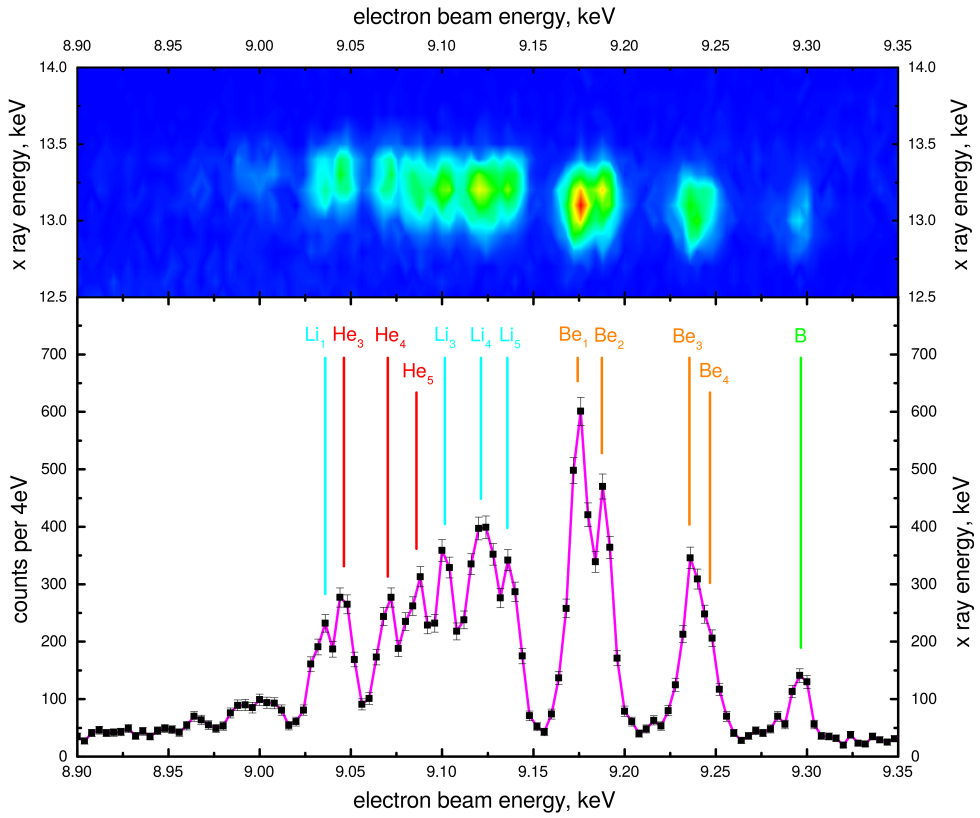


Figure 62: (a) Intensity plot of X-ray events measured while perfoming scans with the electron beam energy. (b) Projection of the X-ray events with an X-ray energy in the $KLL$ DR range on the electron beam energy axis. The resonances are identified with the help of FAC calculations, see figure 31

X-ray spectra were recorded in the one chip SDD detector while the electron beam energy was scanned over the DR resonances. Figure 63 shows such an X-ray spectrum in the one chip SDD detector with the electron beam energy in the region of the $Be_1$ resonance. The peak at 13 keV encompasses the resonance and $L$ shell RR X-rays. The energy resolution was 340 eV FWHM at 13 keV.

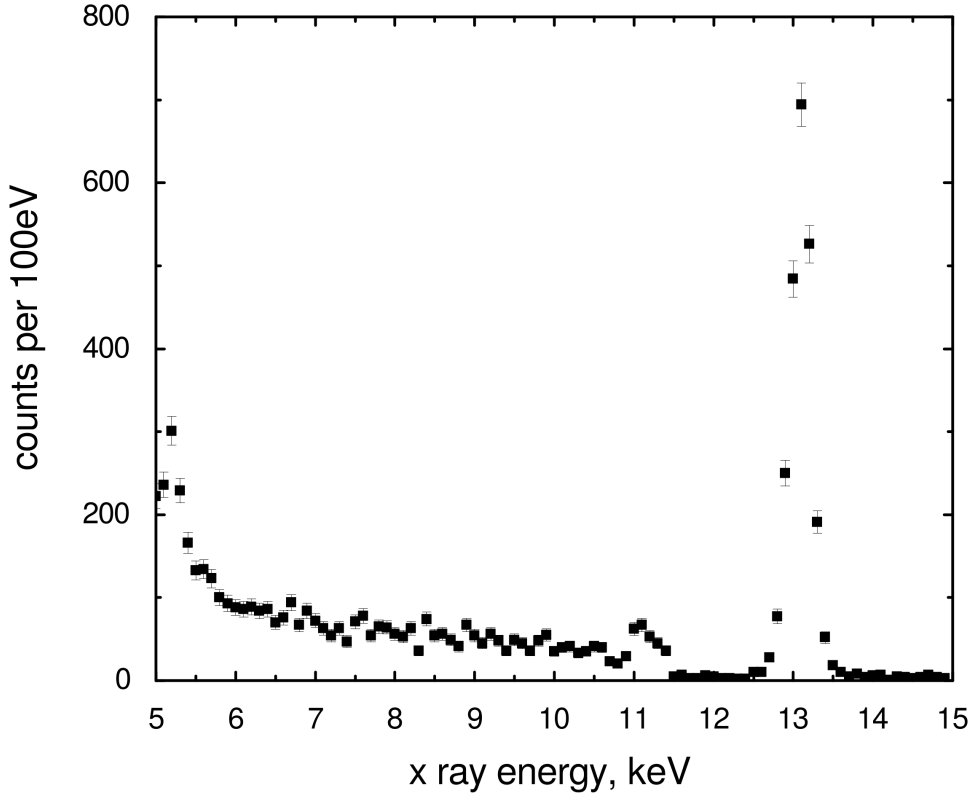


Figure 63: X-ray spectrum in the one chip SDD detector with the electron beam energy tuned into the $Be_1$ resonance. The peak at 13 keV corresponds to $KLL$ DR and $L$ shell RR X-rays.

For polarimetry, the electron beam energy was tuned into the $Be_1$ resonance, while recording energy spectra in the eight polarimeter channels. Figure 64 and figure 64 show such energy spectra. The peak at 12.4 keV corresponds to Compton scattered X-rays with an energy of 13 keV at a scattering angle of 150°. This peak encompasses X-rays due to $KLL$ DR and $L$ shell RR. The peak at 13 keV is due to Rayleigh scattered $KLL$ DR and $L$ shell RR X-rays. Below 10 keV bremsstrahlung dominates the spectrum. For the different channels the energy resolution for the scattered X-rays at 12.4 keV was deduced by fitting the peaks. The results are listed in table 11.

| Channel | 1 | 2 | 3 | 4 | 5 | 6 | 7 | 8 |
|---|---|---|---|---|---|---|---|---|
| FWHM [eV] @ 12.4 keV | 542 | 587 | 594 | 643 | 622 | 601 | 585 | 613 |

Table 11: Energy resolution of the SDD channels for Compton scattered X-rays with 13 keV.

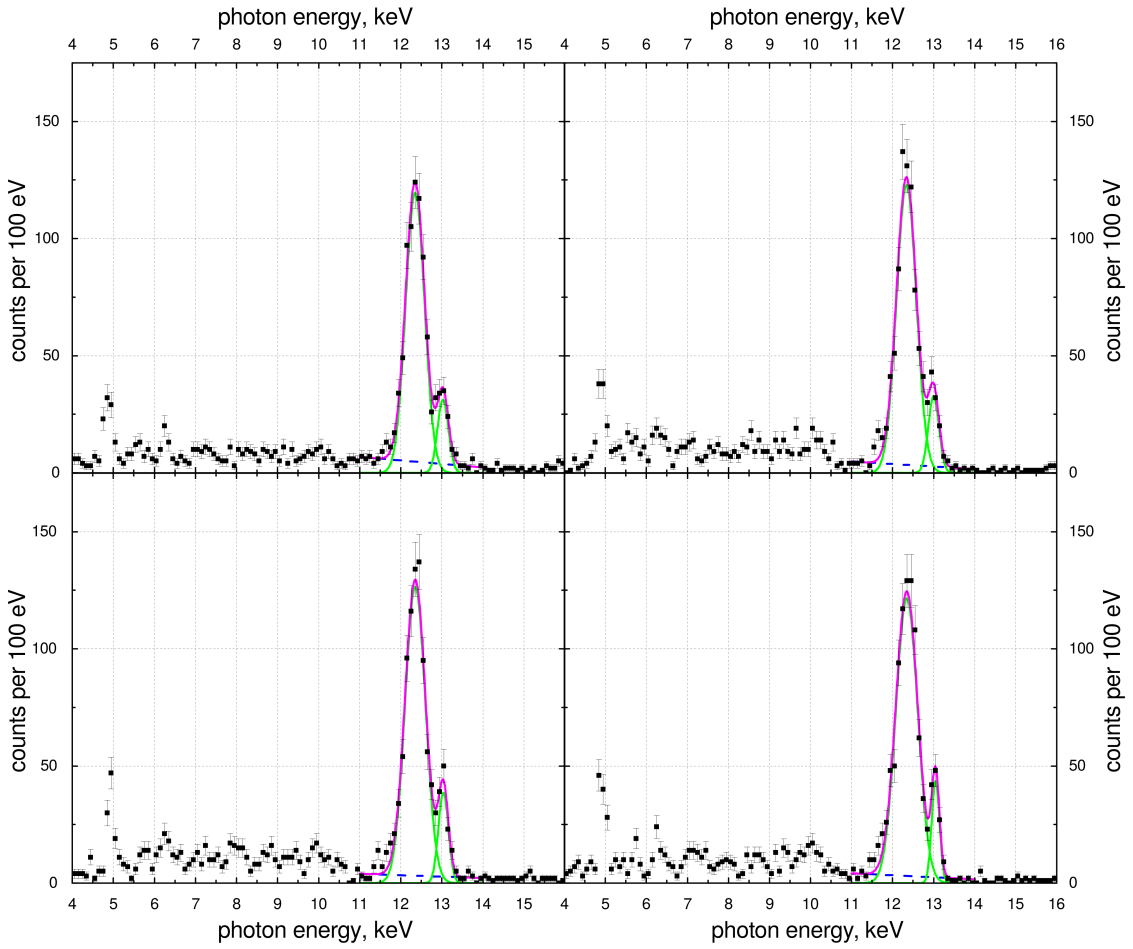


Figure 64: X-ray spectrum observed using the first four SDD polarimeter channels with the electron beam energy tuned into the DR resonance $Be_1$ without a set geometric alignment between collimator and SDD chips. The small peak at 13 keV is due to Rayleigh scattered DR and $L$ shell RR X-rays coming from the EBIT. The peak at 12.4 keV is due to Compton scattered DR and $L$ shell RR X-rays.

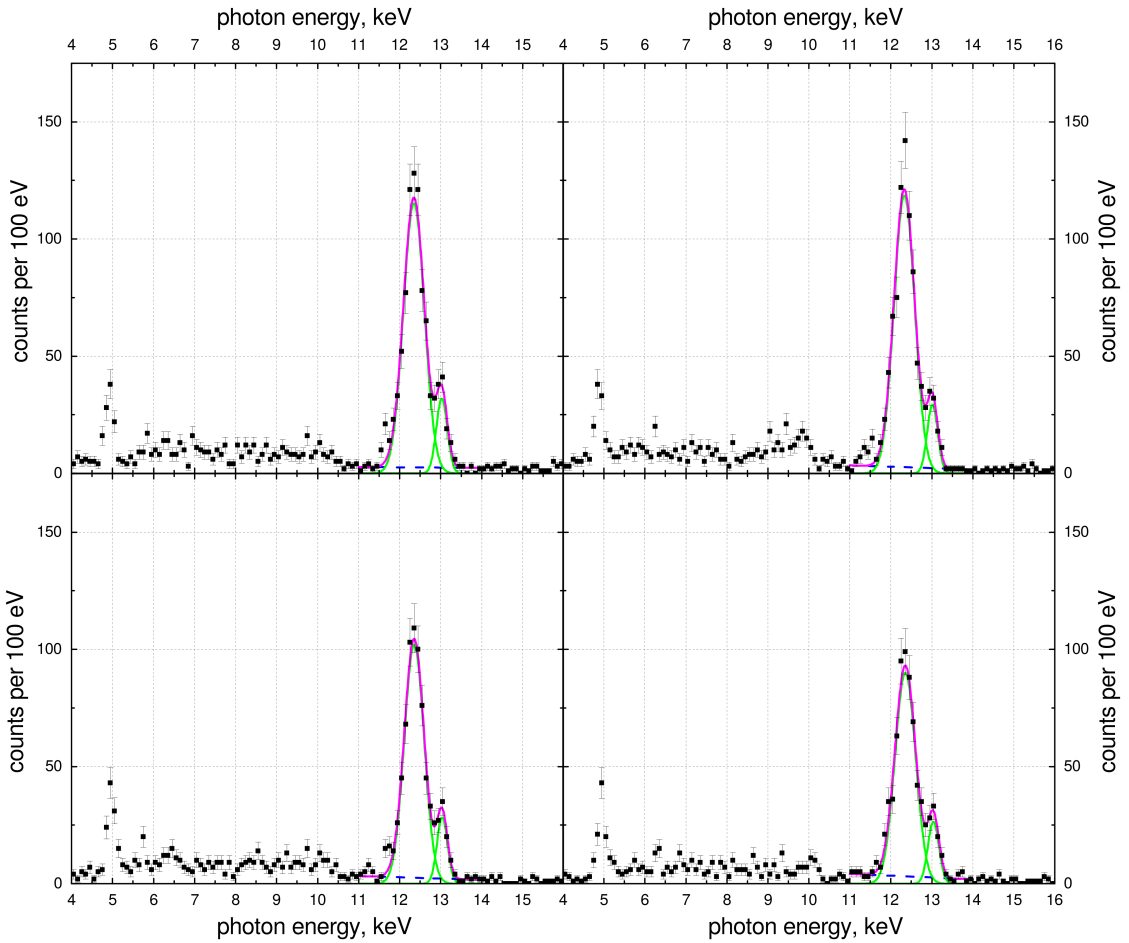


Figure 65: Same as figure 64, except for the second four polarimeter channels

Figure 66 shows a comparison of the energy spectra of Compton and Rayleigh scattered X-rays with 13 keV derived with the Geant4 simulation, see chapter 6.1.2, and measured using the forth SDD polarimeter channel. The ratio of Compton to Rayleigh scattered X-rays, which is approximately nine to one, is the same for the both spectra. X-rays with an energy of 13 keV do not lose any energy in Rayleigh scattering. From fitting the peak due to Rayleigh scattered X-rays, the energy resolution of the SDD channels can be derived, which is approximately 300 eV FWHM. The energy of Compton scattered X-rays depends on their polar scattering angle $\theta$. The SDD chips cover a range of polar scattering angles around $\theta = 150\,°$. With the infinitesimally small energy resolution of the detector chips in the Geant4 simulation, this results in line shape which resembles a Voigt profile. In a single Compton scattering process, X-rays with an energy of 13 keV cannot lose more energy than 700 eV, which corresponds to $\theta = 180\,°$. X-ray events with an energy of less than 12.3 keV are due to multiple scatterings in the beryllium scatterer. In the measurement, the finite energy resolution of the chips smears out this profile.

The resultant line shape can be approximated by a Gaussian profile.

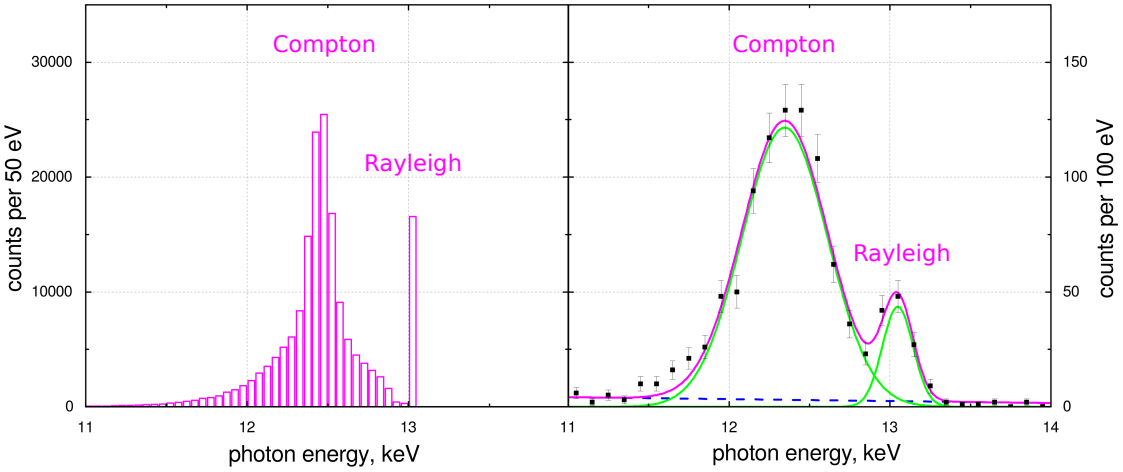


Figure 66: Comparison of the energy spectra of scattered X-rays with 13 keV derived with a Geant4 simulation (left side) and measured using the forth SDD polarimeter channel (right side).

The X-rays coming from the ion trap have to be collimated exactly to the geometric center of the chips on the scatterer. If this geometric alignment is off center, the azimuthal angular scattering distribution does not show a dipole structure even if linearly polarised X-rays are Compton scattered. Therefore, the collimator is fixed on a µm-xy-table to set this geometric alignment between collimator and chips. In comparison to the forward scattering geometry of the SiPIN polarimeter, the SDD polarimeter uses a more complicated backscattering geometry, which makes setting the geometric alignment more difficult. Figure 64 and figure 64 show energy spectra recorded while setting the geometric alignment.

Figure 67 and figure 68 show energy spectra recorded with the final geometric alignment. The accumulated statistics represents two full days of measurements. It is enough to resolve the peak due to Rayleigh scattered X-rays from the peak due to Compton scattered X-rays. The statistics accumulated are not sufficient to perform fits of the peak due to Compton scattering. The Compton scattering intensity at a given angle, i.e. in a given chip, was derived by summing over the X-ray events in the peak. Figure 69 shows the azimuthal angular scattering distribution of X-rays due to the *KLL* DR $Be_1$ resonance in highly charged krypton ions. The intensity modulation is fit with the Klein-Nishina formula to deduce the degree of linear polarisation of the *KLL* DR $Be_1$ X-rays.

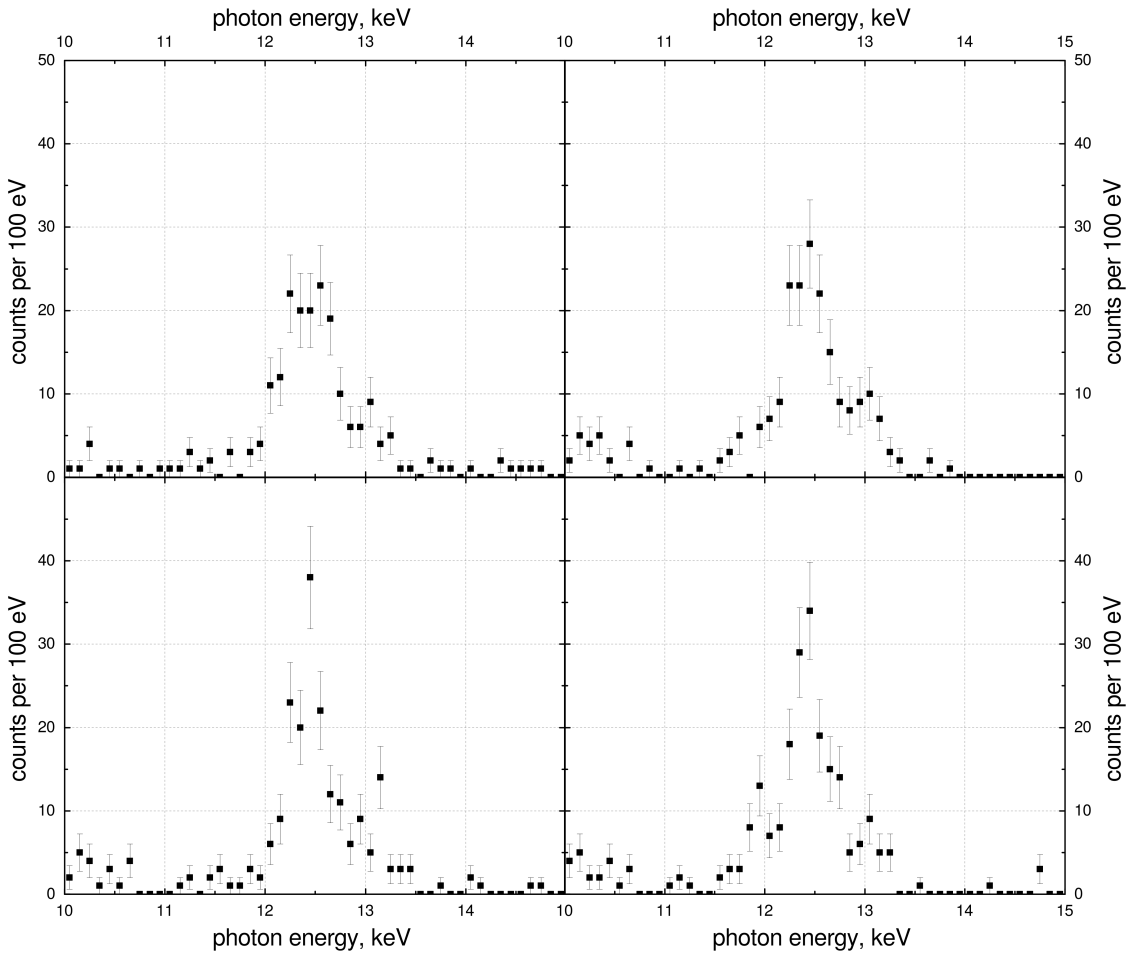


Figure 67: Same as figure 64, except with the final geometric alignment between collimator and SDD chips.

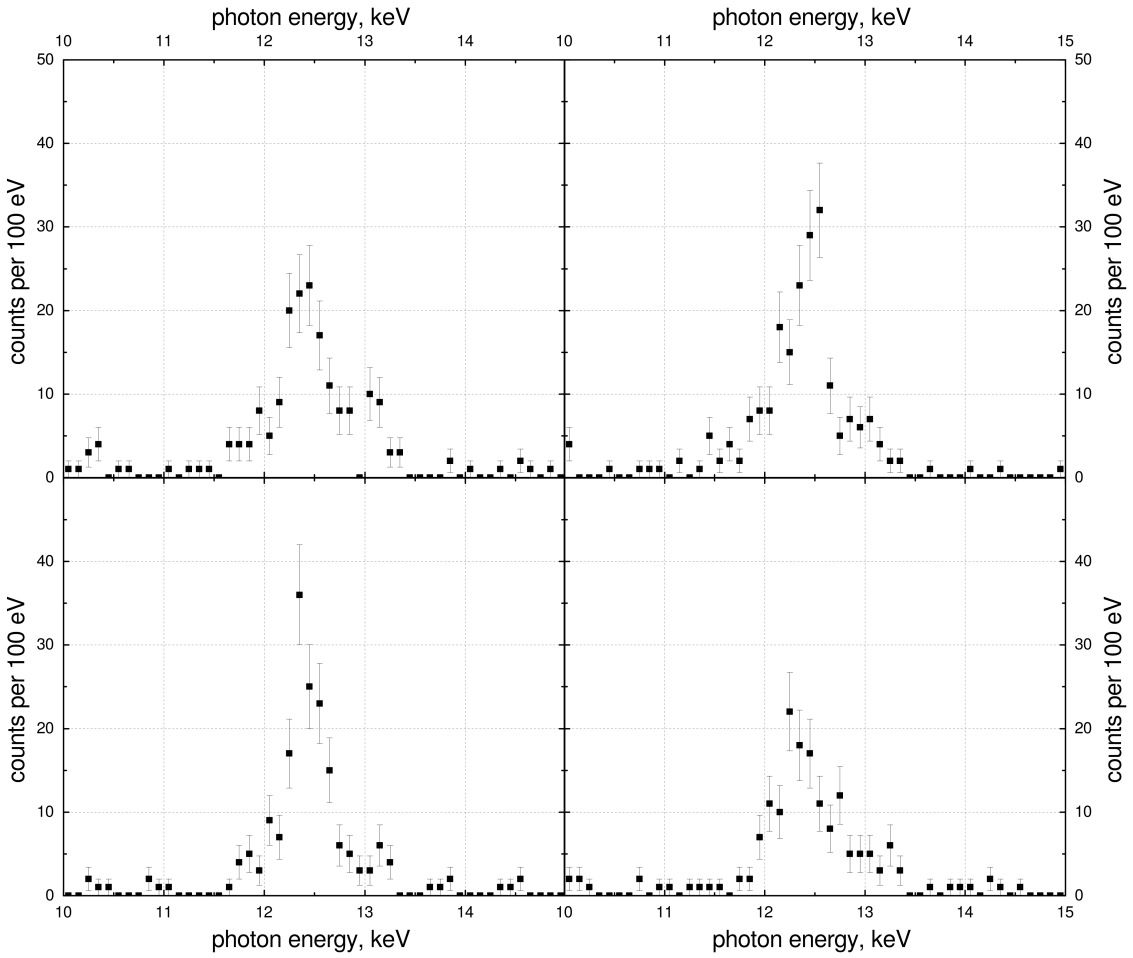


Figure 68: Same as figure 67, except with the second four polarimeter channels.

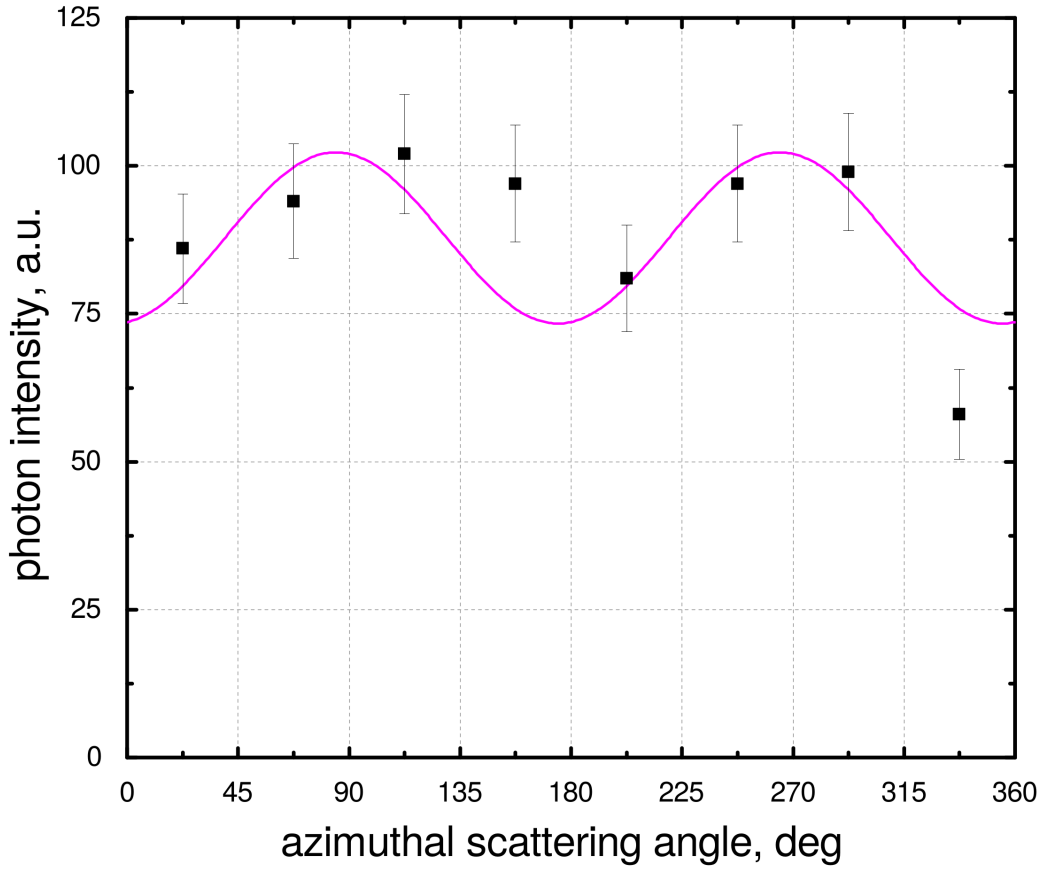


Figure 69: Measured azimuthal angular scattering distribution of X-rays due to the *KLL* DR $Be_1$ resonance in highly charged krypton ions. The magenta line represent the fit with the Klein-Nishina formula.

For the data analysis, the contribution of $L$ shell RR X-rays to the DR peak, which is at 9% has to be taken into account, see chapter 4.2 for the procedure. The polarisation of these RR X-rays is $P_{RR} = 0.59 \pm 0.15$. The error is due to an uncertainty about the charge state distribution in the trap. Fitting the measured azimuthal angular scattering distribution, yields a degree of linear polarisation of $P_{DR,\,exp} = 0.56 \pm 0.20$ for the $Be_1$ *KLL* DR resonance of highly charged krypton ions. The theoretical value is $P_{DR,\,theo} = 0.49$.

The first polarisation measurement with the new SDD based Compton polarimeter has been successfully performed. The measured degree of polarisation has a relative error of 37.5% with respect to the measured degree of polarisation. Longer measuring time and thus more statistics is needed for a more precise measurement. Furthermore, adjusting the geometrical alignment between incoming X-rays, collimator and SDD chips is more complicated in the back scattering geometry than for the SiPIN based Compton polarimeter.

## 6.3 Polarisation Measurement at Petra III

The SDD polarimeter was tested in the course of a polarisation measurement at the Petra III synchrotron radiation source at DESY, Hamburg, in June 2016. The measurements were performed at the beamline P01, where an undulator functions as a source for high brilliance, monochromatic X-ray beams in the energy range from 5 keV to 70 keV with a 100% degree of linear polarisation in the horizontal direction. Under these conditions, the polarimeter response to high-flux X-rays with a high degree of polarisation was tested.

### 6.3.1 Petra III Facility

Petra III is the most brilliant storage-ring-based X-ray radiation source in the world. The Petra accelerator, a 2.3 kilometre synchrotron, stores pulsed beams of electrons - or positrons - at energies of 6 GeV with a beam current of 100 mA. Synchrotron radiation is emitted when charged particles at ultra relativistic speeds are accelerated radially. In synchrotron radiation sources this is achieved by bending magnets, which keep the particles on their circular orbit, or by inserted periodic magnetic structures, undulators or wigglers, which force the particles on a sinusoidal path. All three methods lead to radiation directed tangentially outward in a narrow radiation cone [82]. Synchrotron radiation is characterised by a high brilliance, which is defined as the number of photons per second, per solid angle, per source size, and per bandwidth of 0.1% of the central frequency. Petra III achieves a brilliance exceeding $10^{21}$ ph/(s mm$^2$ mrad$^2$ 0.1%BW)[5]. In comparison to conventional synchrotrons which accelerate particles from low to high energies, synchrotron light sources are storage rings, in the sense that particles are stored at a constant energy and radio-frequency cavities are used to replenish energy losses due to synchrotron radiation.

Bending magnet radiation occurs when charged particles move through the field of a bending magnet with ultra-relativistic speeds and are thus accelerated towards the center of the storage ring, see figure 70. The charged particle emits radiation in a small cone with an emission angle $\theta$ depending on its Lorentz factor $\gamma$: $\theta = 1/\gamma$. For Petra III the emission angle is in the $10^{-2}$ mrad regime. Bending magnet radiation has a broad spectrum which ranges from microwaves into the X-ray regime. The critical energy $E_C$, with half the emitted photons having a larger and the other half a smaller energy than $E_C$, of this radiation provides a parameter for characterising bending magnet radiation [82]:

[5] http://photon-science.desy.de

$$E_C = \frac{3e\hbar B\gamma^2}{2m_e} \tag{59}$$

For Petra III, with bending magnet fields of 0.873 T, this yields $E_C$ =20.9 keV.

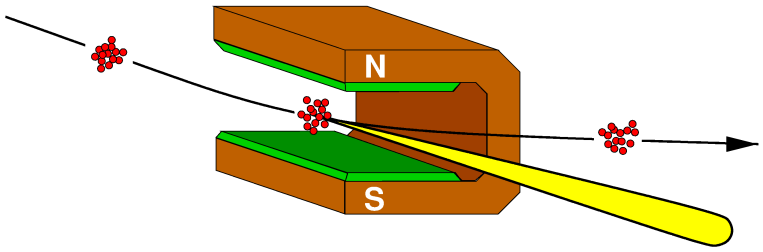


Figure 70: Production of bending magnet radiation in synchrotrons. Ultra-relativistic, charged particles move through a uniform magnetic field and are accelerated towards the center of the synchrotron. They emit radiation tangentially in a narrow cone. Taken from [83]

Undulators consist of a periodic structure of dipole magnets, see figure 71. When relativistic electrons or positrons traverse the periodic magnetic field $B(z) = B_0 cos(2\pi z/\lambda_u)$, with the peak magnetic field $B_0$ and the magnetic period $\lambda_u$, the produced radiation is very intense, collimated in the z-direction and has a very small energy range. Following [82], a derivation of the "undulator equation" is presented here, which yields the wavelength of photons emitted from an undulator as a function of the magnetic field geometry of the undulator, the Lorentz factor of the electrons/positrons passing through it and the observation angle with respect to the undulator axis. It also yields the wavelengths of the higher harmonics of the undulator radiation.

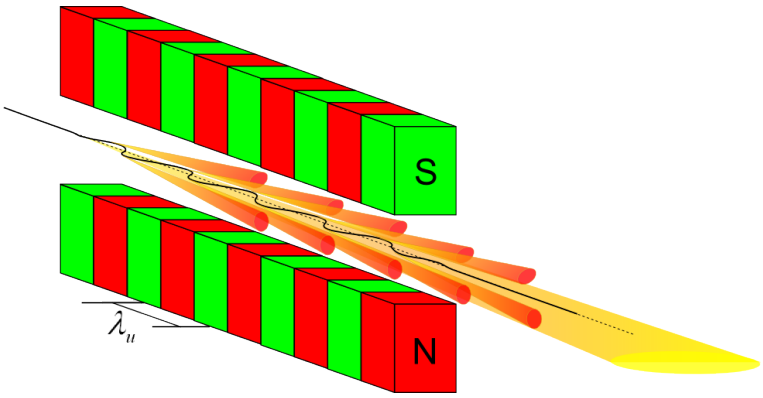


Figure 71: Production of undulator radiation in synchrotrons. Relativistic, charged particles move through a periodic structure of dipole magnets. Taken from [83]

In the electron rest frame, upon entering the undulator, the electron passes a Lorentz contracted periodic magnetic structure with the period $\lambda' = \lambda_u/\gamma$. The electron oscillates and radiates like a classical oscillating dipole with the frequency $\omega' = 2\pi c\gamma/\lambda_u$ with a small relative spectral width $\omega'/\Delta\omega' = N$, with the number of magnetic periods N, see figure 72.

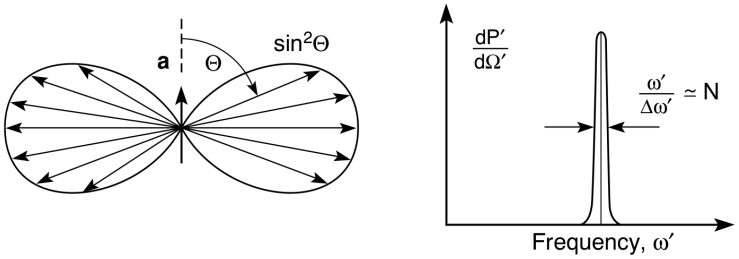


Figure 72: (left side) Dipole radiation pattern of undulator radiation in the rest frame of the electron. (right side) Radiation spectrum of undulator radiation in the rest frame of the electron. Adapted from [82]

In the laboratory frame the radiated wavelength is reduced by relativistic Doppler shifting. In a Taylor expansion around small angles around the electron beam direction $\theta = 0$, this yields the wavelength of emitted radiation in the laboratory frame:

$$\lambda = \lambda'\gamma(1 - cos(\theta)) = \frac{\lambda_u}{2\gamma^2}(1 + \gamma^2\theta^2) \tag{60}$$

The radiation pattern in the laboratory frame is a relativistically contracted dipole radiation pattern, which is often referred to as "searchlight" radiation. Radiation is emitted in a central cone with half an opening angle given by $\theta = 1/(2\gamma)$, see figure 73. Off-axis effects significantly widen the relative spectral width, which makes the use of monochromators to select a small spectral width necessary.

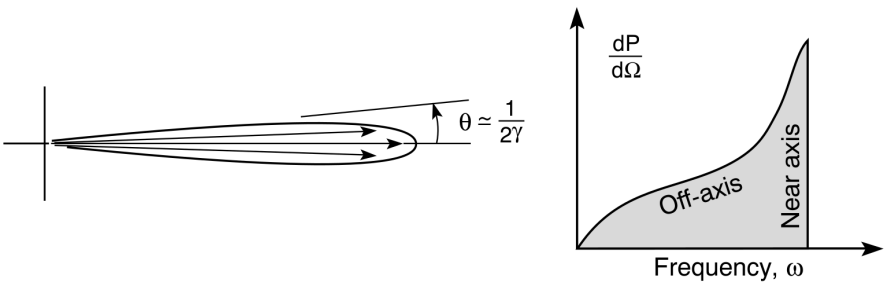


Figure 73: (left side) Dipole radiation pattern of undulator radiation in the laboratory frame. Radiation emission is relativistically contracted to the forward direction. (right side) Radiation spectrum of undulator radiation in the laboratory frame. Adapted from [82]

The actual undulator equation takes effects due to the transverse velocity of the electron $v_x$ into account, which not only yields a dependency on the magnetic field strength and geometry, but also the higher harmonics of the undulator radiation. Deriving this equation has to start with the force an electron experiences in the presence of an electromagnetic field: $d\vec{p}/dt = e(\vec{E} + \vec{v} \times \vec{B})$. In the absence of electric fields and for the periodic magnetic undulator field, this yields in the limit $\vec{v} \simeq \vec{v_z}$:

$$v_x = \frac{Kc}{\gamma} sin\left(\frac{2\pi z}{\lambda_u}\right) \; ; \quad \text{with } K \equiv \frac{eB_0\lambda_u}{2\pi mc} \tag{61}$$

with the non-dimensional parameter K, which defines the magnetic strength for the periodic magnetic structure. K is also called the deflection parameter. It determines the maximum deflection angle of the electron on its trajectory through the undulator, $\theta_{e,max} \simeq K/\gamma$. Undulator radiation is only produced for K<1. In this regime the maximum deflection angle of the electron is within the emitted radiation cone, which allows interference effects between the emitted radiation by the oscillating electrons and the motion of other electrons. This results in a narrow spectral bandwidth. In wigglers, periodic magnetic insertion devices with K>1, on the other hand, such interference effects are not present and they have a much broader spectral bandwidth.

The velocity of the electron in z-direction is not a linear function in time, but includes oscillations. Starting with the Lorentz factor, as a constant in magnetic fields, and inserting the transverse velocity of the electron $v_x$, yields these oscillations in $v_z$.

$$\frac{v_z}{c} = 1 - \frac{1 + K^2/2}{2\gamma^2} + \frac{K^2}{4\gamma^2} cos\left(n2\lambda_u z\right) \tag{62}$$

with the higher harmonics n of the electron oscillation in z-direction. This yields the undulator equation with the higher harmonics in n:

$$\lambda = n\frac{\lambda_u}{2\gamma^2}\left(1 + \frac{K^2}{2} + \gamma^2\theta^2\right) \tag{63}$$

The first term represents the generation of X-rays for the Lorentz contracted dipole radiation. The second term, representing the geometry and strength of the periodic magnetic structure, allows magnetic tuning of the emitted radiation. The third term accounts for off-axis variations of the emitted wavelength. The radiation pattern of the higher harmonics varies from the first harmonic. Odd harmonics have their emission maximum for $\theta = 0$, while even harmonics peak off axis.

At the P01-Beamline at Petra III, where the test measurement was conducted, 100% linearly polarised X-ray beams are produced in the energy range between 5 keV and 70 keV with an energy resolution of 1 meV at 14.4 keV. To achieve such a high energy resolution, the X-ray beam from the undulator passes a crystal monochromator assembly. Only a narrowly selected range of wavelengths, which is diffracted according to Bragg's law, passes a monochromator. Accordingly, for a given crystal spacing, e.g. 3.136 Å for the (111) planes in silicon, this energy range can be selected by setting the scattering angle. For 14 keV X-rays, Bragg scattered at the (111) planes in silicon, this angle is at 61.6°.

### 6.3.2 Experiment

The SDD polarimeter was positioned right in the X-ray beam from the undulator at the beamline P01. The third harmonic of the undulator was used to set the photon energy to 13 keV by the Si (111) double crystal monochromator. The monochromator was not detuned to suppress the higher harmonics generated at the undulator. In front of the collimator, a 1 cm thick aluminium plate was placed to attenuate the beam. Without the plate, the signal count rate in the detector would have exceeded the maximum possible value of 1 kHz, which can be handled by the data acquisition system. Mounting the plate in front of the collimator modifies the modulation factor of the polarimeter, see chapter 3.2.3. For the relevant X-ray energies here, i.e. 13 keV and 39 keV, the modulation factor is M = 0.23 and 0.25, respectively.

Energy spectra from the eight SDD channels were recorded, see figure 74 for the energy spectrum from channel 7. The energy resolution is 300 eV FWHM at 13 keV. The following lines in the spectrum can be clearly identified. At 6.4 keV, there is the iron $K\alpha$ line. The line at 13 keV is due to the first harmonic of the undulator. The line at 12.4 keV is due to Compton scattered X-rays of the first harmonic. The line at 39 keV is due to the ninth harmonic of the undulator beam, with Compton scatterings of these X-rays at approximately 33.5 keV. The line at 14.4 keV may be due to the Mößbauer effect in $^{57}$Fe, which is found in the beamline. There is a faint line at 13.7 keV which might be due to Compton scattered X-rays with 14.4 keV. The line at 25.2 keV may be due to $K\alpha$ X-rays of tin. The line at 26.4 keV may be due to $K\alpha$ X-rays of antimony. Both tin and antimony is used in solder, which is found in the polarimeter. X-rays due to the ninth harmonic may have ionised the tin and antimony used in the polarimeter. The line at 28 keV could not be identified.

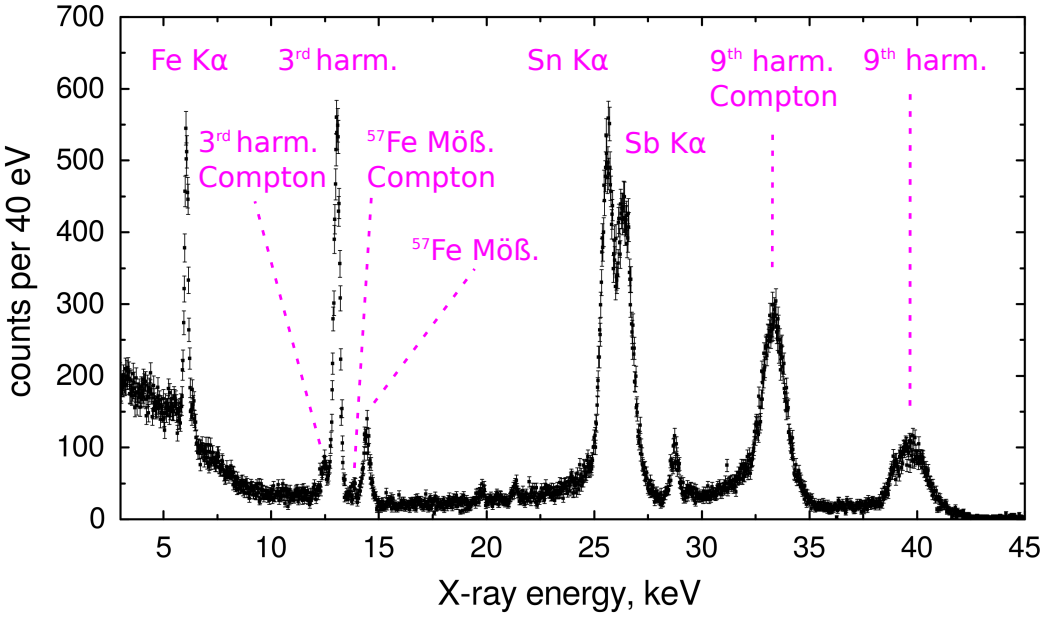


Figure 74: Energy spectrum of the undulator beam in channel 7 of the SDD polarimeter. $3^{rd}$ *harm.* refers to the third harmonic of the undulator, while $3^{rd}$ *harm. Compton* refers to the Compton scattered X-rays of the third harmonic.

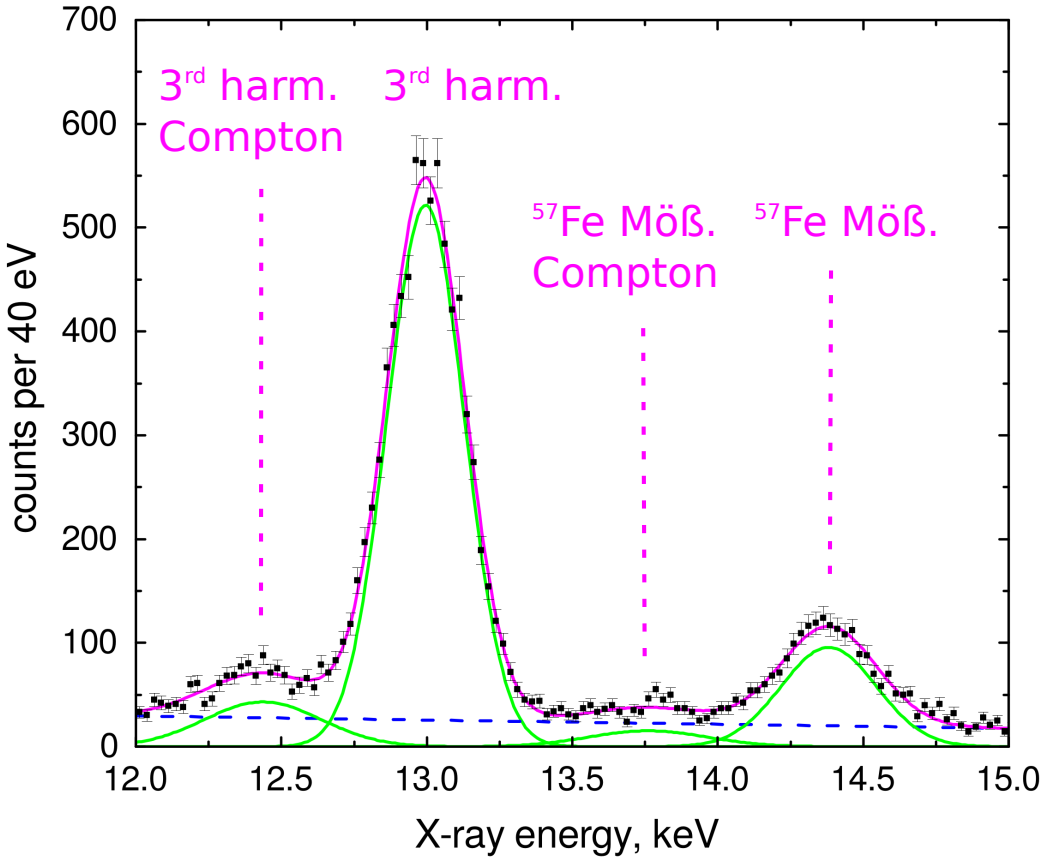


Figure 75: Energy spectrum of the undulator beam in channel 7 of the SDD polarimeter for the energy region of the third harmonic at 13 keV. The lines are fitted with Gaussian profiles. A first order polynominal is used to fit the background. The fit is shown in magenta. The peaks are shown in green and the background in blue.

The degree of linear polarisation of X-rays of the third and ninth harmonic is analysed here. For the third harmonic, the peak due to Compton scattering sits on top of a linear background which is also polarised. To deduce its contribution, the energy spectra in the energy range from 12 keV to 15 keV were fitted, see figure 75. The contribution of background X-rays at 12.4 keV is at 45%. Its polarisation was deduced by fitting the azimuthal angular scattering distribution of X-rays in the energy range from 10 keV to 12 keV with the Klein-Nishina formula. The background X-rays have a degree of linear polarisation of $P_L = 0.14$ in the vertical direction. The azimuthal angular scattering distribution of Compton scattered X-rays of the third harmonic, in the energy region from 12.3 keV to 12.5 keV, was also fitted with the Klein-Nishina formula, see figure 76. An explanation on how to account for background X-rays in the fit has been given in chapter 4.2. The fit yields a degree of linear polarisation of the third harmonic of $P_L$ = -0.95±0.09, i.e. it is fully polarised in the horizontal direction. The degree of linear polarisation of

the third harmonic at 13 keV has been measured before with a Bragg polarimeter. There the measured degree of linear polarisation was $P_L$ = -1.0000±$10^{-4}$ [84]. The measurements with the SDD Compton polarimeter and the Bragg polarimeter agree well.

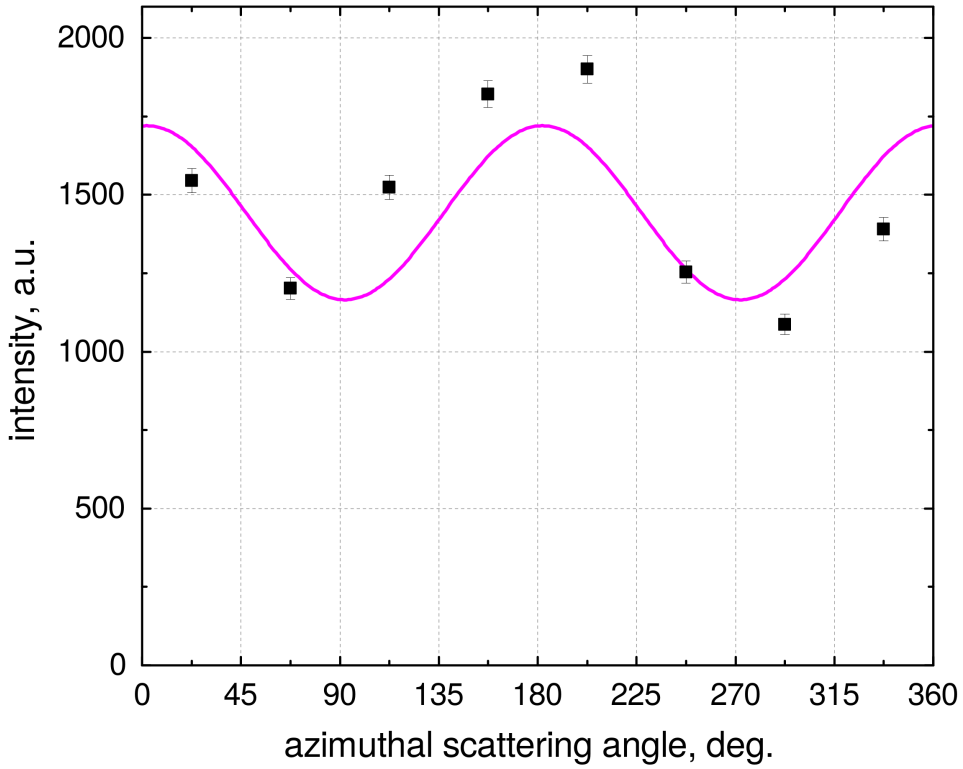


Figure 76: Measured azimuthal angular scattering distributions of X-rays of the third harmonic. The distribution is fitted with the Klein-Nishina formula, shown in magenta.

For the ninth harmonic, the azimuthal scattering distribution of Compton scattered X-rays within an energy interval from 33 keV to 34 keV is fitted to deduce their degree of linear polarisation, see figure 77. The background is in this energy range at a level of 4% and is therefore neglected in the analysis. The deduced degree of linear polarisation of the ninth harmonic is $P_L$ = -1.00±0.04, i.e. it is, like the third harmonic, fully polarised in the horizontal direction.

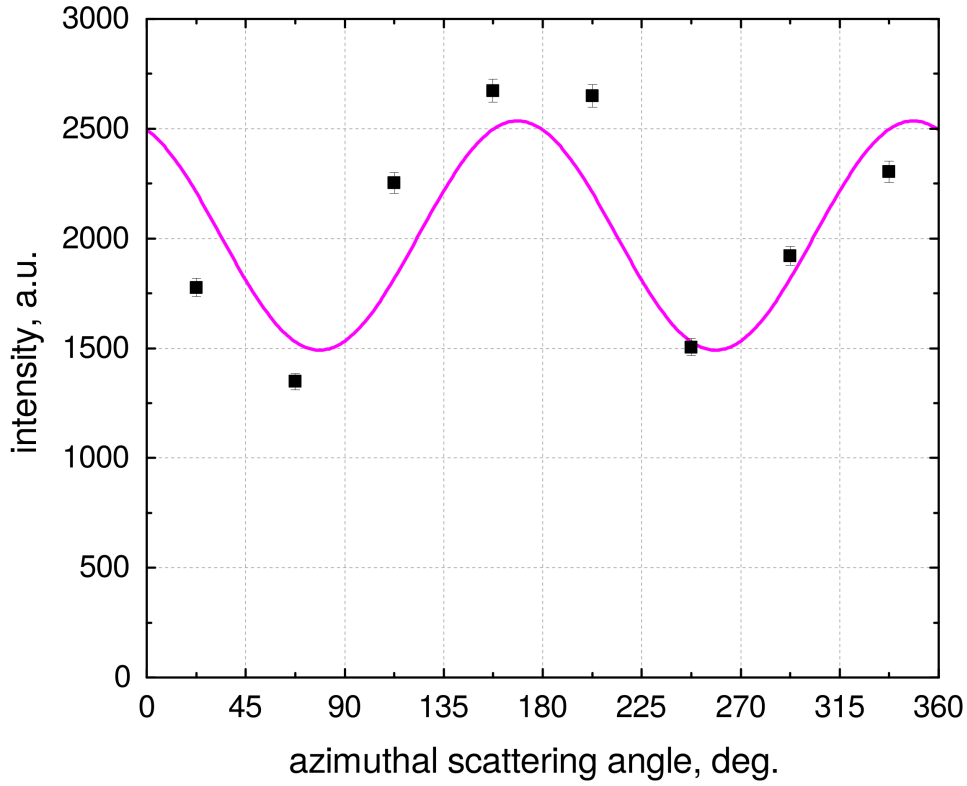


Figure 77: Same as figure 76 except for the nineth harmonic.

The discrepancy between the azimuthal scattering distributions of the third and ninth harmonic and their respective fits is due to a geometrical missalignment between the X-ray beam from the undulator and the SDD chips, which is similar to the geometrical missalignment between the collimator and the SDD chips in the experiment with krypton ions, see chapter 6.2. In both cases, the beam has to be perfectly aligned to the geometric center of the circularly arranged chips. Furthermore, the beam has to impinge perpendicularly on the surface of the scatterer. The width of the beam from the undulator, which is usually of the order of a few hundred µm, is many orders of magnitude smaller than the hole of the collimator. This makes beam collimation with the SDD polarimeter impossible. The recorded azimuthal scattering distributions indicate that, from the perspective of the beam, the beam was aligned off center to the left side.

The new polarimeter generation, the SDD based Compton polarimeter, has been designed for experiments at synchrotron radiation sources. A first, successful test of its performance in this environment has been presented here. Its high energy resolution has made resolving weak lines from background possible. Within the error bars the polarisation measurements agree with the expectations for synchrotron radiation in the energy range between 13 keV and 39 keV, for which the polarimeter

was designed. To conclude, the new polarimeter generation is ready to be used in experiments at synchrotron radiation sources, where it can be used to measure the polarisation of single transitions of HCIs.

# 7 Conclusion and Outlook

In this thesis work, X-ray polarisation measurements in collisional processes in laboratory plasmas of stored HCIs have been performed. The aim was to further our understanding of relativistic particle dynamics under the presence of strong nuclear electromagnetic fields. Therefore, the resonant electronic recombination process, *KLL* DR, into few electron krypton and xenon ions, has been studied. Analysing the degree of linear polarisation of such *KLL* DR lines yields the alignment of the doubly-excited intermediate state, i.e. the population mechanism of the magnetic sublevels of the intermediate state with electrons. Probing the alignment of the excited state via polarisation measurements allows a study of the influences of relativistic effects on the electron-electron interaction in collisional processes, which become pronounced in the presence of strong electromagnetic fields

A newly developed silicon PIN Compton polarimeter was used to perform these measurements. Thereby, the technique of performing polarisation measurements at EBITs in the energy range from 10 keV to 35 keV has been established. Such measurements had been performed before with Bragg crystal polarimeters [25] but only features indicating polarised radiation from an ion trap could be measured. The analysis of polarisation-dependent spectra from Bragg polarimeters suffers from a need to account for the crystal reflectivity and its polarisation sensitivity. These inherent difficulties make such polarisation measurements difficult to perform. The technique presented here allows deriving the degree and angle of linear polarisation with errors below 10%. Furthermore, in comparison to Bragg crystal polarimetry, this technique does not suffer from the narrow energy range set by Bragg's law and can be applied for a broad energy range without any adjustments.

In the first experiment at the FLASH-EBIT facility, the population mechanism of magnetic sublevels of the intermediate state formed in *KLL* DR into highly charged krypton ions has been studied. The density matrix formalism is used to derive the polarisation of DR lines in a stringent fully relativistic calculation. The population mechanism of magnetic sublevels has also been qualitatively illustrated by taking the angular momenta of the initial and intermediate states, as well as the angular momentum of the recombining electron, into account. Furthermore the influence relativistic effects in the electron-electron interaction have on the alignment of the specific intermediate state of the $Li_1$ DR resonance have been studied. Breit interaction was predicted to influence the polarisation of this specific resonance [6]. Due to a lack of the necessary statistics, we were not able to clearly resolve the influence Breit interaction has on the polarisation of this specific line.

A second polarimetry experiment at the HD-EBIT facility was conducted to clearly resolve the influence Breit interaction has on the polarisation of the $Li_1$ resonance. The influence was predicted to become more pronounced for heavier ions, and thus stronger electromagnetic fields. Therefore the measurements were performed with highly charged xenon ions. The effect Breit interaction has on the polarisation of the $Li_1$ resonance was measured in a $5\sigma$ confidence level, which clearly resolves its influence on the dynamics of the electron-electron interaction in strong fields. The presented experiments also benchmark relativistic distorted-wave calculations performed with the FAC and RATIP computer codes, with which they are in good agreement [24].

As already mentioned in the introduction to this thesis, an experiment measuring the influence Breit interaction has on the alignment of the intermediate state of the $Li_1$ resonance had been performed before by Z. Hu et al. [35] in 2014. There, the alignment had been measured indirectly by combining X-ray and DR resonance strength measurements. Such measurements result in large relative uncertainties. As a result, the measurements had been performed with high-Z elements. In comparison, the experiments presented here offer a direct measurement and, therefore, a clearer resolution of the influence of Breit interaction on the alignment of the intermediate state of the $Li_1$ resonance.

Further experiments are planned by our group to study the even finer details of the electron-electron interaction, e.g. QED effects on the alignment of the intermediate states in *KLL* DR. The linear polarisation of X-rays produced by the $Li_1$ resonance in *KLL* DR is not only influenced by the "classical" Breit interaction, but on a more precise level, by the generalised Breit interaction, which takes into account the frequency of the virtual photon exchanged by the interacting electrons in first order QED. Quantitative theoretical results of this effect have been published by Tong et al. in 2015 [7]. GBI effects become distinct at Li-like ions with high atomic number. For ions species with $Z \geq 80$ the effect GBI has on the polarisation of the $Li_1$ line exceeds 8% in comparison to the BI effect. At the HD-EBIT such heavy elements can be produced. Alternatively, measurements at experimental storage rings are an option. To perform such a polarisation measurement, our group is currently building a new Compton polarimeter based on annular segmented germanium with an energy resolution of 2 keV for X-ray energies from 30 keV - 2 MeV.

Polarimetry at the low energy region of hard X-rays has so far been limited by the low efficiency of Compton scattering in this region. In this thesis work, a new Compton polarimeter has been developed, built and tested at two X-ray

radiation facilities. It is based on SDD chips for the energy region of 6 keV to 35 keV and achieves an energy resolution of 600 eV for Compton scattered X-rays at an energy of 13 keV. For unscattered X-rays at 6 keV, the SDD chips provide an energy resolution of 180 eV. This new polarimeter has been tested at a polarisation measurement of *KLL* DR X-rays of highly charged krypton ions at the FLASH-EBIT facility, as well as at the Petra III synchrotron radiation source at DESY. Both Compton polarimeters presented here are simple yet powerful polarisation analysers for the hard X-ray energy range of below 35 keV. Their simple geometry enables them to be used at any radiation facility.

The Compton polarimeters developed in our group are ready to be applied to diagnostics of high temperature plasmas sources, as e.g. tokamaks [85] or laser-generated plasma sources [86]. In tokamaks with very high temperature plasmas in the range of 10 keV to 30 keV, the polarimeters developed here can perform measurements on highly charged krypton, which is used as a coolant gas, to derive information about the directionality of plasma electrons. The feasibility of this method has already been proven for helium-like and beryllium-like oxygen impurity lines at the WT-3 tokamak at the Kyoto University [87]. Here, a VUV spectrometer with a double refracting calcite plate has been used to measure polarisation properties of impurity emission lines in the 100 eV to 300 eV range. Traces of alignment of the ensemble of excited ions were found, which indicates a spatially anisotropic collisional excitation by electrons with an anisotropic velocity distribution. Similar alignment creation in hydrogen n=3 levels observed on Motional Stark Effect (MSE) spectra of the LHD plasma in Tokyo, Japan, has also been reported [88]. Here polarisation measurements of the Balmer-$\alpha$ line can be used to derive the magnetic field orientation in the plasma. Using the polarimeters presented here in this thesis to perform such polarisation measurements with highly charged krypton ions would enable measurements of the actual degree of linear polarisation of emission lines and would furthermore yield more detailed information about the electron velocity distribution in tokamak plasmas.

DR lines are also used for temperature diagnostics of hot plasmas [89] [90]. To be able to derive precise information about the plasma temperature, the polarisation of such lines has to be taken into account. In this thesis, a benchmark for theoretical models used to calculate polarisation of DR lines has been provided, as well as experimental techniques to directly perform such polarisation measurements.

To conclude, the polarimetry studies and the newly developed Compton polarimeters presented here open numerous possibilities for experimental studies with highly charged ions and for diagnostics of anisotropies of hot laboratory and astrophysical plasmas.

# References


[1] Th. Stöhlker et al. “Polarisation and Angular Correlation Studies of X Rays Emitted in Relativistic Ion-Atom Collisions”. In: *Eur. Phys. J. Special Topics* 169 (2009).

[2] Z. Chen et al. “Influence of Quantum Interference on the Polarization and Angular Distribution of X-ray Radiation Following Electron-Impact Excitation of Highly Charged H-like and He-like Ions”. In: *Phys. Rev. A* 90 (2014).

[3] S. Fritzsche et al. “X-ray Emission from Highly Charged Ions Following Dielectronic Recombination: Relativistic Effects Upon Angular Distributions and Polarization”. In: *Physica Scripta* 2011 (2011).

[4] K. Reed and M. Chen. “Relativistic Effects on the Polarization of Line Radiation Emitted From He-like and H-like Ions Following Electron-Impact Excitation”. In: *Phys. Rev. A* 48 (1993).

[5] S. Tashenov et al. “First Measurement of the Linear Polarization of Radiative Electron Capture Transitions”. In: *Phys. Rev. Lett.* 97 (2006).

[6] Stephan Fritzsche, Andrey Surzhykov, and Thomas Stöhlker. “Dominance of the Breit Interaction in the X-Ray Emission of Highly Charged Ions Following Dielectronic Recombination”. In: *Phys. Rev. Lett.* 103 (2009).

[7] X. Tong et al. “Mechanism of Dominance of the Breit Interaction in Dielectronic Recombination”. In: *Journal of Physics B* 48.14 (2015).

[8] J. R. Oppenheimer. “On the Quantum Theory of the Polarization of Impact Radiation”. In: *Proc. N. A. S.* 13 (1926).

[9] W. G. Penney. “Effect of Nuclear Spin on the Radiation Excited by Electron Impact”. In: *Proc. N. A. S.* 18 (1932).

[10] A. Ellett et al. “Polarization of Radiation Excited by Electron Impact”. In: *Phys. Rev.* 27 (1926).

[11] H. Heideman et al. “The Polarization of the 492.2 nm Line of Helium (Excited by Electrons) at Energies Near 60 eV”. In: *Physica* 63 (1973).

[12] J. Hrdý et al. “Polarization of the $L\alpha_1$ X Rays of Mercury”. In: *Phys. Rev. A* 2 (1970).

[13] S. McFarlane. “The polarization of characteristic X radiation excited by electron impact”. In: *J. Phys. B* 5 (1972).

[14] J. Scofield. “Angular and Polarization Correlations in Photoionization and Radiative Recombination”. In: *Phys. Rev. A* 40 (1989).

[15] A. Surzhykov et al. “Polarization Studies on the Radiative Recombination of Highly Charged Bare Ions”. In: *Phys. Rev. A* 68 (2003).

[16] A. Surzhykov et al. “Interelectronic Interaction Effects on the Polarization of Recombination Photons”. In: *Phys. Rev. A* 83 (2011).

[17] G Weber et al. “Direct Determination of the Magnetic Quadrupole Contribution to the Lyman-$\alpha_1$ Transition in a Hydrogenlike Ion”. In: *Phys. Rev. Lett.* 105 (2010).

[18] A. Surzhykov et al. “Radiative Electron Capture into High-$Z$ Few-Electron Ions: Alignment of the Excited Ionic States”. In: *Phys. Rev. A* 73 (2006).

[19] S. Fritzsche, M. Kabachnik, and A. Surzhykov. “Angular Distribution of the Dielectronic Satellite Lines from Relativistic High-$Z$ Ions: Multipole-Mixing Effects”. In: *Phys. Rev. A* 78 (2008).

[20] S. Zakowicz et al. “Angular Distribution of Hypersatellite and Satellite Radiation Emitted after Resonant Transfer and Excitation into $U^{91+}$ ions”. In: *Phys. Rev. A* 68 (2003).

[21] X. Ma et al. “Electron-Electron Interaction Studied in Strong Central Fields by Resonant Transfer and Excitation with H-like U Ions”. In: *Phys. Rev. A* 68 (2003).

[22] M. Gail, N. Grün, and W. Scheid. “Angular distribution of radiation emitted after resonant transfer and excitation”. In: *Journal of Physics B: Atomic, Molecular and Optical Physics* 31 (1998).

[23] H. S. W. Massey and D. R. Bates. “The properties of neutral and ionized atomic oxygen and their influence on the upper atmosphere”. In: *Reports on Progress in Physics* 9 (62 1942).

[24] H. Jörg et al. “Linear Polarization of X-Ray Transitions due to Dielectronic Recombination in Highly Charged Ions”. In: *Phys. Rev. A* 91 (2015).

[25] A. S. Shlyaptseva et al. “Polarization-Dependent Spectra of X Ray Dielectronic Satellite Lines of Be-like Fe”. In: *Phys. Rev. A* 57 (1998).

[26] M. Inal and J. Dubau. “Polarisation of Dielectronic Recombination Satellite Lines”. In: 22 (1989).

[27] M. Chen and J. Scofield. “Relativistic Effects on Angular Distribution and Polarization of Dielectronic Satellite Lines of Hydrogenlike Ions”. In: *Phys. Rev. A* 52 (1995).

[28] A. S. Shlyaptseva et al. "Polarization Properties of Dielectronic Satellite Lines in the K-shell X-Ray Spectra of B-like Fe XXII". In: *Journal of Physics B: Atomic, Molecular and Optical Physics* 32 (1999).

[29] M. Inal and J. Dubau. "Theory of Excitation of He-like and Li-like Atomic Sublevels by Directive Electrons: Application to X Ray Line Polarisation". In: *Journal of Physics B: Atomic and Molecular Physics* 20 (1987).

[30] S. Fritzsche et al. "X Ray Emission from Highly Charged Ions Following Dielectronic Recombination: Relativistic Effects upon Angular Distributions and Polarization". In: *Physica Scripta* 2011 (2011).

[31] S. Nahar, J. Oelgoetz, and A. Pradhan. "Recombination rate coefficients for KLL dielectronic satellite lines of Fe XXV and Ni XXVII". In: *Physica Scripta* 79 (2009).

[32] N. Nakamura et al. "Evidence for Strong Breit Interaction in Dielectronic Recombination of Highly Charged Heavy Ions". In: *Phys. Rev. Lett.* 100 (2008).

[33] J. Fontes et al. "Fully Relativistic Calculations of and Fits to $1s$ Ionization Cross Cections". In: *Phys. Rev. A* 59 (1999).

[34] D. Bernhardt et al. "Breit Interaction in Dielectronic Recombination of Hydrogenlike Uranium". In: *Phys. Rev. A* 83 (2011). URL: `http://link.aps.org/doi/10.1103/PhysRevA.83.020701`.

[35] Z. Hu et al. "Atomic-Number Dependence of the Magnetic-Sublevel Population in the Autoionization State Formed in Dielectronic Recombination". In: *Phys. Rev. A* 90 (2014).

[36] M. F. Gu. "Radiative recombination rate coefficients for bare through F-like isosequences of Mg, Si, S, Ar, Ca, Fe, and Ni". In: *The Astrophysical Journal* 589 (2003).

[37] S. Fritzsche. "The RATIP Program for Relativistic Calculations of Atomic Transition, Ionisation and Recombination Properties". In: *Comp. Phys. Comm.* 183 (2012).

[38] S. Tashenov et al. "Measurement of the Correlation between Electron Spin and Photon Linear Polarization in Atomic-Field Bremsstrahlung". In: *Phys. Rev. Lett.* 107 (2011).

[39] O. Kovtun et al. "Spin-Orbit Interaction in Bremsstrahlung and its Effect on the Electron Motion in a Strong Coulomb Field". In: *Phys. Rev. A* 92 (2015).

[40] A. Dean et al. “Polarized Gamma-Ray Emission from the Crab”. In: *Science* 321 (2008).

[41] P. Laurent et al. “Polarized Gamma-Ray Emission from the Galactic Black Hole Cygnus X-1”. In: 332 (2011).

[42] M. Weisskopf et al. “A precision measurement of the X-ray polarization of the Crab Nebula without pulsar contamination”. In: *ApJ* 220 (1978).

[43] P. Soffitta et al. “XIPE: the X-ray Imaging Polarimetry Explorer”. In: *Experimental Astronomy* 36 (2013).

[44] T. Chattopadhyay et al. “Prospects of Hard X-ray Polarimetry with Astrosat-CZTI”. In: *Experimental Astronomy* 37 (2014).

[45] W. Nolting. *Grundkurs Theoretische Physik 5/1*. Heidelberg: Springer, 2009.

[46] W. Demtröder. *Experimentalphysik 3: Atome, Moleküle und Festkörper*. Heidelberg: Springer, 2010.

[47] H. Friedrich. *Theoretische Atomphysik*. Heidelberg: Springer, 1994.

[48] F. Schwabl. *Quantenmechanik für Fortgeschrittene (QM2)*. Heidelberg: Springer, 2008.

[49] G. Breit. “The Effect of Retardation on the Interaction of Two Electrons”. In: *Phys. Rev.* 34 (4 1929).

[50] G. Breit. “The Fine Structure of He as a Test of the Spin Interactions of Two Electrons”. In: *Phys. Rev.* 36 (3 1930).

[51] G. Breit. “Dirac’s Equation and the Spin-Spin Interactions of Two Electrons”. In: *Phys. Rev.* 39 (4 1932).

[52] C. Fontes, D. Sampson, and H. Zhang. “Inclusion of the generalized Breit interaction in excitation of highly charged ions by electron impact”. In: *Phys. Rev. A* 47 (2 1993).

[53] H. Bethe and E. Salpeter. *Quantum mechanics of one and two electron atoms*. Heidelberg: Springer, 1957.

[54] Joseph B. Mann and Walter R. Johnson. “Breit Interaction in Multielectron Atoms”. In: *Phys. Rev. A* 4 (1 1971).

[55] *XCOM: Photon Cross Section Database*. `https://www.nist.gov/pml/xcom-photon-cross-sections-database`. Accessed: 2015-09-09.

[56] G. Nelson et al. “Gamma-Ray Interactions with Matter”. In: *Passive Nondestructive Analysis of Nuclear Materials* (1991).

[57] J. Jackson. *Classical Electrodynamics*. Hoboken: John Wiley, 1999.

[58] J. Hubbell et al. "Atomic Form Factors, Incoherent Scattering Functions, and Photon Scattering Cross Sections". In: *J. Phys. Chem. Ref. Data* 4 (1975).

[59] S. Tashenov et al. "Bremsstrahlung polarization correlations and their application for polarimetry of electron beams". In: *Phys. Rev. A* 87 (2013).

[60] D. Banas et al. "Differential L-shell radiative recombination rate coefficients for bare uranium ions interacting with low-energy electrons". In: *Eur. Phys. J. Special Topics* 2002 (2013).

[61] K. Yao et al. "KLL dielectronic recombination resonant strengths of He-like up to O-like xenon ions". In: *Phys. Rev. A* 81 (2 2010).

[62] J. von Neumann. "Wahrscheinlichkeitstheoretischer Aufbau der Quantenmechanik". In: *Göttinger Nachrichten* 1 (1927), pp. 245–272.

[63] V. Balashov, A Grum-Grzhimailo, and N. Kabachnik. *Polarisation and correlation phenomena in atomic collisions*. New York: Kluwer Academics / Plenum Publishers, 2000.

[64] S. Fritzsche, A. Surzhykov, and T. Stöhlker. "Radiative recombination into high-Z few-electron ions: cross sections and angular distributions". In: *Phys. Rev. A* 72 (2005).

[65] N. Andersen and K. Bartschat. *Polarisation, alignement, and orientation in atomic collisions*. New York: Springer-Verlag, 2001.

[66] F. Schwabl. *Quantenmechanik 1 (QM1)*. Heidelberg: Springer, 2007.

[67] *Oscillating Magnetic Dipols*. `http://laserstars.org/glossary/spontaneous.html`. Accessed: 2016-10-04.

[68] E. Donets, V. Ilushchenko, and V. Alpert. "Proc. of the 1st ICIS - Saclay". In: 635 (1969).

[69] M. Levine et al. "The electron beam ion trap: a new instrument for atomic physics measurements". In: *Physica Scripta* 1988 (1988).

[70] R. Marrs et al. "The super electron beam ion trap". In: *Physica Scripta* 1995 (1995).

[71] S. W. Epp et al. "X-ray laser spectroscopy of highly charged ions at FLASH". In: *Journal of Physics B* 43 (2010).

[72] J. Pierce. "Rectilinea Electron Flow in Beams". In: *J. Appl. Phys.* 11 (1940).

[73] S. Dobrodey. “Untersuchung von K-LL-Resonanzen dielektronischer Rekombination und simultaner Innerschalen-Vakuum-Ultraviolett bergnge in hochgeladenem Eisen mit einer Elektronenstrahl- Ionenfalle”. In: Master thesis (2015).

[74] G. Herrmann. “Optical theory od thermal velocity effects in cylindrical electron beams”. In: *J. Appl. Phys.* 29 (1958).

[75] S. Bernitt. “Resonante Anregung astrophysikalischer Rntgen-bergnge in hochgeladenen Eisenionen mit dem Freie-Elektronen-Laser LCLS”. In: Doctoral thesis (2013).

[76] S. Epp. “Rntgen-Laserspektroskopie hochgeladener Ionen in einer EBIT am Freie-Elektronen-Laser FLASH ”. In: Doctoral thesis (2007).

[77] S. Weber. “Compton polarimeter for 10-30keV x rays”. In: *Rev. Sci. Instrum.* 86 (2015).

[78] L. Strüder and H. Soltau. “High Resolution Silicon Detectors for Photons and Particles”. In: *Radiation Protection Dosimetry* 61 (1995).

[79] C. Shah et al. “Polarization Measurement of Dielectronic Recombination Transitions in Highly Charged Krypton Ions”. In: *Phys. Rev. A* 92 (2015).

[80] E. Gatti and P. Rehak. “Semiconductor drift chamber - an application of a novle charge transport scheme”. In: *Nuclear Instruments and Methods in Physics Research* 225 (1984).

[81] *Silicon Drift Detector Chip*. `http://www.azom.com/`. Accessed: 2016-09-23.

[82] D. Attwood. *Soft X-Rays and Extreme Ultraviolet Radiation: Principles and Applications*. Cambridge: Cambridge Universtity Press, 2000.

[83] *Bending Magnet Radiation*. `http://photon-science.desy.de/research/studentsteaching/primers/synchrotron_radiation/index_eng.html`. Accessed: 2016-09-09.

[84] H. C. Wille, Priv. Comm. (2016).

[85] K. Widmann et al. “Studies of He-like Krypton for Use in Determining Electron and Ion Temperatures in Very-High-Temperature Plasmas”. In: *Rev. Sci. Instrum.* 66 (1995).

[86] C. Hahn et al. “CdTe Timepix Detectors for Single-Photon Spectroscopy and Linear Polarimetry of High-Flux Hard X-Ray Radiation”. In: *Rev. Sci. Instrum.* 87 (2016).

[87] T. Fujimoto et al. “Polarization of Impurity Lines from a Tokamak Plasma”. In: *Phys. Rev. E* 54 (1996).

[88] A. Iwamae et al. “Alignment Creation and Deviation from Statistical Population Distribution in Hydrogen n=3 Levels Observed on MSE Spectra of LHD Plasma”. In: *Plasma Physics and Controlled Fusion* 51 (2009).

[89] T. Kato, T. Fujiwara, and Y. Hanaoka. “X-Ray Spectral Analysis of Yohkoh Bragg Crystal Spectrometer Data on a 1992 September 6 Flare: The Blueshift Component and Ion Abundances”. In: *The Astrophysical Journal* 492 (1998).

[90] P. Beiersdorfer et al. “Measurement of Level-Specific Dielectronic-Recombination Cross Sections of Heliumlike Fe XXV”. In: *Phys. Rev. A* 46 (1992).

# Acknowledgements

At the end of my Ph.D., I would like to acknowledge the people who contributed to my work, as well as helped and supported me throughout.

I would like to thank my supervisors, Dr. Stanislav Tashenov and Dr. José Ramón Crespo López-Urrutia. They have both been tremendously helpful during my work, supporting and guiding me from day one. I would like to thank them both for always taking their time to answer my questions and supporting me during the experiments.

I am thankful to Dr. José Crespo and Prof. Selim Jochim for agreeing to referee my thesis and additionally to Dr. Zoltán Harman and Prof. Werner Aeschbach-Hertig for agreeing to be in my examination committee. I would like to thank José, Chintan Shah, Sven Bernitt, Hendrik Bekker, Stepan Dobrodey and Michael Blessenohl for correcting parts of my thesis. I am also grateful to the graduate school, HGSFP, for funding my studied.

I would like to thank my colleagues at the Physics Institut and the MPIK: Chintan Shah, Oleksiy Kovtun, Zhimin Hu, Vanessa Simon, Armen Hyrapteyan, Sebastian Weber, Allison Pinto, Hendrik Bekker, Stepan Dobrodey, Michael Blessenohl, Sven Bernitt.

I would like to thank Prof. Stephan Fritzsche and Prof. Andrey Surzhykov for the theoretical calculations supporting my work.

I am grateful to my former supervisor, Dr. Kai Schweda, for introducing me to experimental physics.

I would also like to thank my parents, my brother and my grandmother.